**CENTRO DE INVESTIGACIÓN Y DE ESTUDIOS AVANZADOS
DEL INSTITUTO POLITÉCNICO NACIONAL**

UNIDAD ZACATENCO
DEPARTAMENTO DE FÍSICA

"Espectroscopía de Hadrones en el Experimento CMS"

Tesis que presenta

César Atzín Mondragón Herrera

para obtener el Grado de

Doctor en Ciencias

en la Especialidad de

Física

Director de tesis: Dr. Alberto Sánchez Hernández

Ciudad de México   Octubre, 2021

CENTER FOR RESEARCH AND ADVANCED STUDIES OF THE NATIONAL
POLYTECHNIC INSTITUTE

PHYSICS DEPARTMENT

"Hadron Spectroscopy in the CMS Experiment"

by

César Atzín Mondragón Herrera

In order to obtain the

Doctor of Science

degree, speciality in

Physics

Advisor: Ph. D. Alberto Sánchez Hernández

Mexico City   October, 2021

Abstract

Hadron Spectroscopy in the CMS Experiment

The present work consists of two independent analysis performed with data from the CMS experiment. The initial analysis describes the first observation of signals consistent with the $B_c(2S)^+$ and $B_c(2S)^{*+}$ states in proton-proton collisions at $\sqrt{s} = 13$ TeV, in an event sample corresponding to an integrated luminosity of $140\,\text{fb}^{-1}$, collected by the CMS experiment during the 2016–2018 LHC running periods. The states were observed studying the decay of B_c meson to $B_c\pi\pi$. We measure the mass of $B_c(2^1S_0)^+$, while for $B_c(2^3S_1)^+$ which is reconstructed shifted to the left of $B_c(2^1S_0)^+$ mass in consistency with the lost of the soft photon in the $B_c^* \to B_c\gamma$ decay. The mass shift is also measured.

The second analysis describes a search for a bottomonium resonance-like structure in the $\chi_b(1P)\pi^+\pi^-$ and $\Upsilon(1S)\pi^+\pi^-$ invariant mass spectrum, this is performed using an integrated luminosity of $\sim 139\,\text{fb}^{-1}$ of proton-proton collisions collected by CMS at $\sqrt{s} = 13$ TeV. The analysis is focused on the decay channel, $X_b \to \chi_{b1}\pi^+\pi^-$, following with the $\chi_{b1}(1P) \to \Upsilon(1S)\gamma$ and $\Upsilon(1S) \to \mu^+\mu^-$ decays . Upper limits on the relative production are estimated.

Resumen

Espectroscopía de Hadrones en el Experimento CMS

El presente trabajo consiste en dos análisis independientes, los cuales fueron realizados utilizando datos del experimento CMS. El análisis inicial describe la primera observación de señales consistentes con los estados $B_c(2S)^+$ y $B_c(2S)^{*+}$ en colisiones proton-proton a una energía de centro de masa $\sqrt{s} = 13\,\text{TeV}$ con una muestra de datos cuya luminosidad integrada es de $140\,\text{fb}^{-1}$, recolectada por el experimento CMS durante el periodo de toma de datos 2016-2018 del LHC. Los estados fueron observados estudiando el decaimiento de mesones B_c en el canal $B_c\pi\pi$. La masa de $B_c(2^1S_0)^+$ fue medida, mientras que $B_c(2^3S_1)^+$ es reconstruido con un desplazamiento hacia la izquierda de $B_c(2^1S_0)^+$, esto es consistente con la perdida de un fotón de baja energía en el decaimiento $B_c^* \to B_c\gamma$. La energía del corrimiento antes descrito también fue medida. El segundo análisis describe la búsqueda de una resonancia tipo botomonio en el espectro de masa de los estados finales $\chi_b(1P)\pi^+\pi^-$ y $\Upsilon(1S)\pi^+\pi^-$, con una muestra de datos cuya luminosidad integrada es de $\sim$139 fb^{-1}, el análisis se realizó usando datos de colisiones proton-proton recolectadas por el experimento CMS a $\sqrt{s} = 13\,\text{TeV}$. El estudio se enfoca en el canal de decaimiento $X_b \to \chi_{b1}\pi^+\pi^-$, seguido por los decaimientos $\chi_{b1}(1P) \to \Upsilon(1S)\gamma$ and $\Upsilon(1S) \to \mu^+\mu^-$. Al no encontrar indicios de resonancias en el espectro de masa se procede a estimar límites superiores de producción.

Acknowledgements

Thank you to my advisor, Alberto Sánchez Hernández, for providing guidance and feedback throughout this project. With great patience he provided a constructive environment for discussions that helped me to improve my knowledge of the particle physics world.

I express my gratitude to the institutions which made this thesis possible: CINVESTAV, CMS, CERN and especially to the Consejo Nacional de Ciencia y Tecnología (CONACyT), for the scholarship and the financial support provided during the period of my PhD.

My warm thanks go out to all the members of my loving family especially my wife Denisse and my little son Diego, whom always were there, giving me their unconditional support to continue.

I would like to thank to the B-Physics group at CMS, specially Alexis Pompili and Samet Lezki collegues from Bari University, they were fully involved in the work done during my PhD and provided additional funding to accomplish this thesis.

To my colleagues Jhovanny, Gabriel and Daniel, who helped me through discussions to deepen my understanding of several subjects.

During the seminar and the writing of this thesis professors: Iván Heredia, Pablo Roig, Jaime Santoyo, Alexis Pompili made unvaluable comments and corrections, for which I thank them. Any remaining errors are mine.

Contents

List of Figures

List of Tables

Chapter 1

Introduction

1.1 Quantum Chromodynamics

Quantum Chromodynamics (QCD) is the elementary theory that describes strong interactions between quarks and gluons in the Standard Model. A consequence of this theory is the prediction that quarks and antiquarks bind to form mesons, while three-quark combinations form baryons. In recent years, experiments have discovered several exotic manifestations of QCD, such as weakly-bound meson molecules, quark-gluon hybrids, tetraquarks and pentaquarks, in [1] a review of heavy exotic states is presented. The experimental study of hadronic spectroscopy is important to uncover the nature of these newly discovered states of matter, and for furthering our fundamental understanding of the strong force. With the increased center-of-mass energy and luminosity at the LHC, the CMS experiment presents opportunities for experimental exotic hadron spectroscopy, as well as the study of the doubly heavy-flavored B_c^+ meson.

1.2 Quarkonium

A special family of mesons includes the quarkonium states which are bosons consisting - in the most general way - of a bound $q\bar{q}$ pair which may have different flavours. Quarkonium can be the bound state of any of the quarks with their corresponding antiquark. However, it is not possible for the top and anti-top quarks to form a quarkonium state because the very heavy top mass gives it a large decay width, with a correspondingly short lifetime, so it decays weakly before quarkonium can form. The quarkonium states can be further categorised: the large masses of the c and b quarks forming the heavy quarkonium allow significantly different properties than quarkonium made from lighter quarks. Heavy quarkonium is named charmonium when formed by a $c\bar{c}$ pair and bottomonium when formed by a $b\bar{b}$ pair.

The observation of quarkonium states has been interpreted as the discovery of their constituent quarks. In 1974 the first charmonium state was observed independently at

SLAC and at Brookhaven (BNL) [2, 3]. The observation was immediately acknowledged as evidence of the existence of a fourth quark, the charm quark, previously predicted by Glashow, Iliopoulos and Maiani [4]. In 1977, Υ, the first bottomonium state was observed at Fermilab [5], and interpreted as evidence of the existence of the bottom quark.

$^{2S+1}L_J$	n_r	$c\bar{c}$ state	$b\bar{b}$ state
$^1S_0$	1	η_c	η_b
$^3S_1$	1	J/ψ	$\Upsilon(1S)$
$^3P_0$	1	χ_{c0}	χ_{b0}
$^3P_1$	1	χ_{c1}	χ_{b1}
$^3P_2$	1	χ_{c2}	χ_{b2}
$^3S_1$	2	$\psi(2S)$	$\Upsilon(2S)$
$^3S_1$	2	$\psi(3770)$	$\Upsilon(3S)$
$^3S_1$	4	$\psi(4040)$	$\Upsilon(4S)$

FIGURE 1.1: Table shows some predicted and observed $c\bar{c}$ and $b\bar{b}$ states, classified according the radial excitation quantum number n_r, and the momentum quantum numbers (S for the spin, L for the orbital momentum, and J for the total angular momentum).

1.2.1   Heavy quarkonia spectroscopy

With reference to the charmonium and bottomonium spectra, the J/ψ and Υ resonances, that are both vector mesons with spin 1, are the most produced states. The quantum numbers typically assigned to quarkonium are: $J = L + S$, where S is the total spin of the $q\bar{q}$ system, L is the orbital angular momentum and J is the total angular momentum. The spectroscopic notation $(n)^{2S+1}L_J$ is usually used to describe the quarkonium states. In literature also the J^{PC} convention is commonly used, being the P-parity quantum number of the $q\bar{q}$ system defined as $P = (-1)^{L+1}$, and the charge conjugation (C-parity) quantum number defined as $C = (-1)^{L+S}$.

Figures 1.2 and 1.3 show a subset of the charmonium and bottomonium spectra, namely the CP-even states (J^{++} and J^{--}) below the open-charm and open-beauty thresholds respectively. From the experimental point of view the most important decay modes for CMS are: 1) the dimuon decays of the S-wave states, $\psi(nS) \rightarrow \mu\mu$ and $\Upsilon(nS) \rightarrow \mu\mu$, 2) the radiative decays of the P-wave states, $\chi_c \rightarrow J/\psi\,\gamma$ and $\chi_{bJ}(nP) \rightarrow \Upsilon(mS)\gamma$ (experimentally photons are reconstructed by pair conversion in the tracker material) and 3) the charged dipion transitions (further hadronic transitions involve one or more π^0s which are difficult to reconstruct).
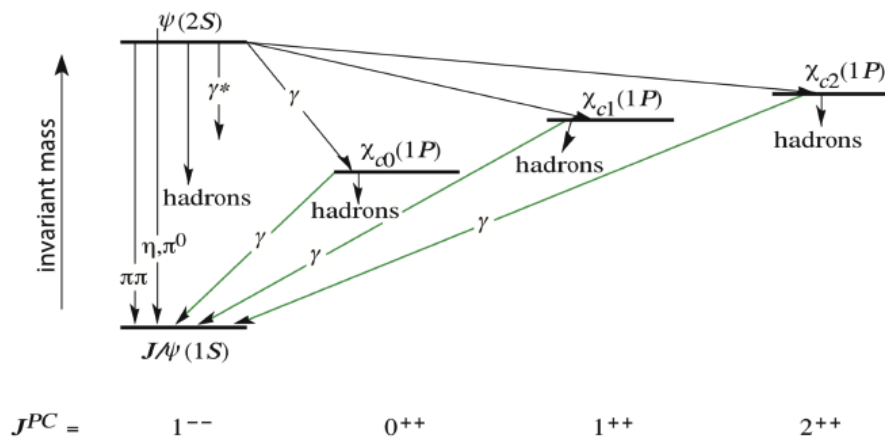
FIGURE 1.2: Charmonium spectrum and decays, limited to the CP-even states, below open charm threshold.

1.3 Hadron Spectroscopy

The bottom-charmed (B_c) meson family provides a unique window to test the non-relativistic limit of quantum chromodynamics (QCD), the strong interaction sector of the standard model of particle physics, because they are the only quarkonium bound states consisting of heavy quarks with different flavors: either $c\bar{b}$ for the positive charged channel or $b\bar{c}$ for the negative one. There is an extra reward on studying these open flavor bound state systems: contrary to charmonium ($c\bar{c}$) and bottomonium ($b\bar{b}$), the B_c mesons can not annihilate into gluons and thus these states are very stable, with narrow widths, at least for those which are below the lowest strong-decay B^*D^* thresholds.

Hadron Spectroscopy has experienced a renaissance in the last two decades thanks to the experimental findings of several new, and unexpected charmonium states at B-factories and at hadron colliders [6]. The development of theoretical models [tetra-quark models, molecules of ordinary hadrons, hadro-charmonium, quark-gluon hybrids] has not been able to provide an unified explanation of these states, so far. For instance the nature of the $X(3872)$ state, namely the first charmonium-like state to be discovered in 2003 [7], is still unknown.

The analyses of LHC Run-I data are contributing to provide new experimental observations and measurements for exotic mesons. CMS has provided some important results, among them it is worthy to mention the study of the production of $X(3872)$ and the search of the neutral bottomonium partner of the $X(3872)$ in the $\Upsilon(1S)\pi^+\pi^-$ final state with Run-I data. These papers show that, despite of the absence of an hadronic identification, CMS can play an important role in this sector of QCD. The search studies are currently being extended by using the Run-II data.
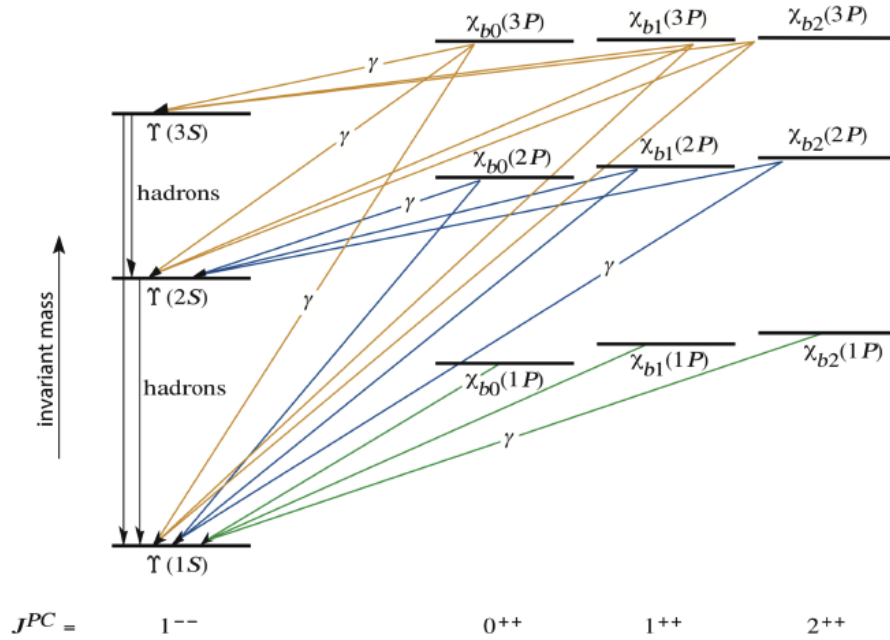
FIGURE 1.3: Bottomonium spectrum and decays, limited to the CP-even
states, below open beauty threshold.

Heavy quark symmetry considerations suggest the existence of a bottomonium counterpart of the $X(3872)$ [8]. Specifically the hadronic molecular model suggests to search it close to $B\bar{B}^*$ threshold (i.e. $m \cong 10.561 GeV$).

By exploiting Run-I data, CMS [9] and ATLAS collaborations searched, for the X_b in the inclusive $\Upsilon(1S)\pi^+\pi^-$ invariant mass distribution produced in pp collisions at the LHC, since the decay $X_b \to \Upsilon(1S)\pi^+\pi^-$ would be analogous to the observed $X(3872) \to$ $J/\psi\pi^+\pi^-$ decay in the charmonium sector.

The two experimental collaborations found no evidence for peaks other then those due to $\Upsilon(2S)$ and $\Upsilon(3S)$ to $\Upsilon(1S)\pi^+\pi^-$ transitions and provided 95% CL upper limits on the ratio R of the inclusive production cross section times the unknown branching fraction of X_b to $\Upsilon(1S)\pi^+\pi^-$:

$$R = \frac{\sigma(pp \to X_b \to \Upsilon(1S)\pi^+\pi^-)}{\sigma(pp \to \Upsilon(2S) \to \Upsilon(1S)\pi^+\pi^-)}$$

According to Karliner and Rosner [10] the analogy of the decay modes is misguided for this particular decay channel. In order to explain this circumstance the following argument holds. If the X_b, the beauty partner of $X(3872)$, has $J^{PC} = 1^{++}$, zero isospin and is near the $B\bar{B}^*$ threshold, the $\Upsilon(1S)\pi^+\pi^-$ decay mode (through an intermediate resonance $\rho \to \pi^+\pi^-$) would violate isospin and be suppressed relative to decays to the isospin-conserving $\Upsilon(1S)\omega$ final state. In the charmonium sector the isospin-allowed $J/\psi\omega$ decay mode is kinematically suppressed by the q-value:

$$Q = m_X - m_{J/\psi} \cong m_{D^0} + m_{D^{*0}} - m_{J/\psi} \cong 774.8 MeV$$

which is about one ω natural width below the nominal mass $m_\omega = 783 MeV$ and the isospin-violating $X(3872) \to J/\psi\rho^0$ has been observed. In the b-quark sector, instead, $m_B + m_{B^*} - m_{\Upsilon(1S)} \cong 1145 MeV$, which is well above m_ω; thus $\Upsilon(1S)\pi^+\pi^-\pi^0$ final state is very likely more relevant than $\Upsilon(1S)\pi^+\pi^-$ for searches of the X_b. Unfortunately the decay final states containing a π^0 are experimentally challenging for the LHC experiments whereas can be viable at Belle-II. No significant signal has been found by Belle-I in the $\Upsilon(1S)\pi^+\pi^-\pi^0$ final state [11].

The strategy for the X_b observation at LHC experiments should instead include the search for the decays $X_b \to \chi_{b1,2}(1P)\pi^+\pi^-$ (where $\chi_{b1,2}(1P) \to \Upsilon(1S)\gamma$) and $X_b \to \Upsilon(3S)\gamma$. By exploiting the data collected at Run-II in the 2016-2018 data taking, CMS has the capability to look for the presence of these radiative decays. CMS has already shown the capability to reconstruct, in the tracker, photons by conversion into electron-positron pairs with enough mass resolution to resolve the $\chi_{c2}(1P)$ and $\chi_{b2}(1P)$ peaks from the $\chi_{c1}(1P)$ and $\chi_{b1}(1P)$ peaks, and also to separate the $\chi_{b1}(3P)$ and $\chi_{b2}(3P)$ peaks.

1.4 Thesis outline

The following thesis is outlined as follows. A review of the charmonium-like and bottomonium-like spectroscopy was presented in Chapter 1 with the aim to provide the motivation for further experimental studies within the current experimental scenario. Chapter 2 is devoted to the illustration of the experimental apparatus used to perform the presented studies; the proton-proton collider (LHC) and the CMS detector are described, focusing on the CMS tracking system and the muon chambers. In Chapter 3 I will give a detailed description of the analysis performed on the observation of two states consistent with the $B_c(2S)^+$ and $B_c(2S)^{*+}$ mesons. Chapter 4 is devoted to the detailed description of the event selection configured to obtain the final mass spectra $\Upsilon(1S)\pi^+\pi^-$ and $\chi_{b1}(1P)\pi^+\pi^-$, together with the extraction of the intermediate $\Upsilon(2S)$, $\Upsilon(3S)$ and $\chi_{b1}(1P)$ signals. Combinatorial background in the final mass spectra is studied also by means of wrong-sign combinations. Finally Chapter 5 provides the details of the calculation of the upper limits on the relative production of X_b states with respect to the chosen normalization channels, including the reconstruction efficiency ratio and the mass resolution estimation across the relevant mass spectrum, obtained by using simulated samples.

Chapter 2

The Large Hadron Collider (LHC) and the Compact Muon Selenoid (CMS) experiment.

2.1   The Large Hadron Collider (LHC).

The Large Hadron Collider (LHC) is the world's largest collider ever built. It consists of a circular tunnel of 27 kilometers long and hosts four major experiments, CMS, ATLAS, ALICE and LHCb. The main purpose of the LHC is to accelerate protons (and heavy Ions) and then collide them in order to study products of such a collisions. With the Pb-Pb collisions we intend to recreate conditions similar to the early stages of the universe and study the quark gluon plasma, whereas for the p-p collisions the main purposes were to search for the Higgs boson (already discovered), search for supersymetric particles, search for new massive vector bosons, to test the standard model (SM) of particle physics and search for the existence of extra dimensions.

The protons are obtained from hydrogen gas. The hydrogen atoms are stripped from their electrons using an electric field to obtain the bare protons. Once we have the protons they pass to a chain of accelerators where they will get to the energies desired for collisions. This chain starts with the Linac 2 (a linear accelerator) where they are accelerated up to 50 MeV and conducted to the Proton Synchrotron (PS) were they reach an energy of 26 GeV and are arranged in bunches of 1.5×10^{11} particles spaced away by 25 ns (50 ns during Run I) from each other. After the PS, the protons are sent to the Super Proton Synchrotron (SPS) where they are accelerated to 450 GeV. The protons finally go to the LHC where they reach the final energy.

The two proton beams travel inside a couple of pipes kept at ultrahigh vacuum and allocated inside the tunnel of the LHC. The beams are bent using dipole magnets and collimated with quadrupoles. Finally, the beams are synchronized for collisions at the different detection points.

The collisions happen in specific places where the results can be detected.

2.2 CMS Experiment

In this section we include a brief description of the CMS detector and the way the information recorded is handled, putting special attention on the muons subdetectors. The order will go from the innermost (the pixel detector) up to the outermost detector (the muon detectors).

We will also include a short description on how the events [1] that contain the physics we are looking for are selected. This is reached using a system of several layers that involve both hardware and software processing, and it is called trigger system.

2.2.1 Tracker detector

The inner tracker system has as a main purpose to reconstruct trajectories of electrically charged particles and secondary vertices. These two tasks have to be performed in a efficient and precise manner.

The entire inner tracker system has a length of 5.8 and a diameter of 2.5m. Due to technical requirements (e.g. the granularity needed for the different layers due to the hit rate density being inversely proportional to the distance from the interaction point) the inner track system is composed by two different technologies: the pixel detector and the silicon strip detector. These two subdetectors and their regions are represented in Figure 2.1. That will establish different requirements in terms of spatial resolution and speed response for these two detectors.

The pixel detector was entirely replaced in the winter of 2016/2017 [12]. The main reason for this upgrade is the buffer overflow in the readout chip, which would have caused a drop in the efficiencies of the track detector of nearly 16% for the luminosity expected at that time for the 2017 and after. Moreover, the pixel detector is the nearest to the interaction point and it is exposed to high radiation conditions which cause a faster damage of the components. Our analysis uses data from before and after the upgrade, for this reason we will describe the pixel detector for the two periods separately.

Pixel detector

The pixel detector before the upgrade consists of three barrel layers at radii of 4.4cm, 7.3cm and 10.2cm and two disks covering a radii between ≈ 6 and 15 cm at each side at $z = \pm 34.5$ and $x = \pm 46.6$ cm from the nominal interaction point in the endcap. Covering a pseudorapidity range of $|\eta| < 2.5$.

It is composed by 1400 modules which contain n+-in-n silicon sensors segmented in pixels, 66 million in total, each one of the size of 100 x 150 μm^2, 48 million in the barrel

---

[1]An **event** is the smallest entity containing the complete information about a given collision.
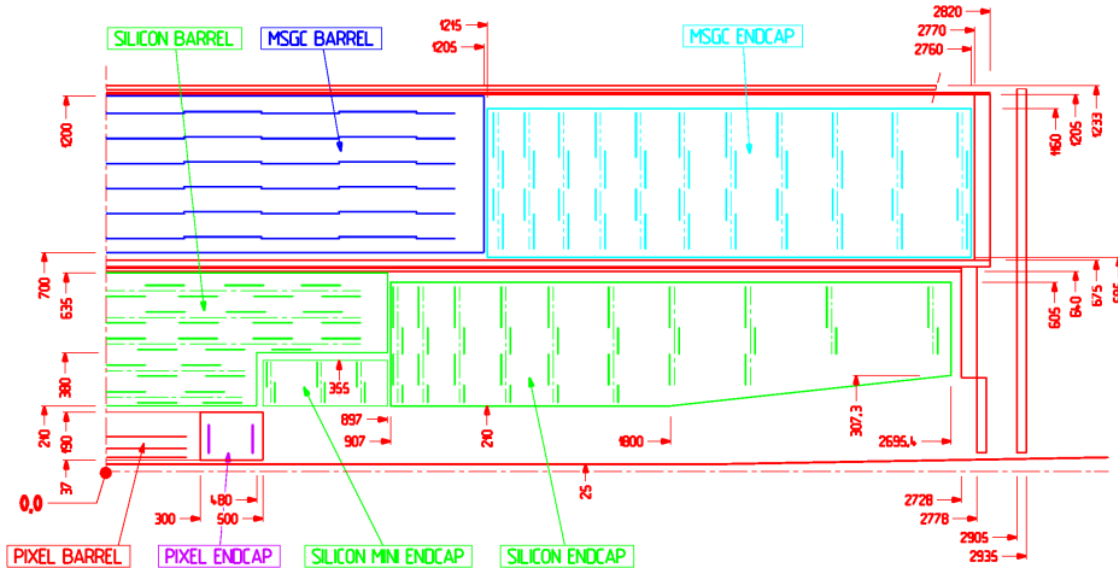
FIGURE 2.1: Tracker system original layout [13]. Every zone of the two
subdetectors is represented with a specific color and labeled.

region and 28 millions in the endcap. The modules are arranged in such a way that there
would be at least three tracking points over all the η-range.

In the barrel region a spatial resolution of 15-20 μm is achieved and in the endcap is
approximately of 15 μm. The readout is performed at 40 MHz.

After the upgrade the number of layers of the pixel detector increased to four located
at radii of 2.9, 6.8, 10.9 and 16cm and the number of disks in the endcap increased to
three at distances 29.1, 39.6 and 51.6cm from the nominal interaction point. With this
new layout there are 4 hits per track in the η coverage up to 2.5. The total number of
pixels increased from 66 millions to 124 millions. The pixel detector geometry can be
seen in the Figure 2.2.

Silicon strip detector

The silicon tracker detector is composed by three different subsystems: the Tracker Inner
Barrel and Disk (TIB/TID), the Tracker Outer Barrel (TOB) and the Tracker EndCaps
(TEC+/TEC-) with 15148 strip detector modules in total.

The TIB/TID surrounds the pixel detector and it is composed of 4 barrel layers (with
a resolution of 23 μm on layers 1 and 2 and 35 μm for the 3 and 4) and 3 disks (with
resolution between 100 μm to 141 μm) at each end, providing up to 4 hits to the track. It
is located between the radii of 20cm and 55 cm and extends in z from -118 to 118 from
the nominal interaction point.

Chapter 2. The Large Hadron Collider (LHC) and the Compact Muon Selenoid (CMS)
experiment.

10
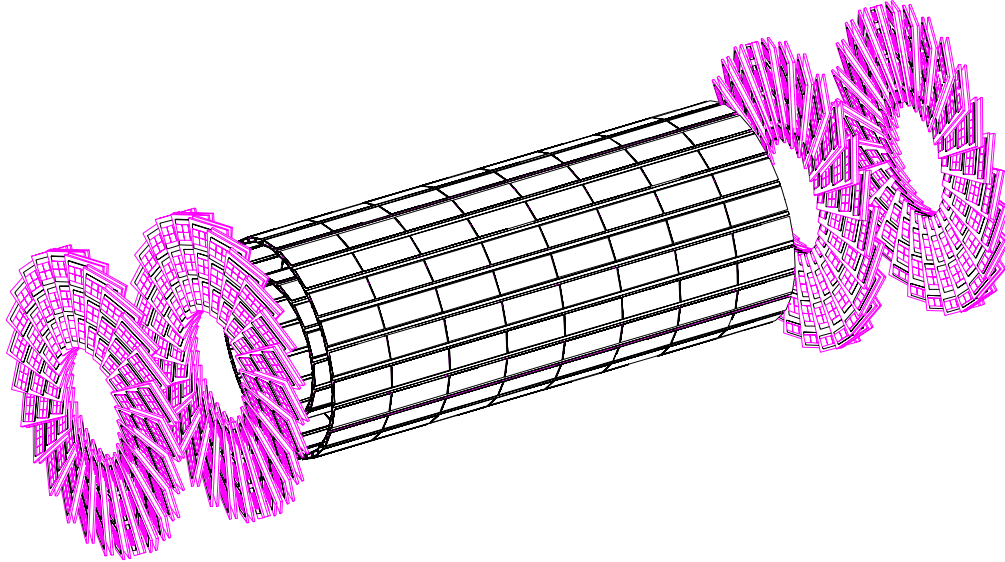
FIGURE 2.2: Pixel detector geometry [13]. Pixel barrel (black) and pixel
endcap (magenta).

The TOB reach radially from the end of the TIB/TID up to 116cm of outer radius. It consists of 6 barrel layers that provides up to 6 r-ϕ measurements with single point resolution of 53 μm and 35 μm, respectively.

Finally, the TECs are composed of 9 disks, providing up to 9 hits points, with a maximum of 7 rings in each disk. It is located from 124 cm to 282 along the z axis at both ends of the TOB and TID.

In addition, the modules in the first two layers and rings, respectively, of TIB, TID, and TOB as well as rings 1, 2, and 5 of the TECs carry a second micro-strip detector module which is mounted back-to-back with a stereo angle of 100 mrad in order to provide a measurement of the second coordinate (z in the barrel and r on the disks). The achieved single point resolution of this measurement is 230μm and 530μm in TIB and TOB, respectively, and varies with pitch in TID and TEC.

2.2.2 Electromagnetic calorimeter

The electromagnetic calorimeter (ECAL) consist of 61 200 lead tungstate crystals in the barrel region and 7 324 at each end in the endcap regions, as shown in the Figure 2.3. The crystals poses a truncated pyramidal shape with a cross-section of approximately 2.2×2.2cm^2 in the front faces and 2.2×2.2cm^2 in the rear faces for the barrel as for the endcap 2.862×2.862cm^2 in the front faces and 2.9×2.9cm^2 in the rear faces. All the crystals are placed in a quasi-projective geometry to avoid cracks aligned with particle trajectories, so that their axes make a small angle (3°) with respect to the vector from the nominal interaction vertex, in both the ϕ and η projections. The crystals are followed by

vacuum phototriodes in the endcap and avalanche photodiodes. A preshower detector in front of the ECAL, which helps to identify neutral pions.
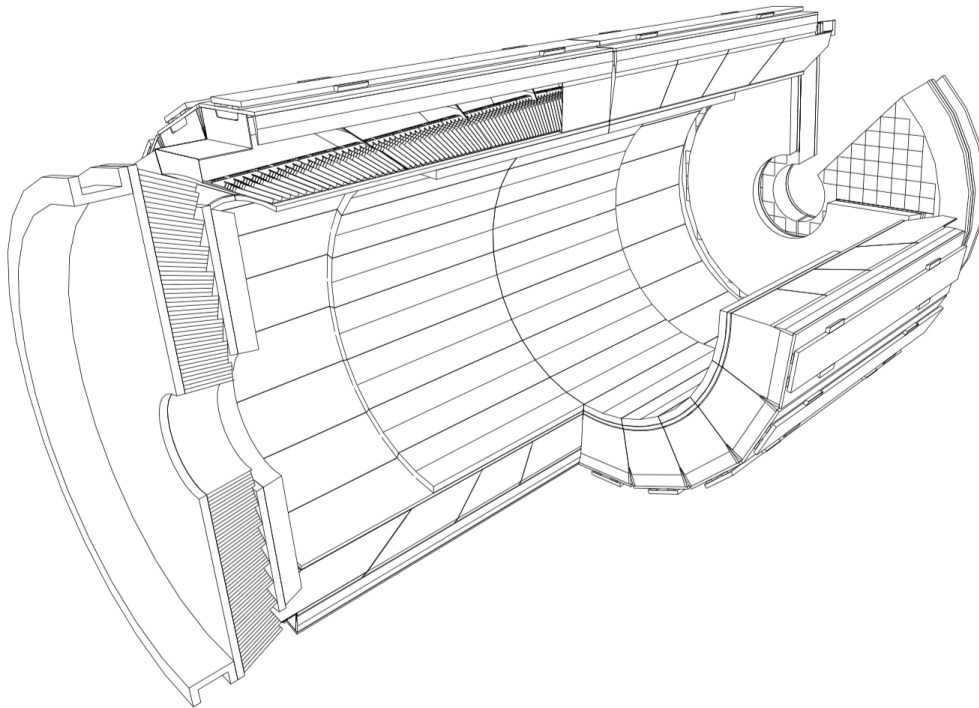
FIGURE 2.3: 3D view of the electromagnetic calorimeter [14].

In the barrel region the crystals are contained in submodules containing a pair of shapes. The submodules are assembled into modules of different type containing 400 or 500 crystals. Finally the four modules are arranged to form a supermodule which contains 1700 crystal. On the other hand, the endcap consists of identically shaped crystals grouped in 5 ×5.

One of the main purpose for the inclusion of the ECAL is detection of the Higgs boson decaying into a pair of photons.

2.2.3 Hadron calorimeter

The hadron calorimeters are designed for the measurement of hadrons energy and they are useful for indirect measurement of neutrinos or exotic particles resulting in apparent missing transverse energy, for this reason the detector has to possess a tight hermeticity and good energy resolution. This detector works with two main components alternated by layers: the absorber and the scintillator. The absorber consists of a 4cm steel plate, followed by 8 5.55cm thick brass plates, six 5.65cm thick brass plate, and a 7.5cm steel back plate. The scintillators will be in charge of producing rapid light pulses when a particle passes through.

Chapter 2. The Large Hadron Collider (LHC) and the Compact Muon Selenoid (CMS) experiment.

12

The hadron calorimeter is composed of four parts. The barrel design (HB) is placed between the electromagnetic calorimeter and the magnet coil at a radii between 1.77m and 2.95m in a pseudorapidity range of $|\eta| < 1.3$. To complement the HB the outer hadron calorimeter is located outside the solenoid. The endcap calorimeters (HE) reach up to $|\eta| = 3$ and beyond it and and up to $|\eta| = 5.2$ the forward calorimeter (HF) is located at a distance of 11.2m from the nominal interaction point.

2.2.4 Superconducting magnet system

The superconducting magnet has a diameter of 6m and length of 12.5m. It was designed to provide a magnetic field for the tracker and muon system of up to 4T. The strong magnetic field increases the efficiency of muon triggering, which plays a big roll in the CMS philosophy.

The solenoid provides a magnetic field parallel to the beam and the particles bend in the transverse plane. This magnetic field will bend electrically charged particles allowing the tracker and muons systems to precisely measure their momentum and electric charge.

Additionally, to the solenoid a yoke composed of 3 layers and with 12 sides is interleaved with the muon detector. The yoke has the task of stopping particles, for a cleaner detection of muon, and as guide for the magnetic field.

2.2.5 Muon detectors

The muon system was built to perform precise and robust measurements of momentum and charge of muons in the entire kinematic range of the LHC. The muon detectors have an additional important role in the trigger system. Three different technologies are involved in the muon detection and triggering in CMS, all of the gaseous particle detectors. The Drift Tube (DT) system is located only in the barrel region covering a pseudorapidity region $|\eta| < 1.2$ where the magnetic field is uniform and mostly contained within the return yoke. The Cathode Strip Chamber (CSC) system is located only in the endcap. Resistive Plate Chamber (RPC) is in the whole eta region up to $|\eta| < 2.1$. The layout of a quadrant of the muon detector is shown in Figure 2.4.

Resistive Plate Chambers

The Resistive Plate Chamber (RPC) has a good time resolution to perform trigger decisions. The RPC consists of chambers, Fig. 2.5, formed by two or four resistive plates, for single and double gap respectively, charged positive and negatively in alternate way. This produces an uniform electric field inside, as in a capacitor. There is a special mixture of gas between each pair of plates. The gas is ionized by the incoming particles and
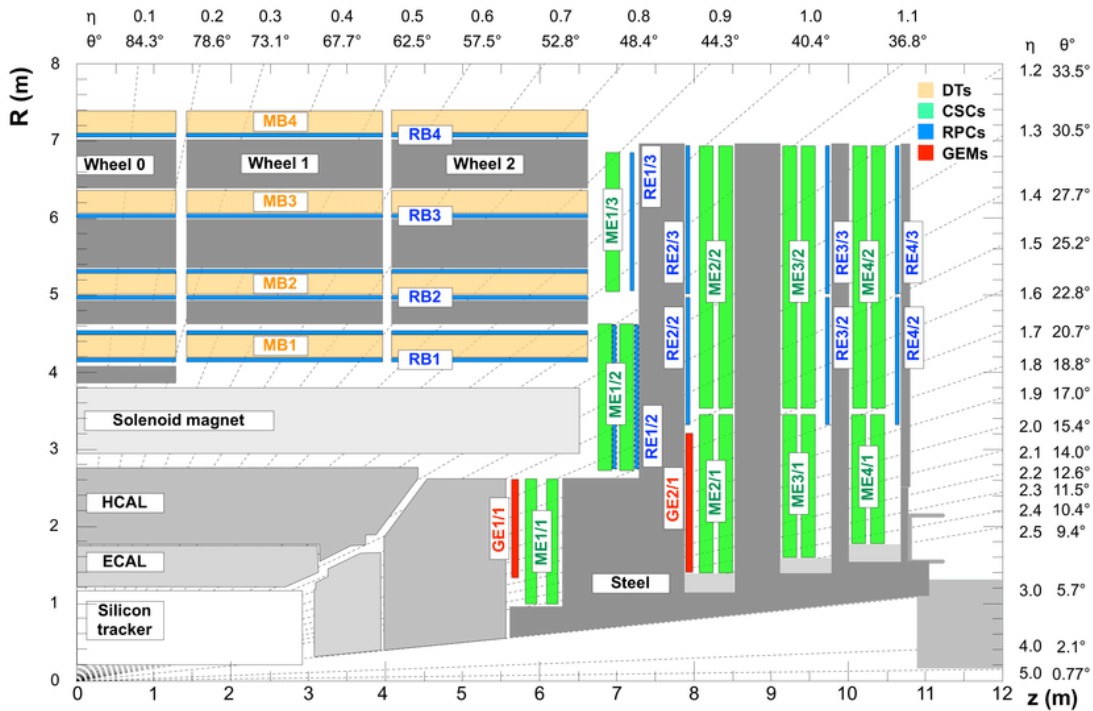
FIGURE 2.4: Muon detectors quadrant. The Drift Tube detector is only in the bars region, the Cathode Strip Chamber detector is located only in endcap regions, and finally the Resistive Plate Chamber is in both barrel and endcap regions [15].

avalanche is produced in the mixture. The electrons are detected by the metallic strips and the information is recorded with the help of the read-out system.

Cathode Strip Chambers

The cathode strip chambers consist of 540 six plane trapezoidal chambers with about 2.5 million wires, 210,816 anode channels and 273,024 precision cathode channels. Every trapezoidal chamber contains wires with a constant spacing between them and they are aligned perpendicular to the radial direction giving a measurement of r coordinate. The cathode planes have strips with a width from 3 to 16cm, depending on the chamber, running in radially in the direction of the r coordinate, giving the measurement of ϕ. The spatial configuration of the strip and wires is shown in Figure 2.6.

The magnetic field in the endcap is weaker than in the barrel and is more inhomogeneous.
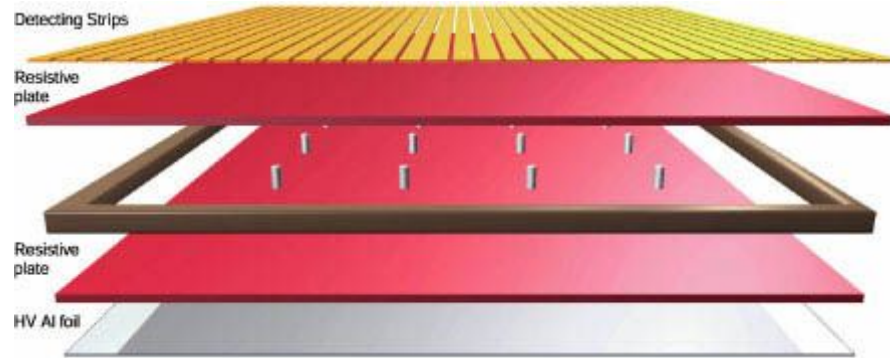
FIGURE 2.5: Schematic representation of a typical RPC chamber [16].

Drift tube system

The DT consists of 4 stations with 5 segmentations of 2.5m along the z axis. The first 3 stations are composed by 60 chambers and the last has 70, with about 195 000 wires in total. Each chamber is formed by 12 layers planes organized in three independent subunits called Super Layers (SL) made up with four planes with parallel wires, shown in Figure 2.8. Two out of the three SL measure the $\phi - r$ projection and the other, placed between them, measures the z coordinate. The outermost station does not have the z measurement.

The four layers are staggered by half a cell, making it possible to use the correlation of the drift times in the different planes to compute the coordinate and the angle of the crossing tracks without any external time tag. The maximum transverse path was chosen to be 21mm, corresponding 380ns of drift time. The mean timer is fast enough to be used in the first-level trigger.

The anode is a 50-μm-diameter gold-plated stainless-steel wire. The field electrode is made of a 16-mm-wide, 50-μm thick aluminium tape, as shown in Figure 2.7.

2.2.6 Trigger

CMS has an average of 10^9 interactions per second, but due to technical specification only up to 100 Hz can be recorded on the online computer farm. For this reason, a method consisting on two steps was designed to select the events containing the physics we want to study. The first step, the Level 1 (L1) trigger, consists on a selection performed by hardware and the second step, High Level Trigger (HLT) is done using software.

Level 1 Trigger

The Level 1 trigger reduces the amount of events on a order of 10^4 to pass approximately 100 kHz to the next step of selection. At this stage only calorimeter and muon systems

radial strips   wires
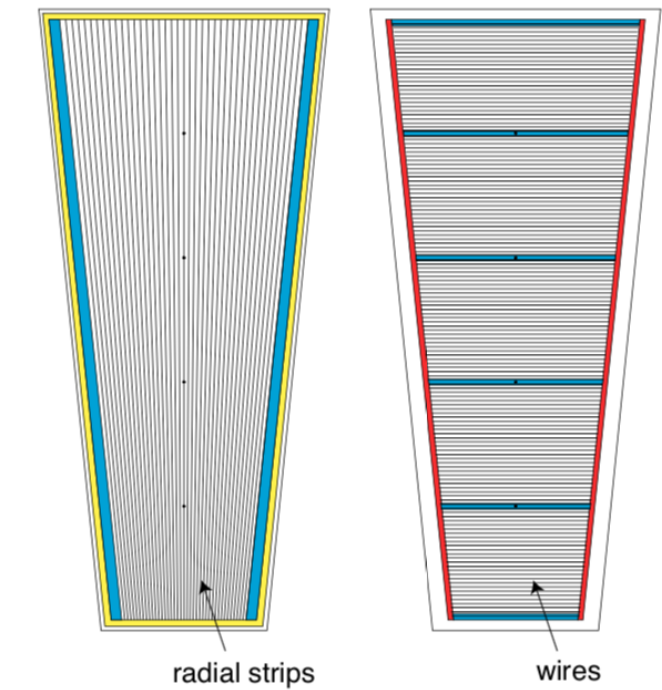
FIGURE 2.6: Spatial configuration of the CSC chamber strips (left) and
wires (right) [16].

are involved. Tracker information is left out due to the limited time for processing.

The information of all the collisions is present until the trigger sends the flag for the event to be accepted or rejected. The decision is based on the presence of local objects such photons, electrons, muons and jets.

High Level Trigger.

This part of the trigger is supposed to reduce the rate of collisions down to 100 Hz.

To optimize the selection the filtering is made in a series of different steps. The first filter takes only into account the information from the calorimeters and the muon systems. This step will reduce the event rate at least one order of magnitude.

After this first selection all the accepted events are sent to a computer farm where they will be filtered again now using the information of all the systems. At this stage the information of L1 trigger can be also accessed and it is completed looking for new combinations and performing new topological calculations.

2.2.7 Data reconstruction

The CMS detector works in a similar way than a photographic camera. Once the collisions are produced in the beam interaction region, the particles enter the tracker. Charged
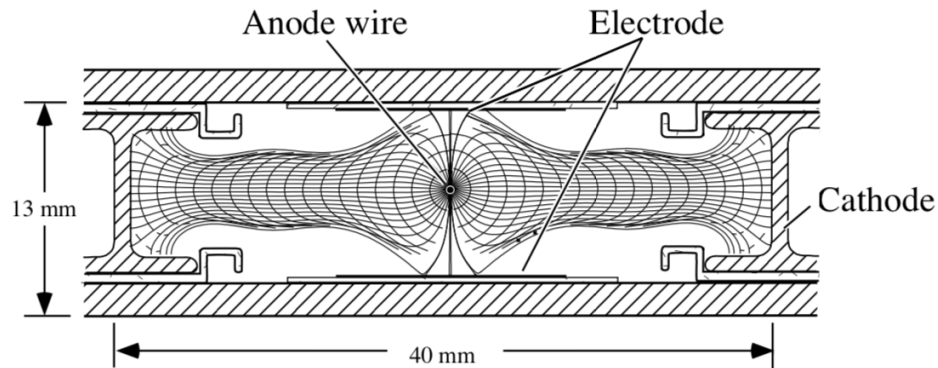
FIGURE 2.7: DT cell diagram [16].
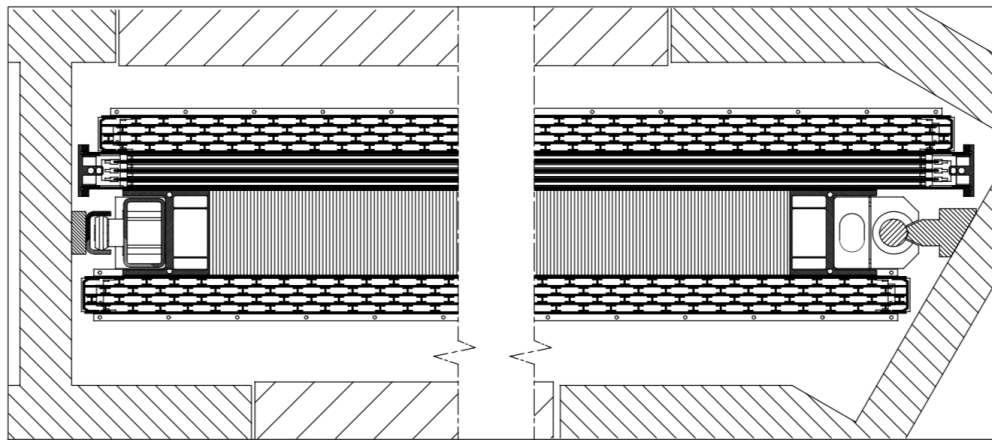
FIGURE 2.8: DT Super Layer setup [16].

particles are detected along their path by it. With this information their tracks and vertices can be computed. Due to the magnetic field produced by the solenoid the charged particles will bend, which allows the momenta and the charge to be measured as well. Following their path the electrons and photons are absorbed by the ECAL. Their direction and energy can be inferred from the electromagnetic showers produced and detected as clusters of energy. On the other hand, hadrons may initiate hadronic showers in the ECAL and be fully absorbed by the HCAL, with this providing information to compute their direction and energy. Muons will normally leave hits on the muon detectors, located outside the calorimeters. Neutrinos would pass undetected. In Figure 2.9 a schematic representation of what is mentioned above can be found.
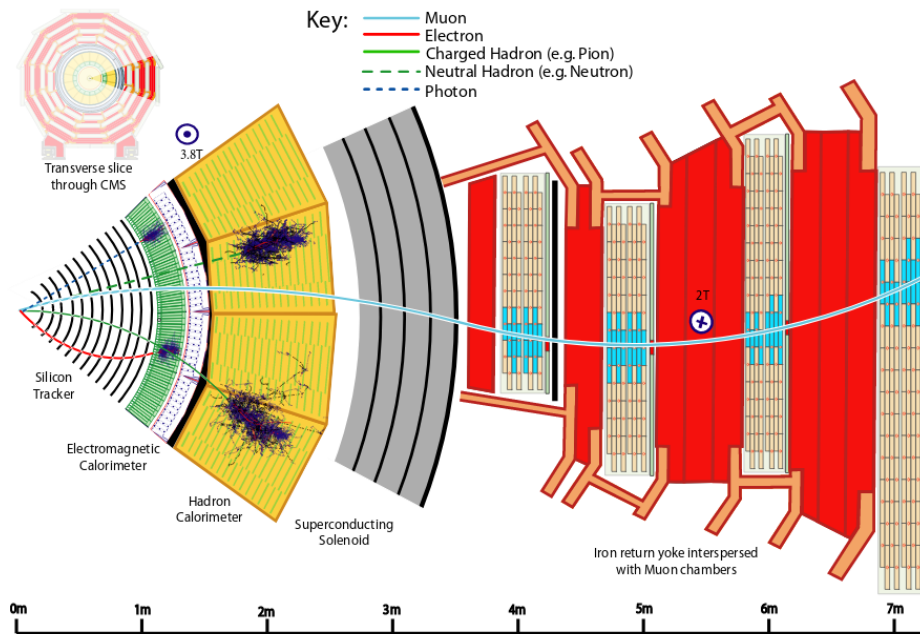
FIGURE 2.9: A sketch of the specific particle interactions in a transverse slice of the CMS detector, from the beam interaction region to the muon detector [17].

2.2.8 CMS Event Data Model

The information produced by the series of detectors and objects calculated from them are stored in the Event Data Model format. In this model the event is the minimal consistent structure, and it is composed by C++ type products. Most of the products contain tracks, cluster, particles, etc. The format of the files is made on ROOT and all the data must be usable interactively. Furthermore, CMS defines different data tiers containing different levels of details. There is RECO, which contains detailed reconstruction outputs allowing to apply new calibrations and alignments, and reprocess most of the products. AOD is composed of a subset of RECO, chosen to satisfy needs of a large fractions of the analysis studies. To further reduce the size of the dataset, given the increased size of the data collected by CMS, MINIAOD format was produced, where very reduced and optimized output is stored. Part of the studies in the current thesis use MINIAOD format.

Chapter 3

Observation of two excited B_c^+ states

The B_c^+ meson was discovered by CDF in 1998 [18]. It is the lowest mass bound state containing a charm quark and a bottom anti-quark. Its production mechanism differs from the $b\bar{b}$ or $c\bar{c}$, since the lowest order mechanism for creating of $c\bar{b}$ system is at least of α_s^4: $q\bar{q}, gg \rightarrow B_c^+ b\bar{c}$, being the gluon-gluon contribution the dominant one at the LHC. Experimental information has been limited, due to this reduced production rate. However, thanks to the higher luminosities available at LHC its knowledge has improved.

Recently, in 2014, the ATLAS collaboration reported the observation of a new state whose mass is consistent with predictions for the $B_c(2S)^+$, the second S-wave state of the B_c^+ meson [19]. The spectrum of the $c\bar{b}$ states has been calculated by several authors [20, 21, 22, 23, 24, 25, 26, 27]. Figure 3.1 shows one of these predicted spectra.

The properties of B_c^+ ($c\bar{b}$ family) mesons are a special case in quarkonium spectroscopy as they consist of heavy quarks with different flavors, due to this, they cannot annihilate into gluons. So, the excitations, in a cascade way, decay to the ground state with the emission of photons and pion-pion pairs.

The $B_c(2S)^+$ meson, observed by ATLAS, was reconstructed from its $B_c^+ \pi^+ \pi^-$ decay (followed by $B_c^+ \rightarrow J/\psi \pi^+$). They found a local significance of 5.2σ. So far, this observation has not been confirmed. LHCb with a signal yield of B_c^+ decays of 3325 ± 73 concluded that "No significant signal is found", in the search for the excited states $B_c(2^1S_0)^+$ (called $B_c(2S)^+$) and $B_c(2^3S_1)^{+1}$ (called $B_c(2S)^{*+}$), arguing that the detection efficiency of ATLAS should be large in comparison with them [28].

Theoretical calculations predicts $B_c(2^3S_1)^+$ could have a larger production rate than $B_c(2^1S_0)^+$, however it decays to $B_c^{*+}\pi^+\pi^-$, followed by $B_c^{*+} \rightarrow B_c^+\gamma$. According to [20, 21, 22, 23, 24, 25, 26, 27], the masses of $B_c(2S)^{*+}$ is in the range 6.881–6.914 GeV, $B_c(2S)^+$ in 6.835–6.882 GeV, B_c^{*+} in 6.308–6.341 GeV, and B_c^+ in 6.247–6.286 GeV. Being the mass separation of B_c^{*+} to B_c^+ in the range 41–80 MeV, this γ is a very-low energy photon which is challenging to reconstruct and will be lost. Under this assumption the decay

---

[1] In the spectroscopy notation $n^{2s+1}L_J$ used, n is the radial quantum number, s is the total spin of the two valence quarks, L is their relative angular momentum, and J is the total angular momentum of the system, in this notation $B_c(2^3S_1)^+$ denotes the $B_c(2S)^{*+}$ state.
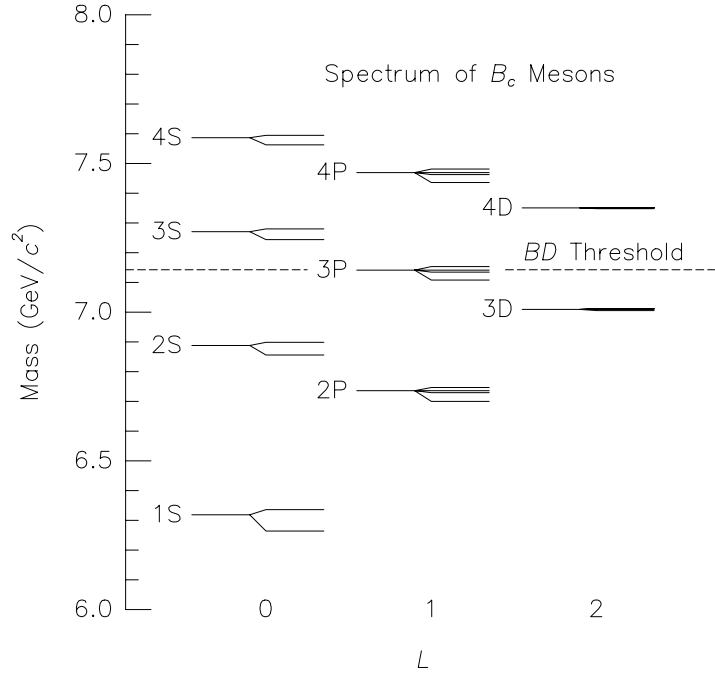
FIGURE 3.1: The spectrum of $c\bar{b}$ states. Taken from [24]

chain $B_c(2S)^{*+} \rightarrow B_c^{*+}\pi^+\pi^- \rightarrow B_c^+(\gamma_{\mathrm{lost}})\pi^+\pi^-$ should manifest in the $B_c^+\pi^+\pi^-$ mass spectrum as a "shifted" narrow peak. This mass-peak should be centered at $M(B_c(2S)^+)-\Delta M$, where

$$\Delta M \equiv [M(B_c^{*+}) - M(B_c^+)] - [M(B_c(2S)^{*+}) - M(B_c(2S)^+)] \tag{3.1}$$

and should range in 0–35 MeV, for the above predictions. LHCb argues, as well, that the most probable interpretation of ATLAS result is that observed $B_c(2S)^+$ states is in fact $B_c(2S)^{*+}$ or the sum of $B_c(2S)^+$ and $B_c(2S)^{*+}$ under the $\Delta M \sim 0$ scenario. However, if ΔM is different from zero, the reconstruction of the decay channel $B_c(2S)^+ \rightarrow B_c^+\pi^+\pi^-$ will show a two-peak structure, with the lower peak actually representing the higher $B_c(2S)^{*+}$ mass state.

At CMS a preliminary study on this decay channel has already been performed and discussed in [29] using 8 TeV dataset. In this chapter we describe the studies on the 2016–2018 datasets, at 13 TeV center of mass.

The analysis is based on the reconstruction of $B_c(2S)^{(*)+}$ [2] states using their hadronic decay into the $B_c^+\pi^+\pi^-$ final state, with B_c^+ decaying to $J/\psi\pi^+$ and J/ψ to two muons.

We report the observation for the of the two spin states and provide the measure of their masses.

---

[2]$B_c(2S)^{(*)+}$ denotes either $B_c(2S)^+$ or $B_c(2S)^{*+}$, while $B_c^{(*)+}$ denotes either B_c^+ or B_c^{*+}. Charge-conjugate candidates are implied.

3.1 Data and Monte-Carlo samples

The study reported here, regarding the reconstruction of $B_c(2S)^{(*)+}$ states in pp collisions at $\sqrt{s} = 13$ TeV, uses data collected by CMS in the years 2016, 2017 and 2018. The 2018 dataset uses all available re-reco data of eras A, B and C. Era D is considered as re-reco. Table 3.1 shows the list of data samples and respective run ranges, for the years 2016-2018.

TABLE 3.1: Data samples used in the current analysis. The names of the datasets are used internally by the CMS collaboration.

Data set	Run range
Run2016B-07Aug17-v1	273150–275376
Run2016C-07Aug17-v1	275656–276283
Run2016D-07Aug17-v1	276315–276811
Run2016E-07Aug17-v1	277420–277305
Run2016F-07Aug17-v1	277932–278808
Run2016G-07Aug17-v1	278820–280385
Run2016H-07Aug17-v1	281207–284035
Run2016H-07Aug17-v1	284036–284068
Run2017B-17Nov2017-v1	297031–299329
Run2017C-17Nov2017-v1	299368–302029
Run2017D-17Nov2017-v1	302031–302663
Run2017E-17Nov2017-v1	303572–304797
Run2017F-17Nov2017-v1	305040–306460
Run2018A-17Sep2018-v1	315252–316995
Run2018B-17Sep2018-v1	317080–319310
Run2018C-17Sep2018-v1	319337–320065
Run2018D-PromptReco-v2	320673–325175

The events were collected with a dimuon trigger requiring an opposite-sign muon pair of invariant mass in the range 2.9–3.3 GeV, called `HLT_DoubleMu4_JpsiTrk_Displaced_v*`. This HLT path required a dimuon vertex fit χ^2 probability larger than 10% and a distance of closest approach between the two muons smaller than 0.5 cm ($\mathrm{MaxDCAMuMu} < 0.5$ cm). The selected muons had to be in the η region of the CMS detector, $|\eta| < 2.5$, and they had to have a transverse momentum larger than a certain threshold, $p_\mathrm{T} > 4.0$ GeV.

Table 4.3 lists the specific HLT trigger paths used in the analysis, as well as the respective recorded and effective integrated luminosities, L_int.

The HLT paths had different L1 seeds (The nomenclature for L1 seeds and other technical details are used internally by CMS collaboration):

- 2016, activated at lumi $< 1.0e34$ Hz/cm2:
  `DoubleMu_10_0_dEta_Max1p8 OR`

- 2016, activated at lumi $< 1.1e34$ Hz/cm2:
  `DoubleMu0er1p6_dEta_Max1p8_OS OR`

- 2016, always on:
  `DoubleMu0er1p4_dEta_Max1p8_OS OR`

- 2016, activated at lumi $< 1.2e34$ Hz/cm2:
  `DoubleMu_11_4 OR`

- 2016, always on:
  `DoubleMu_12_5`

- 2017–2018, (no p_T cut, $|\eta| < 1.5$, *high quality*, opposite-sign, deltaR(MuMu)< 1.4):
  `DoubleMu0er1p5_SQ_OS_dR_Max1p4 OR`

- 2017–2018, ($p_T > 4$, *high quality*, opposite-sign, deltaR(MuMu)< 1.2):
  `DoubleMu4_SQ_OS_dR_Max1p2`

Table 4.3 also presents the integrated luminosity of the samples, separately for each running year and HLT trigger period, both before and after applying the data certification requirement, as computed with the `brilcalc` tool [30]. The total integrated luminosity is also provided.

TABLE 3.2: Trigger paths used in this analysis and respective integrated luminosities.

HLT path	L_{int} (fb^{-1})	
	Recorded	Certified
HLT_DoubleMu4_JpsiTrk_Displaced_v2	2.914	2.795
HLT_DoubleMu4_JpsiTrk_Displaced_v3	5.540	5.297
HLT_DoubleMu4_JpsiTrk_Displaced_v4	10.047	9.622
HLT_DoubleMu4_JpsiTrk_Displaced_v5	10.093	9.676
HLT_DoubleMu4_JpsiTrk_Displaced_v7	9.070	8.727
HLT_DoubleMu4_JpsiTrk_Displaced_v8	3.145	3.009
HLT_DoubleMu4_JpsiTrk_Displaced_v9	2.084	1.930
HLT_DoubleMu4_JpsiTrk_Displaced_v10	1.516	1.367
HLT_DoubleMu4_JpsiTrk_Displaced_v11	9.133	8.451
HLT_DoubleMu4_JpsiTrk_Displaced_v12	24.860	23.654
HLT_DoubleMu4_JpsiTrk_Displaced_v13	2.963	2.810
HLT_DoubleMu4_JpsiTrk_Displaced_v14	0.901	0.862
HLT_DoubleMu4_JpsiTrk_Displaced_v14	9.399	9.092
HLT_DoubleMu4_JpsiTrk_Displaced_v15	54.689	52.511
Total luminosity		140

The quoted luminosity values have been evaluated taking into account that the analysis is restricted to data collected in certified lumisections, as listed in the following JSON files, respectively for the 2016, 2017, and 2018 periods:

- `Cert_271036-284044_13TeV_23Sep2016ReReco_Collisions16_JSON_MuonPhys`

- `Cert_294927-306462_13TeV_EOY2017ReReco_Collisions17_JSON_MuonPhys`

- `Cert_314472-325175_PromptReco_Collisions18_JSON_MuonPhys`

For determination of the efficiencies and fitting modeling we rely on PYTHIA 8 [31] simulations. They are prepared to reproduce the CMS running conditions as closely as possible to the data, in 2016 and 2017. The $B_c(2S)^{*+}$, $B_c(2S)^+$ and B_c^+ Monte Carlo (MC) samples were produced with the dedicated generator BCVEGPY 2.2 [32], which produce events in Les Houches Event (LHE) standard format [33]. Those events are passed to CMS PYTHIA 8 interface to simulate the hadronizing process and to EvtGen for the final decaying [34]. QED Final state radiation is modeled by PHOTOS [35].

For these simulations we apply minimal kinematical requirements in order to speed up the generation: In BCVEGPY the B_c^+'s mesons are required to have $p_T > 10.0$ GeV and $|y| < 3$. While the muons, daughters of the J/ψ, are required to have $p_T > 3.5$ GeV and $|\eta| < 2.5$ and the pion, daughter of the B_c^+, must have $p_T > 1.0$ GeV and $|\eta| < 2.5$.

Samples were also fully simulated with digitization, trigger simulation and reconstruction following the configuration available in `RunIISummer16`, `RunIIFall17`, and `RunIIAutumn18` campaigns. The simulated events include multiple proton-proton interactions in the same or nearby beam crossings (pileup), with the distribution matching that observed in data.

For studies related with the determination of the natural width of the $B_c(2S)^+$ system, we generate single particle events, based on PYTHIA 8, where the p_T of the $B_c(2S)^+$ meson was set to follow the p_T distribution of real J/ψ data [36] and the rapidity was set flat, these choices are based on the fact the p_T shapes are similar for the two particles and irrelevant for the natural width studies.

The generated events were fully simulated, following the same receipt as in the MC campaigns mentioned above. The masses used for these samples are set to: $M(B_c^+)$ = 6.2749 GeV, $M(B_c^{*+})$ = 6.3400 GeV, $M(B_c(2S)^+)$ = 6.8630 GeV, and $M(B_c(2S)^{*+})$ = 6.9030 GeV.

3.2   Event reconstruction and Selection

The candidate $B_c(2S)^{(*)+}$ is the result of the pions and muon selection, of the J/ψ selection, of the B_c^+ selection and of the requirements imposed on the relation between the B_c^+ candidate and the pions candidates. If several $B_c(2S)^+$ candidates are found in the same event, only the one with the highest p_T value, is kept. This approach was tested on Monte Carlo simulation, given a better reconstruction efficiency (of the order of 6%) than just using the the vertex probability, as used in several other similar analysis. In the following we describe the process in detail.

3.2.1 J/ψ **reconstruction**

The J/ψ quarkonium states were reconstructed taking advantage of the standard CMS muon reconstruction. The Muon-POG-approved *Soft Muon* selection [37] used means the following requirements. The tracker track is matched with at least one segment in any muon station, in both x and y coordinates (*TMOneStationTight*), and arbitrated. The track needs to qualify as *high-purity* and must include more than five hits in the tracker layers, at least one of them being in a pixel layer. The impact parameter of the single muons, with respect to the primary vertex, must be smaller than 0.3 cm in the transverse plane and smaller than 20 cm along the beam axis. The single muons also need to have $|\eta| < 2.4$ and, a minimum transverse momentum of $p_{\mathrm{T}} > 4.0$ GeV.

Trigger matching is applied for these muons, so that the selected ones, at the offline level, are the ones that triggered the detector readout. The muons are combined in opposite-sign pairs to form the J/ψ candidates, which are kept in the analysis if they have invariant mass between 2.9 and 3.3 GeV. The dimuon vertex have a χ^2 probability greater than 10%, $\Delta R(\mu\mu) < 1.2$ and $\cos\theta > 0.98$, where $\cos\theta = \vec{L}_{xy} \cdot \vec{p}_{\mathrm{T}}/(|L_{xy}| \cdot |p_{\mathrm{T}}|)$ and $\vec{L}_{xy}$ and $\vec{p}_{\mathrm{T}}$ refer to the transverse decay length and momentum of the J/ψ meson. After above cuts, Figure 3.2 shows the dimuon mass distributions for the three data taking periods. The differences in number of J/ψ candidates for 2016, 2017, and 2018 are expected because of differences in trigger, for instance HLT path for 2017/2018 requires a track with $p_{\mathrm{T}} > 1.2$ GeV, while 0.9 for 2016, and an impact parameter significance of $dxy/\sigma_{dxy} > 2$ (> 0 for 2016), forming a good vertex with J/ψ.

3.2.2 B_c^+ **reconstruction**

From the sample of collected J/ψ events, candidate B_c^+ mesons are reconstructed by combining a J/ψ candidate with a track. This last track is denoted as π_1 hereafter. No trigger matching is applied to this track, since we are just using the feature of having a displaced J/ψ, rather than the complete decay channel. Only tracks that pass *high-purity* are used. The B_c^+ meson candidate is fitted to a common vertex with the appropriate pion mass assigned to the charged track and the dimuon invariant mass constrained to the world-average J/ψ mass [38]. Primary vertexes (PV) are fitted from the reconstructed tracks. The PV having the smallest pointing angle, defined as the angle between the reconstructed B_c^+ hadron momentum and the vector joining the PV with the B_c^+ decay vertex, is used. The chosen PV was refitted removing all tracks from B_c^+ candidate, if they were present.

The charged hadron tracks, π_1, are required to have at least 1 pixel hits, at least 5 tracker hits (strips and pixels together), impact parameter significance $dxy/\sigma_{dxy} > 2$ and must have a $|\eta| < 2.4$. The p_{T} of the charged hadron tracks are required to be greater than 3.5 GeV, while The p_{T} of the B_c^+ hadrons are required to be greater than
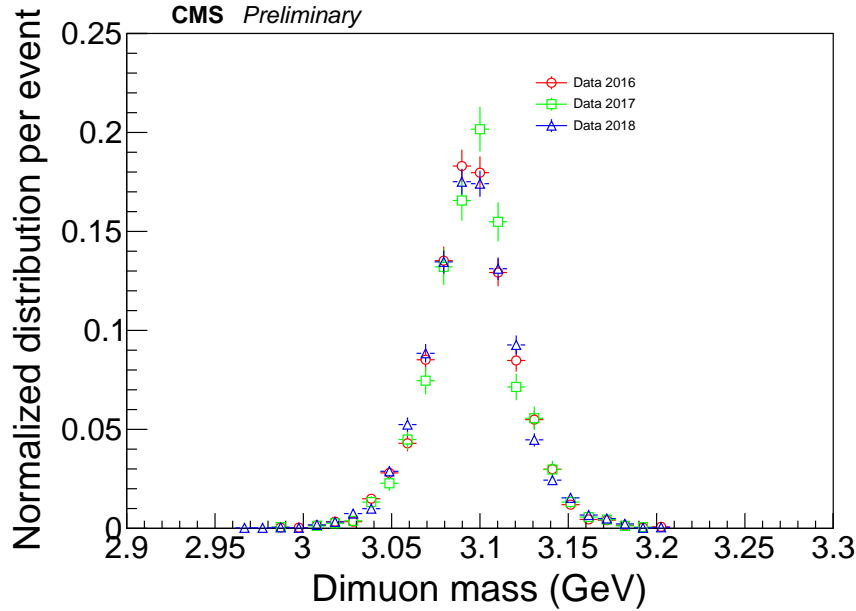
FIGURE 3.2: Dimuon mass distributions, in the J/ψ region, as measured for the 2016, 2017 and for the 2018 data taking periods.

15 GeV. The B_c^+ mesons must have a rapidity of $|y| < 2.4$, $ct > 0.01$ cm, and a vertex χ^2 probability greater than 10%. The cuts used in this selection are based on previous studies within the PAG, however, further studies shows that they are robust enough as can be seen in Appendix A.3.

The $B_c^+ \to J/\psi\pi^+$ invariant mass distribution after the selection described above is shown in Figure 3.3, which is fitted with an unbinned maximum-likelihood (ML) estimator. The $J/\psi\pi^+$ invariant mass distribution is fitted with two Gaussian functions with a common mean for the B_c^+ signal and the background is parametrized by the combination of the first order Chebyshev polynomial function (for the combinatorial contribution) and an Argus function which describes the partially reconstructed B_c^+ decays, $B_c^+ \to J/\psi + X$. They Argus shape of this contribution was inferred from the $B_c^+ \to J/\psi + \rho^+(\to \pi^+\pi^0)$ simulated sample. The parameters of the Argus function are determined from data, since these simulated events are just a small part of all unknown contributions of this kind. An additional background contribution from $B_c^+ \to J/\psi K^+$ decays is modeled from a simulated sample of $B_c^+ \to J/\psi K^+$ events, and its contribution is constrained using the value of the branching fraction relative to $J/\psi\pi^+$ [39], scaled by the observed ratio of reconstructed efficiencies of these two decays. All the fitted parameters are listed in Table 3.3, where $M_{B_c^+}$, $\sigma1_{B_c^+}$, and $\sigma2_{B_c^+}$ are the measured mass and width of the Gaussian functions describing the B_c^+ meson respectively, with f_g as the corresponding fraction between the two Gaussian. $N_{B_c^+}$ is the B_c^+ yield, N_{bkg} is the

yield of the background events. a_{pol}, $d0$ and $d1$ are the parameters of the polynomial and Argus functions, respectively. The quoted uncertainties only reflect statistical effects. The quoted values refers to the B_c^+ mass window 5.9–6.6 GeV.
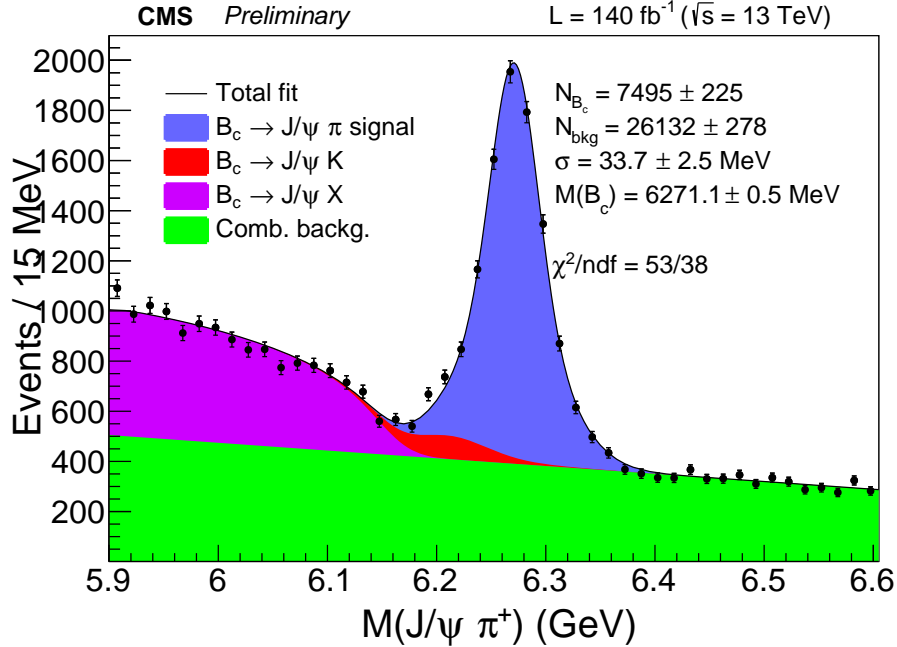
FIGURE 3.3: The $J/\psi\pi^+$ invariant mass distribution (2016+2017+2018) with the solid line representing the total fit, the signal component in blue, the combinatorial background in green, and the contribution from $B_c^+ \to J/\psi K^+$ decays in red, and partial reconstructed decays in magenta. The vertical bars on the data points represent the statistical uncertainties. Quoted values correspond to the mass window shown in the plot.

Figure 3.4 shows the mass distributions for the 2016, 2017 and 2018 data taking periods and the fitted parameters are listed in Table 3.4. The partially reconstructed B_c^+ decays are fixed from the default fit (see Figure 3.3). The yields difference observed in the 2016 and 2017 taken periods is justified by the tighter trigger present in 2017. The effective mass resolutions of 34.7 ± 5.9 MeV and 33.6 ± 6.9 MeV for 2016 and 2017 respectively are consistent with the ones for MC, where we reconstruct 35.1 ± 1.0 MeV and 34.2 ± 1.0 MeV respectively. The observed differences in yield between 2016 and 2017 data taking periods is expected due to the trigger differences, as has already been mentioned. These differences are reduced and get consistent with the amount of luminosity being available in each period when the cuts are tightened. The shape of the background looks consistent when the two datasets are normalized to each other.

$m_{B_c^+}$ (GeV)	6.2711 ± 0.0005
$\sigma1_{B_c^+}$ (GeV)	0.0210 ± 0.0015
$\sigma2_{B_c^+}$ (GeV)	0.0420 ± 0.0037
f_g (GeV)	0.47 ± 0.09
$N_{B_c^+}$	7495 ± 225
N_{bkg}	26132 ± 278
a_{pol}	-0.30 ± 0.04
$d0$	-3.00 ± 0.00
$d1$	6.16 ± 0.00

TABLE 3.3: Parameters fitted to the $J/\psi\pi$ mass distribution for 2016+2017+2018 data sample.
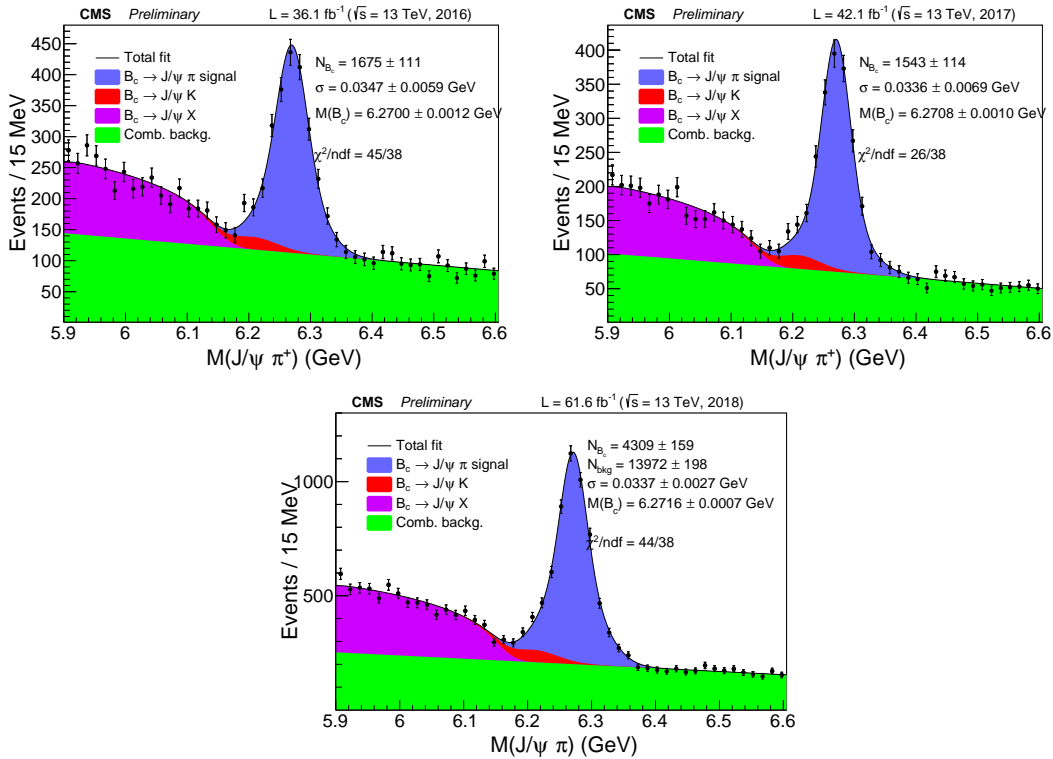
FIGURE 3.4: The $J/\psi\pi^+$ invariant mass distribution, for 2016 (top left), 2017 (top right) and 2018 (bottom) data taking periods .

TABLE 3.4: Parameters fitted for the $J/\psi\pi$ mass distribution, 2016 (top left), 2017 (top right) and 2018 (bottom).

$m_{B_c^+}$ (GeV)	6.2700 ± 0.0012		$m_{B_c^+}$ (GeV)	6.2708 ± 0.0010
$\sigma 1_{B_c^+}$ (GeV)	0.0234 ± 0.0038		$\sigma 1_{B_c^+}$ (GeV)	0.0223 ± 0.0023
$\sigma 2_{B_c^+}$ (GeV)	0.0429 ± 0.0092		$\sigma 2_{B_c^+}$ (GeV)	0.0478 ± 0.0136
f_g (GeV)	0.49 ± 0.23		f_g (GeV)	0.65 ± 0.15
$N_{B_c^+}$	1675 ± 111		$N_{B_c^+}$	1543 ± 114
N_{bkg}	7132 ± 141		N_{bkg}	4993 ± 136
a_{pol}	-0.29 ± 0.07		a_{pol}	-0.37 ± 0.09
$d0$	-3.00 (fixed)		$d0$	-3.00 (fixed)
$d1$	6.16 ± 0.01		$d1$	6.16 ± 0.01

$m_{B_c^+}$ (GeV)	6.2716 ± 0.0007
$\sigma 1_{B_c^+}$ (GeV)	0.0195 ± 0.0018
$\sigma 2_{B_c^+}$ (GeV)	0.0407 ± 0.0038
f_g (GeV)	0.41 ± 0.09
$N_{B_c^+}$	4309 ± 159
N_{bkg}	13972 ± 198
a_{pol}	-0.26 ± 0.06
$d0$	-3.00 (fixed)
$d1$	6.17 ± 0.01

3.2.3 $B_c(2S)^{(*)+}$ **reconstruction**

From the sample of collected B_c^+ events, candidate $B_c(2S)^+$ and $B_c(2S)^{*+}$ are reconstructed by combining a B_c^+ candidate with two tracks. These two tracks are denoted as π_2 and π_3 hereafter. The states $B_c(2S)^+$ and $B_c(2S)^{*+}$ are supposed to be produced at the PV and then strongly decay to $B_c^+\pi^+\pi^-$ and thus its production point and its decay vertex virtually coincide. Therefore, the daughter pions are required to be tracks used in the PV fit (We follow the same procedure as we did in BPH-16-002 [40]) . These pion candidates, π_2 and π_3, are also required to pass standard *high-quality and purity* track requirements, to have at least 1 pixel hits, at least 5 tracker hits and to have opposite signs. The p_T of the π_2 and π_3 tracks are required to be greater than 0.8 and 0.6 GeV, respectively. As a cross-check we require a dipion invariant mass less than 0.6 GeV, the study is shown in Appendix A.3. We have to notice that the selection is somehow insensitive to the other p_T requirements (of B_c^+ and the hard pion), see Appendix A.3. There, you can also found a consistency check of the selection of the cuts in the soft pions and the selection of the best candidate. That shows that the current reconstruction strategy is robust enough.

The mass of the B_c^+ meson candidates is restricted to lie within 6.2 to 6.355 GeV, which roughly correspond to about -2 to $+2.5\sigma$ of the reconstructed mass peak. The $B_c(2S)^+$ and $B_c(2S)^{*+}$ hadron candidates must have a rapidity of $|y| < 2.4$, and the χ^2

probability of the vertex build with B_c^+ and the two selected tracks has to be greater than 10%. Peaks are sought in the distribution of the variable $Q = M(B_c^+\pi^+\pi^-) - M(B_c^+) - 2M(\pi)$, where $M(B_c^+)$ is the offline reconstructed invariant of the B_c^+ candidate, $M(B_c^+\pi^+\pi^-)$ is the invariant mass of the B_c^+ candidate combined with two charged pion candidates as obtained from the kinematical vertex fit, and $m_{B_c^+}$ is the PDG B_c^+ mass. This definition improves the invariant mass resolution as verified by MC simulations.

The measured Q distribution is presented in Figure 3.5. An unbinned extended maximum-likelihood fit is performed on this distribution. The fit includes a third-order Chebyshev polynomial to model the background and a Single Gaussian function for the signal for any of the two $B_c(2S)^{(*)+}$ states. The fitted number of signal events are 54 ± 10 and 67 ± 10 for $B_c(2S)^+$ and $B_c(2S)^{*+}$, respectively. The fit χ^2 is 36, for 39 degrees of freedom. The PDF of the fit is, then, given by

$$PDF(M) = N_1 \cdot f_1(M) + N_2 \cdot f_2(M) + N_{bkg} \cdot f_{bkg}(M) \quad , \tag{3.2}$$

where N_1 and N_2 are the $B_c(2S)^{*+}$ and $B_c(2S)^+$ yields, respectively, and N_{bkg} is the yield of background events, in the full mass range considered in the fit.

N_1, N_2, N_{bkg}, the mass and width parameters of the $B_c(2S)^{*+}$ and $B_c(2S)^+$, ΔM, Q_2, σ_1 and σ_2, are left free in the fit, as well as, the coefficients of the third-order Chebyshev polynomial. The estimated contribution of the partial B_c^+ decays was found to be negligible, then no contribution is considered in the Q distribution, but the component associated to $B_c^+ \to J/\psi K^+$ decays, was found to have the same shape as the signal, but shifted 1 MeV to the left, we add that component to the nominal fit, with a weight estimated 5% obtained after from the B_c^+ mass distribution cutted at 6.2-6.355 GeV. Variations to this contribution are considered in the systematic evaluations.

In order to validate the fit, several MC samples were generated. In all the cases the values recovered are in statistical agreement with the inputs. All the fitted parameters are listed in Table 3.5, where the quoted uncertainties only reflect statistical effects. The signal peak structure represent the predicted states $B_c(2S)^+$ and $B_c(2S)^{*+}$ with a local significance larger than five standard deviations. This significance is obtained taking the ratio of the likelihood made under the hypotheses of two peaks or a single one. It is important to mention that the left peak represents the "shifted" $B_c(2S)^{*+}$ state, which actually has higher mass and we are unable to fully reconstruct due to the presence of the very low energy photon. Scanning the $B_c(2S)^{*+}$ Monte Carlo sample, looking for the low-energy photon, shows that the reconstruction efficiency of such photon conversion could as low as 1%, making impossible to further characterize this kind of events.

In Appendix A, a split sample cross checks are shown, to test the consistency of the selection.

We have tried to use a Breit-Wigner function convoluted with a Gaussian resolution
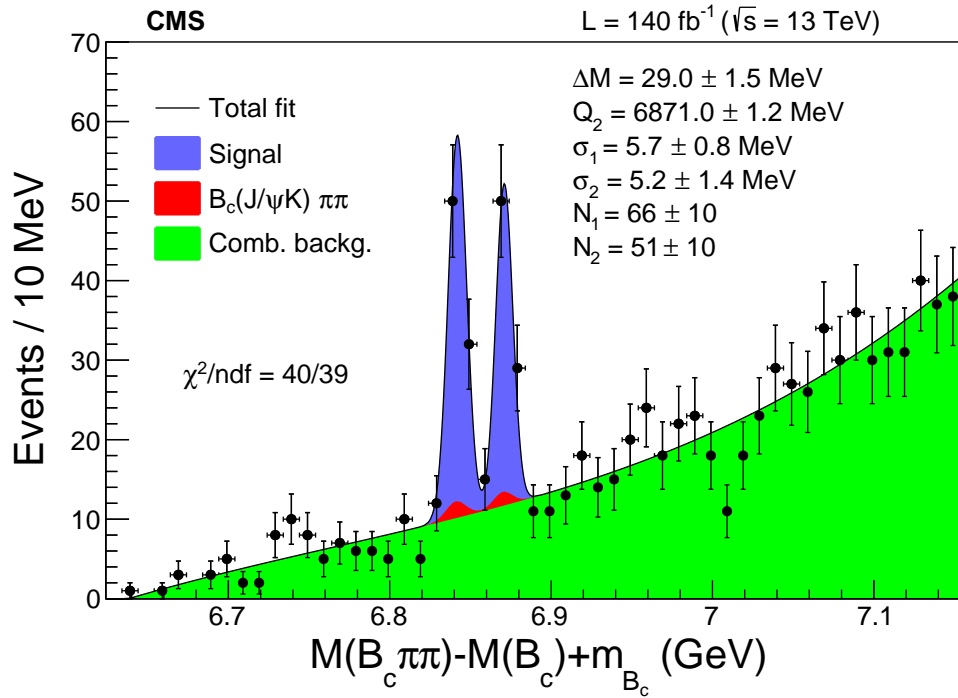
FIGURE 3.5: The invariant mass distribution (2016+2017+2018) with
the solid black line representing the total fit, the filled red area the
$B_c^+(J/\psi K^+)\pi^+\pi^-$ components, and the combinatorial background in
green. The vertical bars on the data points represent the statistical un-
certainties.

ΔM (MeV)	29.0 ± 1.5
m_2 (MeV)	6871.0 ± 1.2
σ_1 (MeV)	5.7 ± 0.8
σ_2 (MeV)	5.2 ± 1.4
N_1	66 ± 10
N_2	51 ± 10
N_{bkg}	801 ± 30
$a0$	1.19 ± 0.03
$a1$	0.22 ± 0.05
$a2$	0.08 ± 0.04

TABLE 3.5: Parameters fitted to the $B_c^+\pi\pi$ mass distribution for
2016+2017+2018 data sample.

function. The resolution was obtained from simulated samples. The fit is very unstable, then we opted to fix the masses to the ones returned by the nominal fit, as well as the background component. Both natural widths returned by the fit are consistent with zero, which may indicate that the natural width of any of the two peaks is small relative to the detector resolution. Figure 3.6 shows the Q distribution with the fit just described, and the result of the fit in the label.
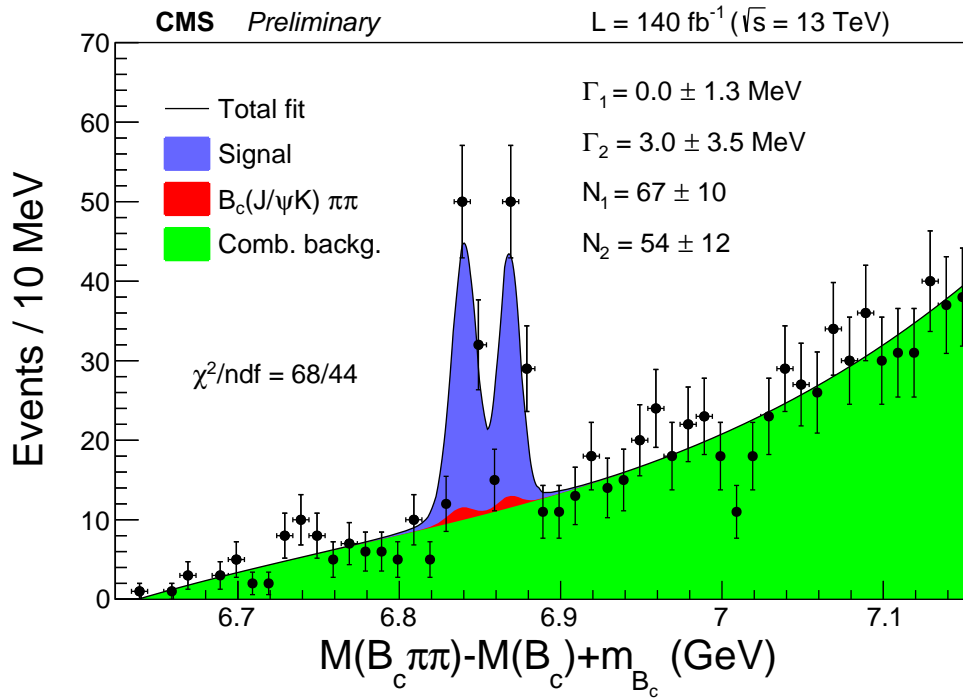
FIGURE 3.6: The invariant mass distribution (2016+2017+2018) with the solid black line representing the total fit, the filled red area the $B_c^+(J/\psi K^+)\pi^+\pi^-$ components. The vertical bars on the data points represent the statistical uncertainties.

Chapter 4

Search for exotic resonances in $\chi_b(1P)\pi^+\pi^-$ and $\Upsilon(1S)\pi^+\pi^-$ final states

A search for a bottomonium resonance-like structure in the $\chi_b(1P)\pi^+\pi^-$ and $\Upsilon(1S)\pi^+\pi^-$ invariant mass spectrums is performed using an integrated luminosity of 138.57 fb^{-1} of proton-proton collisions collected by the CMS experiment at $\sqrt{s} = 13$ TeV.

The analysis is focused on the decay channels, $X_b \to \chi_b(1P)\pi^+\pi^-$, $X_b \to \Upsilon(1S)\pi^+\pi^-$ following with the $\chi_{b1}(1P) \to \Upsilon(1S)\gamma$ and $\Upsilon(1S) \to \mu^+\mu^-$ decays. If a clear peak is found in one of the two spectra, beyond expected signals foreseen by conventional spectroscopy, the yield and its statistical significance would be estimated and the relative production cross sections would be measured with respect to some other reference signal. If no clear hint/evidence of a new signal was found, a limit setting procedure would be applied to provide upper bounds on the production of the X_b.

4.1 Data and simulated samples

This analysis is performed with the MuOnia primary dataset collected by CMS in proton-proton collisions at a center of mass energy of 13 TeV, during the 2016, 2017 and 2018 data taking periods. The corresponding integrated luminosity of the analysed dataset is about ~ 139 fb^{-1} for the whole three years. The list of data samples and respective run ranges is given in Table 4.1.

Only certified data has been used, the JSON files used to access the data on the GRID are:

1. Cert_271036-284044_13TeV_ReReco_07Aug2017_Collisions16_JSON_MuonPhys.txt

2. Cert_294927-306462_13TeV_EOY2017ReReco_Collisions17_JSON_MuonPhys.txt

3. Cert_314472-325175_13TeV_17SeptEarlyReReco2018ABC_PromptEraD_Collisions18
   _JSON_MuonPhys.txt

Data set	Run range
/MuOnia/Run2016B-17Jul2018 ver2-v1	273150–275376
/MuOnia/Run2016C-17Jul2018-v1	275657–276283
/MuOnia/Run2016D-17Jul2018-v1	276315–276811
/MuOnia/Run2016E-17Jul2018-v1	277420–277305
/MuOnia/Run2016F-17Jul2018-v1	277932–278808
/MuOnia/Run2016G-17Jul2018-v1	278820–280385
/MuOnia/Run2016H-17Jul2018-v1	281207–284068
/MuOnia/Run2017B-31Mar2018-v1	297046–299329
/MuOnia/Run2017C-31Mar2018-v1	299368–302029
/MuOnia/Run2017D-31Mar2018-v1	302030–303434
/MuOnia/Run2017E-31Mar2018-v1	303824–304797
/MuOnia/Run2017F-31Mar2018-v1	305040–306462
/MuOnia/Run2018A-17Sep2018-v1	315252–316995
/MuOnia/Run2018B-17Sep2018-v1	317080–319310
/MuOnia/Run2018C-17Sep2018-v1	319337–320065
/MuOnia/Run2018D-PromptReco-v2	320673–325175

TABLE 4.1: Data samples used in the current analysis.

Fully simulated Monte Carlo (MC) samples are used for the purpose of evaluating trigger effects, mass resolution and efficiencies. $\Upsilon(2S, 3S) \to \Upsilon(1S)\pi^+\pi^-$, $X_b \to \chi_b(1P)\pi^+\pi^-$ and $X_b \to \Upsilon(1S)\pi^+\pi^-$ decays used in this analysis have been produced initially privately and afterwards officially (centrally). Those private samples have been validated against the samples produced officially. They are fully consistent with each other even for the pile-up distribution.

The production configurations, global tags, and the setup for pile-up mixing, are from the official RunIISummer16, RunIIFall17 and RunIIAutumn18 campaigns for 2016, 2017 and 2018, respectively. A list of simulated MC samples can be found in 4.2.

The MC events are first generated with PYTHIA8 to produce proton-proton collisions, and to perform the parton shower and hadronization. Stable particles are decayed with the EVTGEN package [41] and final state radiation is implemented with PHOTOS [42].

Since there is no X_b particle in the generator, the signal samples are generated with a modification to the mass of the $\chi_{b0}(1P)$ state. In order to enhance the production speed, filters at generator level have been applied. An obvious requirement is to have, in an event, one X_b candidate decaying to an $\Upsilon(1S)$ or a $\chi_{b1}(1P)$ particles according to the (forced) decay of interest; for the latter particle the (forced) radiative decay is into $\Upsilon(1S)$. Other requirements include the existence of least two opposite-sign muons with pseudo-rapidity $|\eta| < 2.4$ and a minimum transverse momentum of 2.5 GeV and also

MC sample	Campaign	$M(X_b)$ [GeV]
chib0_ToUpsilon1SPiPi_m**X**_TuneCP5_13TeV	RunIISummer16 RunIIFall17 RunIIAutumn18	**X**=10p1,10p3, 10p5,10p7, 10p9,11p1, 11p4,11p7, 12p0
chib0_Tochib1PiPi_m**X**_TuneCP5_13TeV	RunIISummer16 RunIIFall17 RunIIAutumn18	**X**=10p3,10p5, 10p7,10p9, 11p1,11p4, 11p7,12p0,

TABLE 4.2: Official signal Monte Carlo samples produced with the three years campaigns: 2016, 2017 and 2018 for $X_b \to \Upsilon(1S)\pi^+\pi^-$ and $X_b \to \chi_b(1P)\pi^+\pi^-$ decays and different mass point.

a minimum transverse momentum of 0.5 GeV for generic tracks (pions). These criteria approximately reproduce the acceptance of the detector. Events are then passed through the CMS detector simulation using the GEANT4 package [43], including digitized signals from MC-simulated inelastic proton-proton events to match the amount of pileup in the data. Simulated events are processed with the same reconstruction and trigger algorithms as in data.

4.2 Triggers and event selection

This analysis highly depends on the reconstruction of $\Upsilon(1S) \to \mu^+\mu^-$ in order to select events containing a Υ meson and perform the search for the X_b state. Two dedicated inclusive HLT paths were set up and configured before the 2017 data taking and at the beginning of 2018 data taking. Specifically these two HLT paths together with the one used in 2016 data taking are reported below:

- HLT_Dimuon8_Upsilon_Barrel for the full 2016 data taking

  - $p_T(\mu^+\mu^-) > 7.9$ GeV
  - $m(\mu^+\mu^-) \in [8.5, 11.5]$ GeV
  - $|y(\mu^+\mu^-)| < 1.25$
  - $P_{vtx}(\mu^+\mu^-) > 0.5\%$ probability for the vertex fit of the two muons

- HLT_Dimuon12_Upsilon_eta1p5 for the full 2017 data taking

  - $p_T(\mu^+\mu^-) > 11.9$ GeV
  - $m(\mu^+\mu^-) \in [8.5, 11.5]$ GeV
  - $|\eta(\mu^+\mu^-)| < 1.5$

  – $P_{vtx}(\mu^+\mu^-) > 0.5\%$ probability for the vertex fit of the two muons

- HLT_Dimuon12_Upsilon_y1p4 started just after the beginning of 2018 data taking

  – $p_T(\mu^+\mu^-) > 11.9$ GeV

  – $m(\mu^+\mu^-) \in [8.5, 11.5]$ GeV

  – $|y(\mu^+\mu^-)| < 1.4$

  – $P_{vtx}(\mu^+\mu^-) > 0.5\%$ probability for the vertex fit of the two muons

The HLT paths had different L1 seeds:

- 2016, activated at lumi $< 1.0e34$ Hz/cm2:
  `DoubleMu_10_0_dEta_Max1p8 OR`

- 2016, activated at lumi $< 1.1e34$ Hz/cm2:
  `DoubleMu0er1p6_dEta_Max1p8_OS OR`

- 2016, always on:
  `DoubleMu0er1p4_dEta_Max1p8_OS OR`

- 2016, activated at lumi $< 1.2e34$ Hz/cm2:
  `DoubleMu_11_4 OR`

- 2016, always on:
  `DoubleMu_12_5`

- 2017–2018, (no p_T cut, $|\eta| < 1.5$, *high quality*, opposite-sign, deltaR(MuMu)< 1.4):
  `DoubleMu0er1p5_SQ_OS_dR_Max1p4 OR`

- 2017–2018, ($p_T > 4$, *high quality*, opposite-sign, deltaR(MuMu)< 1.2):
  `DoubleMu4_SQ_OS_dR_Max1p2`

Table 4.3 also presents the integrated luminosity of the samples, separately for each running year and HLT trigger period, both before and after applying the data certification requirement, as computed with the `brilcalc` tool [30]. The total integrated luminosity is also provided.

4.3   Event reconstruction

The $\Upsilon(1S)$ S-wave quarkonium state was reconstructed taking advantage of the standard muon reconstruction. The Muon-POG-approved "Soft Muon" selection is used. This consists of tracker or global muons that follow the requirements summarized in the following:

HLT path	L_{int} (fb^{-1})	
	Recorded	Certified
HLT_Dimuon8_Upsilon_Barrel_v2	2.313	2.221
HLT_Dimuon8_Upsilon_Barrel_v3	5.532	5.290
HLT_Dimuon8_Upsilon_Barrel_v4	9.650	9.247
HLT_Dimuon8_Upsilon_Barrel_v5	10.139	9.720
HLT_Dimuon8_Upsilon_Barrel_v6	9.118	8.773
HLT_Dimuon12_Upsilon_eta1p5_v8	3.146	3.012
HLT_Dimuon12_Upsilon_eta1p5_v9	2.084	1.930
HLT_Dimuon12_Upsilon_eta1p5_v10	1.516	1.367
HLT_Dimuon12_Upsilon_eta1p5_v11	9.133	8.453
HLT_Dimuon12_Upsilon_eta1p5_v12	27.823	26.464
HLT_Dimuon12_Upsilon_eta1p5_v13	0.901	0.862
HLT_Dimuon12_Upsilon_eta1p5_v13	5.581	5.413
HLT_Dimuon12_Upsilon_y1p4_v1	3.794	3.656
HLT_Dimuon12_Upsilon_y1p4_v2	54.327	52.163
Total luminosity		138.571

TABLE 4.3: Trigger paths used in this analysis and respective integrated luminosities.

- the muon track needs to qualify as "high-purity" and must includes more than 5 hits in the tracker layers, with at least one of them being in a pixel layer;

- the absolute values of the impact parameters $|dxy|$ and $|dz|$ of the muon tracks must be smaller than 0.3 cm and 20.0 cm, respectively;

- the muon must be characterized by $|\eta| < 2.4$ and by a minimum transverse momentum of 4.0 GeV;

- the muon must meet the (quality) reconstruction requirement "TMOneStation-Tight".

The opposite-sign combinations of these muons, the $(\mu^+\mu^-)$ candidates, must initially satisfy that:

- the invariant mass must belong to the mass window $8.6 < m(\mu^+\mu^-) < 11.4$ GeV;

- the vertex fit of the two muons with the geometrical constraint to come from a common vertex must be not only valid (converged) but also have a vertex probability $P_{\chi^2} (\mu\mu\text{-vtx}) > 1\%$;

- the p_T must be greater than 10 GeV.

Finally, the so called trigger matching is applied to both muons of the selected pairs: the muons of the selected combination must be exactly those muons that have been used

at trigger level to build the dimuon candidate that has triggered the event.

The final selected $\mu^+\mu^-$ candidate, one per event, is retained if its invariant mass is in the range [9.1, 10.5] GeV. This window allows to collect the three signals Υ(nS) with n = 1, 2, 3.

In order to make results homegeneous, regardless the year of data taking and the HLT trigger, it is mandatory to require the same η range for single muons and the same transverse momentum of the dimuon candidates: $|\eta(\mu\pm)| < 1.5$ and $p_T(\mu^+\mu) > 12$ GeV. After the application of these two requirements Figure 4.1 shows the dimuon mass spectrum for the dimuon candidates divided by year of data taking, whereas Figure 4.2 shows the same three invariant mass distributions being superimposed after relative normalization.
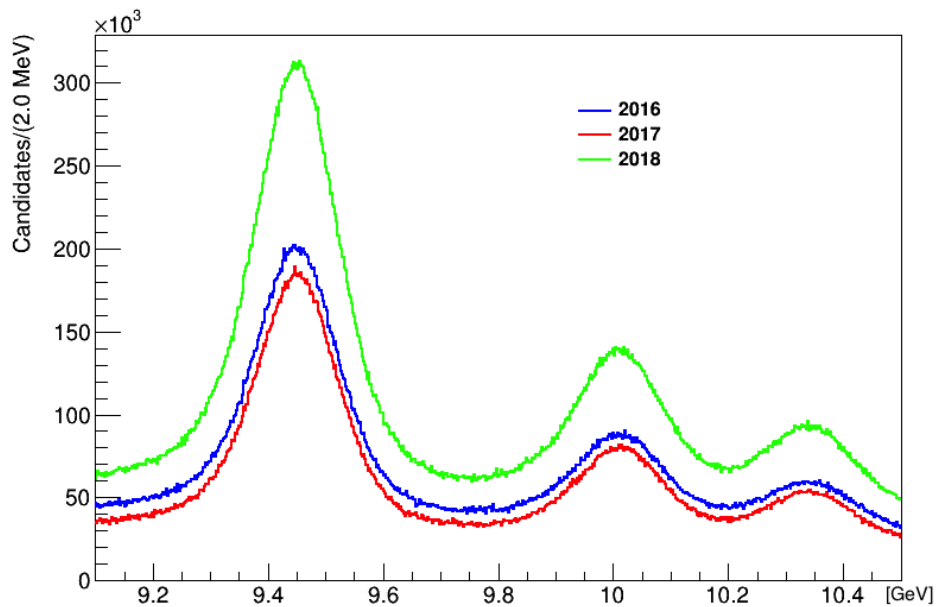
FIGURE 4.1: Dimuon mass distributions, for the 3 years of the Run-II data taking.

For each Υ candidate, its combinations with any two additional, oppositely charged, tracks are investigated; all tracks, other than muons, are assumed to be pions and must have $p_T > 0.5$ GeV (to reproduce track acceptance). These pion candidates are required to pass standard high-quality and purity track requirements, to have at least 1 pixel hits, at least 5 tracker hits. Any considered dipion must have an invariant mass less than 1.6 GeV.

FIGURE 4.2: Dimuon mass distributions, for the 3 years of the Run-II data
taking, superimposed after relative normalization.

A vertex fitting procedure, based on the standard package KinematicConstraintVertexFitter, has been applied to the $\Upsilon\pi^+\pi^-$ candidate using the daughter muons. The $\Upsilon(1S)$ mass constraint is applied in order to considerably improve the resolution in the $\mu^+\mu^-\pi^+\pi^-$ mass reconstruction. The final $\Upsilon\pi^+\pi^-$ candidates are kept if their invariant masses are in the range [9.8,12.2] GeV. The $\Upsilon\pi^+\pi^-$ invariant mass distribution resulting from this pre-selection is shown in Figure 4.3.

Table 4.4 summarizes the offline selections for muon pairs ($\Upsilon(1S)$), pion pairs and the 4-track candidates ($\Upsilon(1S)\pi^+\pi^-$).

Given the extreme width of the investigated spectrum, where the hypothetical X_b could be found, it is rather difficult to configure a non cut-based selection (like a BDT or similar), also because of the high level of multiplicity still present at this stage and shown in Figure 4.5. Unlike from the Run-I CMS analysis, the level of the combinatorial background is very high in Run-II data because of the strongly increased pileup conditions.

As can be seen in Figure 4.6, the WS distribution reproduces rather well the background shape of the RS distribution and well confirms the quite pure combinatorial nature of the distribution once $\Upsilon(2S)$ and $\Upsilon(3S)$ signal peaks are removed.
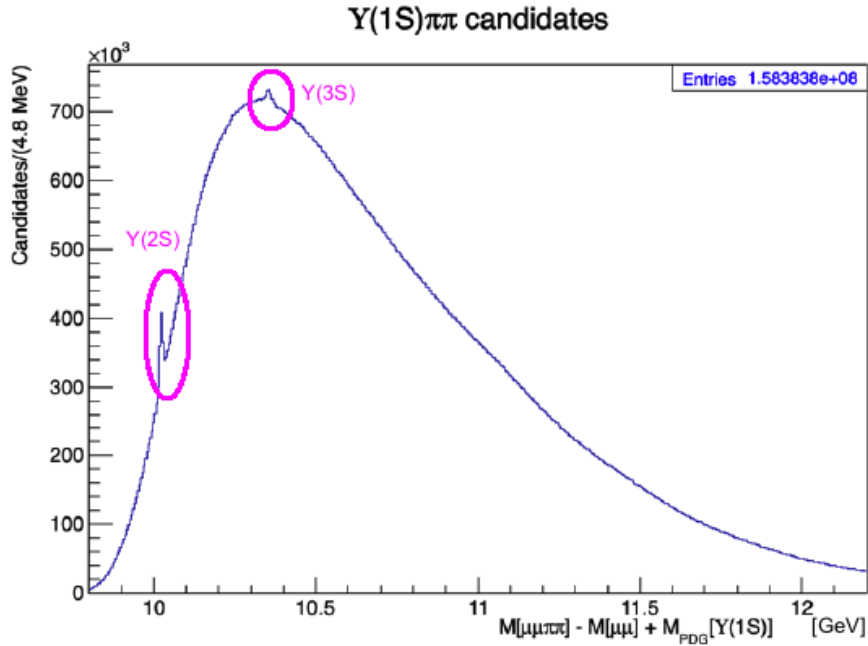
FIGURE 4.3: The invariant mass distribution of $\Upsilon(1S)\pi^+\pi^-$ candidates after baseline selection.

Source	Selections
innerTrack	numberOfValidStripHits ≥ 5
	numberOfValidPixelHits ≥ 1
	$p_T(\pi^\pm) > 0.5 GeV$
	$\lvert\eta(\pi^\pm)\rvert < 2.5$
Track pair	Opposite charge sign
	pion $p_T > 0.5 GeV$
	$M(\pi^+\pi^-) < 1.6 GeV$
$\mu^+\mu^-$ pair	$9.3 GeV < M_{\mu^+\mu^-} < 9.6 GeV$
	$\lvert\eta(\mu^\pm)\rvert < 1.5$
	$p_T(\mu^+\mu^-) > 12 GeV$
$\mu^+\mu^-\pi^+\pi^-$	Constrained fit probability $> 5\%$
	$9.8\ GeV < M_{\Upsilon(1S)\mu^+\mu^-} < 12.2\ GeV$

FIGURE 4.4: Dimuon mass distributions, for the 3 years of the Run-II data taking, superimposed after relative normalization.

FIGURE 4.5: Multiplicity of $X_b \rightarrow \Upsilon(1S)\pi^+\pi^-$ candidates. The last bin is actually the overflow bin.
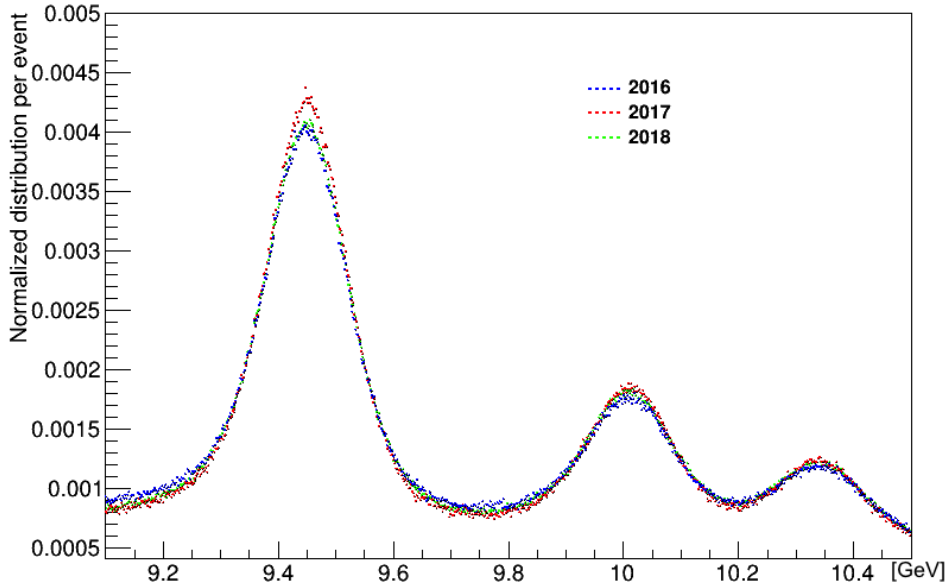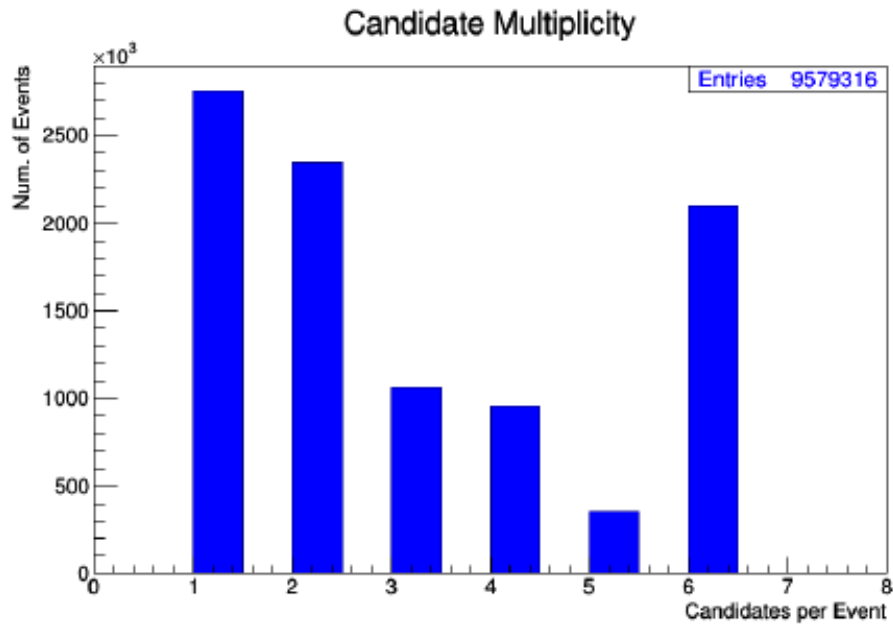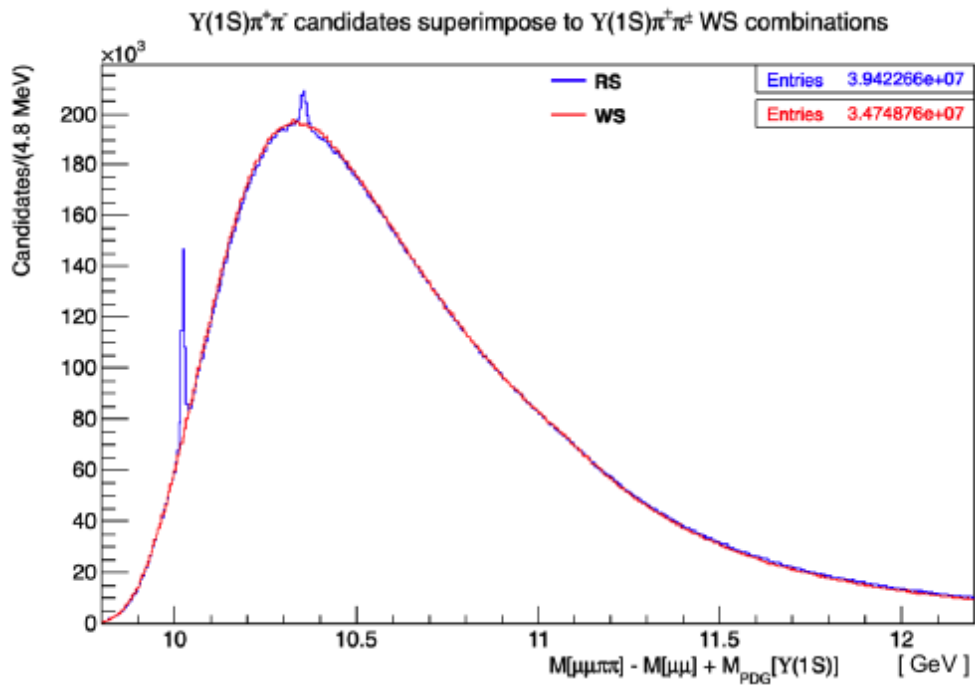

FIGURE 4.6: Dimuon mass distributions, for the 3 years of the Run-II data taking, superimposed after relative normalization.

4.4   Selection of $\chi_b(1P)\pi^+\pi^-$ candidates

Starting from the sample of collected $\Upsilon(1S)$, the candidate $\chi_b(1P)$ is reconstructed by combining the selected $\Upsilon(1S)$ with a converted photon ($\gamma \to e^+e^-$). Afterwords the candidate $\chi_b(1P)\pi^+\pi^-$ is reconstructed by combining a $\chi_b(1P)$ candidate with two tracks. The details about the reconstruction of the converted photons are discussed in the next subsection.

4.4.1   Photon reconstruction

Photon conversions are characterized by an electron-positron pair originating from the photon conversion vertex. Because of the energy spectrum of the photon from the radiative decay, the electron and positron tracks are low p_T tracks.

To efficiently reconstruct low p_T and displaced tracks as those coming from a typical photon conversion, the algorithm relies on the capabilities and features of the iterative tracking. For this analysis, only standard high purity conversions are used.

4.4.2 $\chi_b(1P)$ reconstruction

For each event the selected $\Upsilon(1S)$ candidate and the converted photons are paired to form $\chi_b(1P)$ candidates. The distance in the direction parallel to the z axis between the dimuon vertex and the extrapolation of the photon direction to the beam-line (dz), is required to be less than $5\ mm$.

Photon conversions can be reconstructed if they mainly happen in the one-two innermost pixel layers as can be noticed in Figure 4.7 that shows the distribution along the radial dimension of the photon conversion vertices, for the three data taking periods. The change in the number of pixel layers occurred between 2016 and 2017 can be clearly observed. The observed patterns reflect the tracker material distribution convoluted with the reconstruction efficiency.

Figures 4.8 and 4.9 refer to the $\mu^+\mu^-$ invariant mass distributions, after the preselection criteria have been applied to dimuon candidates that furthermore are combined to converted photons to form one or more $\chi_b(1P)$ candidates in an event.

4.4.3 $\chi_b(1P)\pi^+\pi^-$ reconstruction and selection

The combination of a $\chi_b(1P)$ candidate with two oppositely charged pions follow the same baseline criteria discussed before to build up $\Upsilon(1S)\pi^+\pi^-$ candidates. A $\mu^+\mu^-\gamma\pi^+\pi^-$ vertex fit with a geometric constraint together with a $\chi_b(1P)$ mass constraint is performed by exploiting the so called KinematicConstraintVertexFitter algorithm available in a standard CMSSW vertexing package. The final candidate is retained if its invariant mass is in the range [10.2, 12.2] GeV.
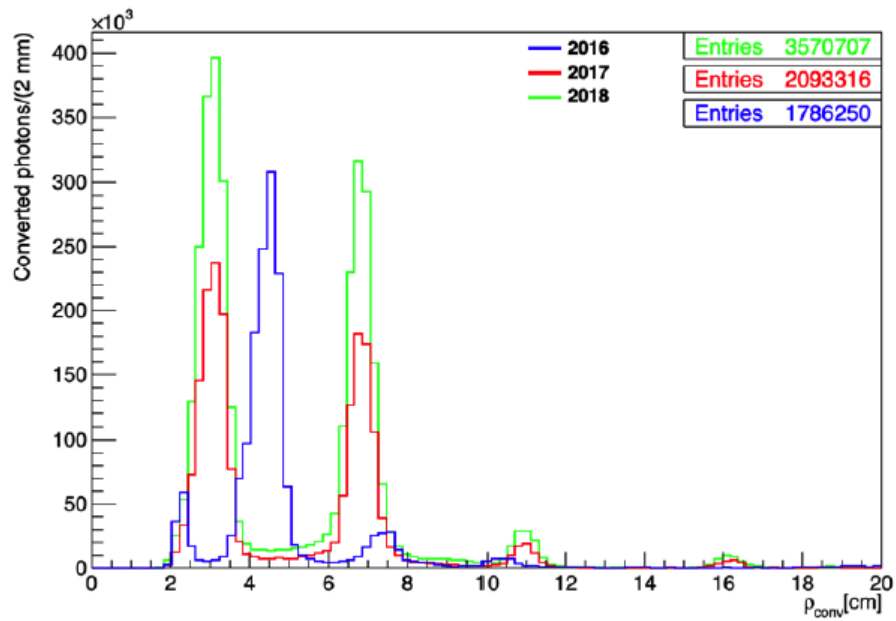
FIGURE 4.7: Distribution of the radial coordinate of the photon conversion vertices (without applying requirements on the dimuon candidate) for 2016(blue), 2017(red) and 2018(green) data taking periods in the LHC Run-II.
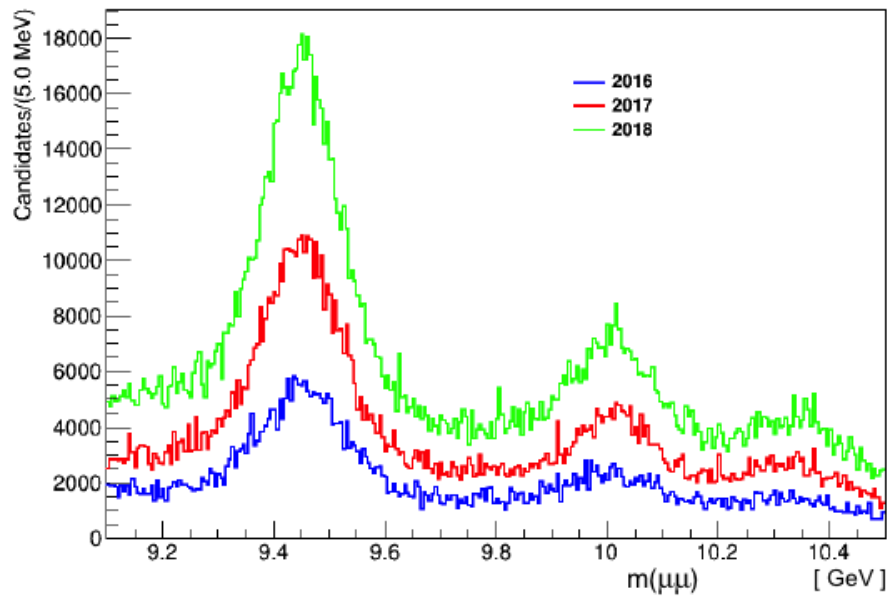
FIGURE 4.8: Dimuon mass distributions, after passing trigger matching and $|\eta(\mu\pm)| < 1.5$ and $p_T(\mu^+\mu^-) > 12$ GeV requirements, for the 3 years of the Run-II data taking, when dimuon candidates are used to reconstruct $\chi_b(1P)$ candidates.
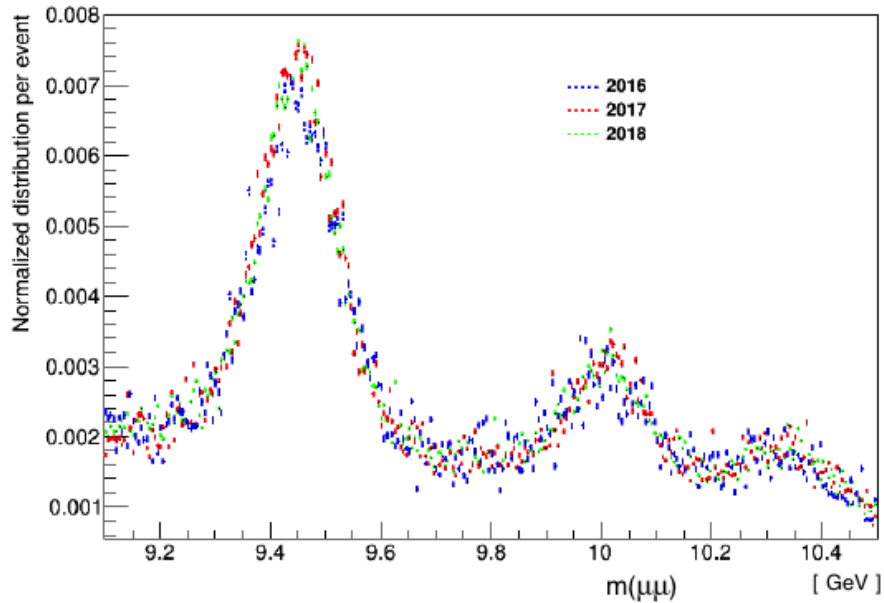
FIGURE 4.9: The three mass distributions shown in Figure 4.8 are presented superimposed after proper relative normalization.

The $\chi_b(1P)\pi^+\pi^-$ invariant mass resulting from this selection is shown in Figure 4.10 with all multiplicity. Moreover the final vertex fit probability is again required to be greater than 5% in order to reject random combinations. After applying the vertex probability most of the combinatorial background in the dimuon mass spectrum is eliminated. Furthermore only $\Upsilon(1S)$ candidates which are in the [9.3, 9.6] GeV mass window are used to reconstruct $\chi_b(1P)$ candidates. Table 4.11 summarizes the baseline selection criteria.

An unexpected small excess appears around 10.5 GeV in Figure 4.10. Later, after applying, the selection of the best candidate in the event, this excess will be much weaker or vanishing after background subtraction. It can be associated to the radiative decay $\chi_{b1}(3P) \rightarrow \Upsilon(2S)\gamma$ (see Ref.[44]) with the subsequent decay $\Upsilon(2S) \rightarrow \Upsilon(1S)\pi\pi$. The excess seems to be peaking at a slightly lower mass value than the $\chi_{b1}(3P)$ mass but this shift can be, at least partially, compensated by the missing photon energy scale correction that has been extensively studied in the CMS paper in Ref.[45].

A way to study the background nature and shape is to compare the mass distribution $\chi_b(1P)\pi^+\pi^-$ obtained so far (the right-sign) with the mass distribution of the wrong-sign combinations, namely the mass distribution $\chi_b(1P)\pi^\pm\pi^\pm$. The latter is superimposed to the former, after proper normalization, in Figure 4.12.
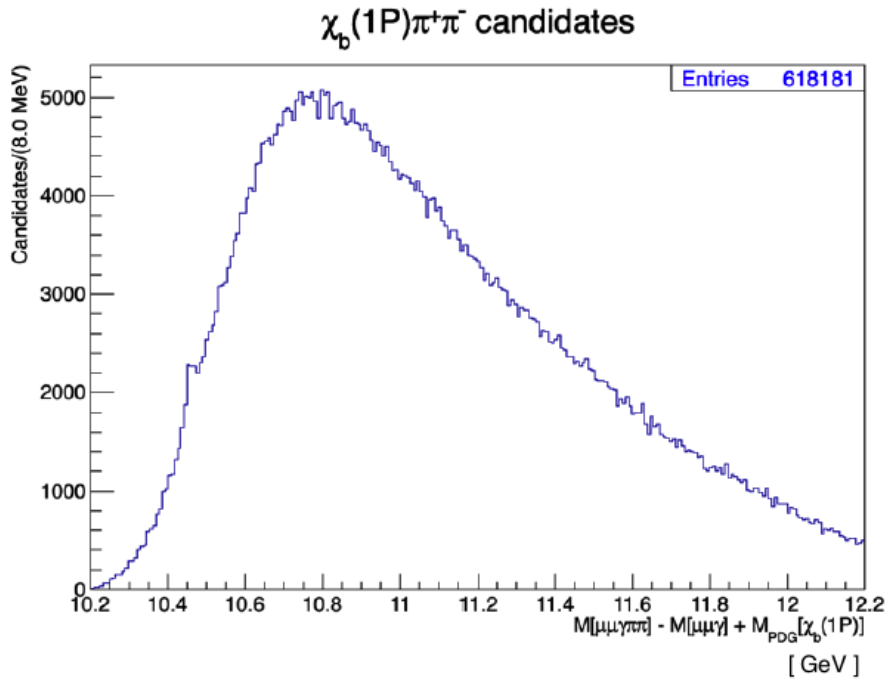
FIGURE 4.10: The invariant mass distribution of $\chi_b(1P)\pi^+\pi^-$ candidates after baseline selection.

Source	Selections
innerTrack	numberOfValidStripHits ≥ 5 numberOfValidPixelHits ≥ 1 $p_T(\pi^\pm) > 0.5\ GeV$ $\|\eta(\pi^\pm)\| < 2.5$
Track pair	Opposite charge sign $p_T(Leading\ \pi) > 0.7\ GeV$ $p_T(Softer\ \pi) > 0.5\ GeV$ $M(\pi^+\pi^-) < 1.6\ GeV$
$\mu^+\mu^-$ pair	$9.3\ GeV < M_{\mu^+\mu^-} < 9.6\ GeV$ $\|\eta(\mu^\pm)\| < 1.5$ $p_T(\mu^+\mu^-) > 12\ GeV$
$\chi_b(1P)$	$9.87\ GeV < M_{\mu^+\mu^-\gamma} < 9.902\ GeV$
$\mu^+\mu^-\gamma\pi^+\pi^-$	Constrained fit probability $> 5\%$ $Energy(\gamma) > 400\ MeV$

FIGURE 4.11: Selection criteria for pions, $\pi^+\pi^-$ pairs, $\mu^+\mu^-$ pairs, $\chi_b(1P)$ and $\chi_b(1P)\pi^+\pi^-$ candidates.
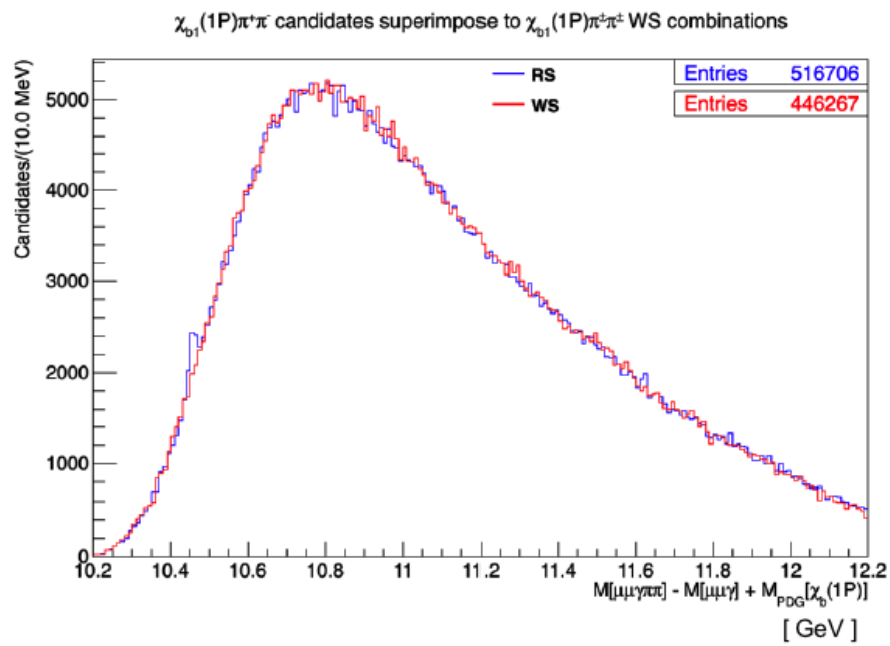
FIGURE 4.12: RS mass distribution (blue) compared to the superimposed WS mass distribution (red). The WS distribution is normalized to RS distribution.

Chapter 5

Estimation of an upper limit on the production of X_b decaying into $\Upsilon(1S)\pi^+\pi^-$ and $\chi_b(1P)\pi^+\pi^-$ final states

After reconstructing and selecting $\Upsilon(1S)\pi^+\pi^-$ and $\chi_b(1P)\pi^+\pi^-$ final states no significant excess above the background was observed. Thus, after having no relevant hint of a possible signal that can be associated to the hypothetical X_b state, we proceed in performing the upper bound calculation on the X_b production cross-section times the unknown branching ratio of its decay to the considered final state. In order to minimize as much as possible the effect of the systematic uncertainties we actually calculate ratios of production cross sections choosing a suitable decay as a reference channel:

- The upper limit on the production of the X_b times the unknown branching ratio of its decay into $\Upsilon(1S)\pi^+\pi^-$ is performed with respect to the normalization channel $\Upsilon(2S) \to \Upsilon(1S)\pi^+\pi^-$; the reference signal is present in the same final state used for the search.

- The upper limit on the production of the X_b times the unknown branching ratio of its decay into $\chi_b(1P)\pi^+\pi^-$ is performed with respect to the normalization channel $\chi_{b1}(1P) \to \Upsilon(1S)\gamma$, since, in this case, no reference signal is available in the final state used for the search.

The calculation of p-values and the upper limits settings are carried out with the so called combine which is a RooFit/RooStats-based software tool used for statistical analysis. The combine provides an interface to many different statistical techniques available inside the RooFit/RooStats package used widely inside CMS and, more in general, within HEP community. For the purpose of the analysis, the modified frequentist Asymptotic CLs method is used in the calculation of the upper bounds and the profile

48

Chapter 5. Estimation of an upper limit on the production of X_b decaying into
$\Upsilon(1S)\pi^+\pi^-$ and $\chi_b(1P)\pi^+\pi^-$ final states

likelihood method is used for obtaining the p-values at each mass points. The latter is also an asymptotic method that makes use of a profile likelihood ratio to calculate the local p-value of the background only hypothesis.

5.1 Upper limit for production of the X_b decaying to $\Upsilon(1S)\pi^+\pi^-$

The calculation of the upper bound for the production of $X_b \to \Upsilon(1S)\pi^+\pi^-$ has been performed with respect to the production of $\Upsilon(2S) \to \Upsilon(1S)\pi^+\pi^-$. Specifically the upper limit has been provided for the following rate:

$$R = \frac{\sigma(pp \to X_b \to \Upsilon(1S)\pi^+\pi^-)}{\sigma(pp \to \Upsilon(2S) \to \Upsilon(1S)\pi^+\pi^-)} = \frac{\sigma(pp \to X_b + X) \times B(X_b \to \Upsilon(1S)\pi^+\pi^-)}{\sigma(pp \to \Upsilon(2S) + X) \times B(\Upsilon(2S) \to \Upsilon(1S)\pi^+\pi^-)} \tag{5.1}$$

that represents the inclusive production cross section in pp collisions of the hypothetical X_b state times its unknown branching fraction for its decay to $\Upsilon(1S)\pi^+\pi^-$ final state, divided by the production cross section of the $\Upsilon(2S)$ times the known branching fraction for the $\Upsilon(2S) \to \Upsilon(1S)\pi^+\pi^-$ decay.

Experimentally this ratio can be determined as the product of the ratio of the yields of X_b and $\Upsilon(2S)$ both decaying to the $\Upsilon(1S)\pi^+\pi^-$ final state multiplied by the inverse ratio of the corresponding reconstruction efficiencies (namely the inverse of the relative efficiency ϵ_{rel}):

$$R = \frac{N_{X_b}}{N_{\Upsilon(2S)}} \times \frac{\epsilon_{\Upsilon(2S)}}{\epsilon_{X_b}} \tag{5.2}$$

where:

- N_{X_b} is the $X_b \to \Upsilon(1S)\pi^+\pi^-$ yield,

- $N_{\Upsilon(2S)}$ is the $\Upsilon(2S) \to \Upsilon(1S)\pi^+\pi^-$ yield,

- $\epsilon_{\Upsilon(2S)}$ is the reconstruction efficiency of $\Upsilon(2S) \to \Upsilon(1S)\pi^+\pi^-$ signal,

- ϵ_{X_b} is the reconstruction efficiency of $X_b \to \Upsilon(1S)\pi^+\pi^-$ signal.

5.1.1 Reconstruction efficiency estimation

Monte Carlo (MC) samples for $X_b \to \Upsilon(1S)\pi^+\pi^-$ and $\Upsilon(2S) \to \Upsilon(1S)\pi^+\pi^-$ have been used to estimate the total reconstruction efficiency for each decay channel. To correctly estimate the efficiency, the reconstructed candidates (tracks, including muons) need to be matched to the generated particles in order to remove the purely combinatorial background and the possible reconstruction multiplicity mostly induced by pileup events.

The matching criteria is tuned checking that all the reconstructed candidates populating the sidebands of the reference signals such as $\Upsilon(2S, 3S) \to \Upsilon(1S)\pi^+\pi^-$ are completely removed.

The total efficiency is defined as the ratio between the number of reconstructed candidates at the end of the whole selection chain and the number of generated candidates in the sample.

$M[X_b]$	2016 MC samples		2017 MC samples		2018 MC samples	
	ϵ_{X_b}	ϵ_{rel}	ϵ_{X_b}	ϵ_{rel}	ϵ_{X_b}	ϵ_{rel}
10.1	0.277	1.092	0.260	1.024	0.285	1.123
10.3	0.235	0.926	0.232	0.914	0.244	0.960
10.5	0.211	0.830	0.203	0.801	0.223	0.879
10.7	0.185	0.728	0.177	0.696	0.204	0.804
10.9	0.166	0.655	0.162	0.638	0.171	0.675
11.1	0.147	0.579	0.138	0.544	0.163	0.642
11.5	0.090	0.354	0.094	0.369	0.109	0.428
12.0	0.049	0.192	0.063	0.247	0.058	0.229

FIGURE 5.1: Summary table for the efficiency calculations of $X_b \to \Upsilon(1S)\pi^+\pi^-$ for 2016, 2017 and 2018 MC samples, as a function of the mass. The efficiency ratio (as defined in the text) is also provided for the three years.

Table 5.1 reports the reconstruction efficiency estimated for the $X_b \to \Upsilon(1S)\pi^+\pi^-$ decay and different X_b mass values used at generation level, also considering different conditions corresponding to the three different years of data taking. These values are reported in the plot shown in Figure 5.2 together with the reconstruction efficiency ratio estimated from MC for $\Upsilon(2S, 3S) \to \Upsilon(1S)\pi^+\pi^-$. It can be appreciated how the last two efficiencies follow quite well the trend for the efficiency of the X_b as a function of the generated (nominal) mass, even if they show a slightly larger discrepancy across the years.

Mass Resolution estimation for signal modelling

Another ingredient needed in the upper bound extraction for the rate R is the parametrization of the signal and background PDFs. Let us start from the signal model that requires the prior knowledge of the mass resolution as a function of the mass itself. The procedure for the determination of the mass resolution consists in generating a set of signal
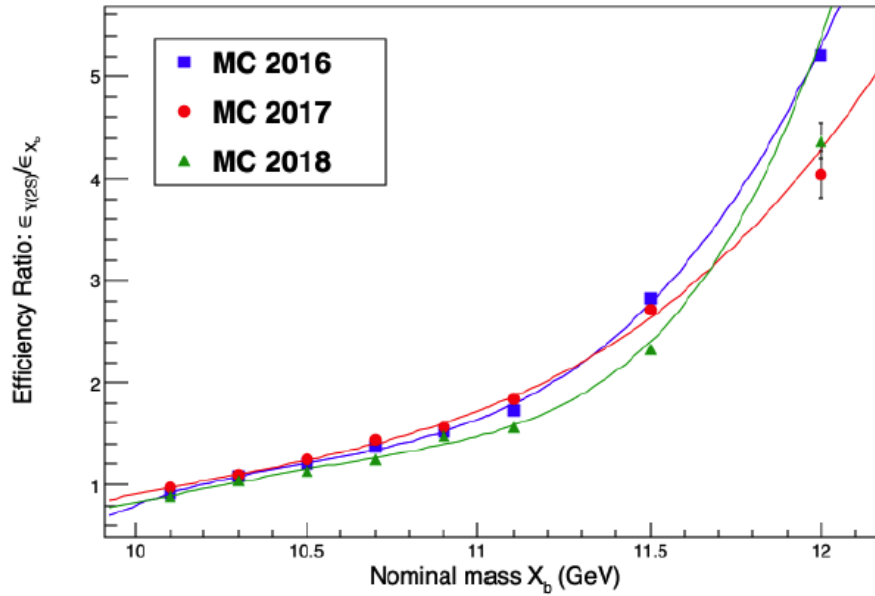
50

Chapter 5. Estimation of an upper limit on the production of X_b decaying into $\Upsilon(1S)\pi^+\pi^-$ and $\chi_b(1P)\pi^+\pi^-$ final states

FIGURE 5.2: Fits on the efficiency ratios, ϵ_{ratio}, obtained for 2016, 2017 and 2018 MC samples.

MC samples, one for each of the three years of data taking, with the generated X_b candidates' width set to zero. In this case the width of the signal associated to the reconstructed X_b candidates in the mass spectrum of interest, would represent the estimate of the experimental mass resolution.

Since the $\Upsilon(2S)$ natural width is negligible with respect to the experimental dimuon mass resolution, the same procedure has been adopted to measure the mass resolution for the decay $\Upsilon(2S) \to \Upsilon(1S)\pi^+\pi^-$. The mass resolution is calculated as the weighted average of the two gaussians' standard deviations.

M[X_b][GeV]	2016 MC samples	2017 MC samples	2018 MC samples
	σ_{X_b}[MeV]	σ_{X_b}[MeV]	σ_{X_b}[MeV]
10.1	6.49	6.06	6.21
10.3	8.68	8.09	8.19
10.5	10.57	10.60	10.76
10.7	13.71	12.20	12.23
10.9	15.74	13.53	14.87
11.1	17.54	15.49	16.66

Table 6.2: Summary table of the mass resolution values characterizing the decay $X_b \to \Upsilon(1S)\pi^+\pi^-$ and estimated by exploiting the 2016, 2017 and 2018 MC samples.

FIGURE 5.3: Summary table of the mass resolution values characterizing the decay $X_b \to \Upsilon(1S)\pi^+\pi^-$ and estimated by exploiting the 2016, 2017 and 2018 MC samples.
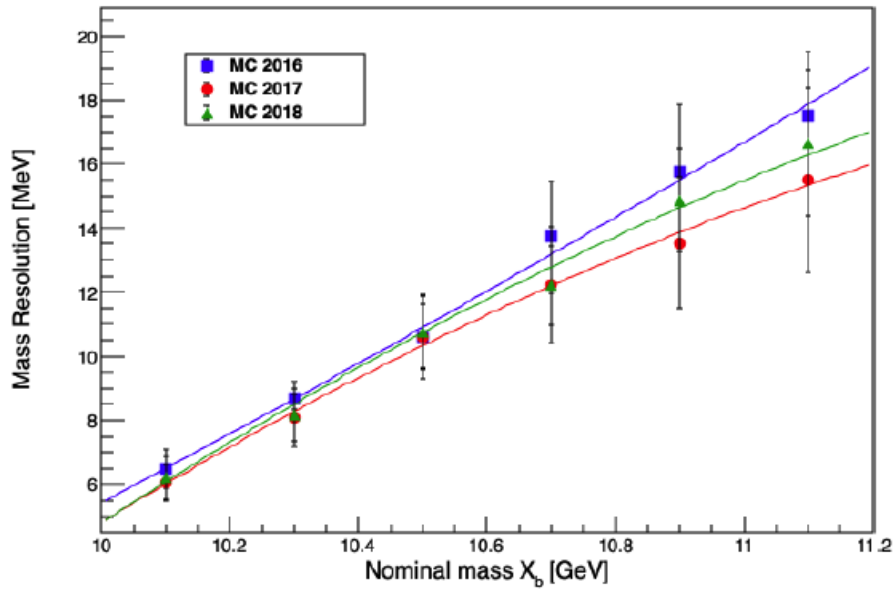
FIGURE 5.4: Superimposed fits to the estimated mass resolutions (points), obtained for 2016, 2017 and 2018 MC samples.

5.1.2 Background modelling

The background model has been extracted from data by fitting the full $\Upsilon(1S)\pi^+\pi^-$ mass spectrum. Since the spectrum is very wide it has been divided in five parts, of which the first two include also the $\Upsilon(2S)$ and $\Upsilon(3S)$ signal peaks.

The PDFs chosen for the background consist in Bernstein polynomial functions ranging from 4 to 6 degrees of freedom according to the fitted part of the spectrum. In the two lower mass parts that include the $\Upsilon(2S)$ and $\Upsilon(3S)$ signal peaks, a signal PDF has been considered in addition to the polynomial background to fit the two peaks. Specifically, in the first part of the spectrum a Voigtian (the convolution of a Breit-Wigner and a Gaussian) and a Crystal Ball functions, sharing the same mean, have been used for the $\Upsilon(2S)$ peak in the region [10.0, 10.05] GeV. The resulting fit is presented in Figure 5.5.

In the second part, instead, a Crystal Ball function has been used for the $\Upsilon(3S)$ peak in the region [10.31, 10.39] GeV. The resulting fit is presented in Figure 5.6.

The third, fourth and fifth part of the spectrum have been fitted with a background-only model, using, as in the first two parts, Bernstein polynomials. The resulting fits are presented in Figures 5.7, 5.8 and 5.9. The overlap between the 5 mass regions has been considered on purpose to allow smooth transitions when determining the upper limit for the rate R. During the latter procedure, two narrow enough mass bands containing the $\Upsilon(2S)$ and $\Upsilon(3S)$ peaks will be - of course - excluded.

52

Chapter 5. Estimation of an upper limit on the production of X_b decaying into
$\Upsilon(1S)\pi^+\pi^-$ and $\chi_b(1P)\pi^+\pi^-$ final states

FIGURE 5.5: Background shape determination by fitting with Bernstein polynomials the first part of the $\Upsilon(1S)\pi^+\pi^-$ mass spectrum in the data and considering a signal PDF, discussed in the text, to account for the $\Upsilon(2S)$ peak. Bin-by-bin pulls provide the goodness-of-fit.

FIGURE 5.6: Background shape determination by fitting with Bernstein polynomials the second part of the $\Upsilon(1S)\pi^+\pi^-$ mass spectrum in the data and considering a signal PDF, discussed in the text, to account for the $\Upsilon(3S)$ peak. Bin-by-bin pulls provide the goodness-of-fit.

FIGURE 5.7: Background shape determination by fitting with Bernstein polynomials the third part of the $\Upsilon(1S)\pi^+\pi^-$ mass spectrum in the data. Bin-by-bin pulls provide the goodness-of-fit.

FIGURE 5.8: Background shape determination by fitting with Bernstein polynomials the fourth part of the $\Upsilon(1S)\pi^+\pi^-$ mass spectrum in the data. Bin-by-bin pulls provide the goodness-of-fit.
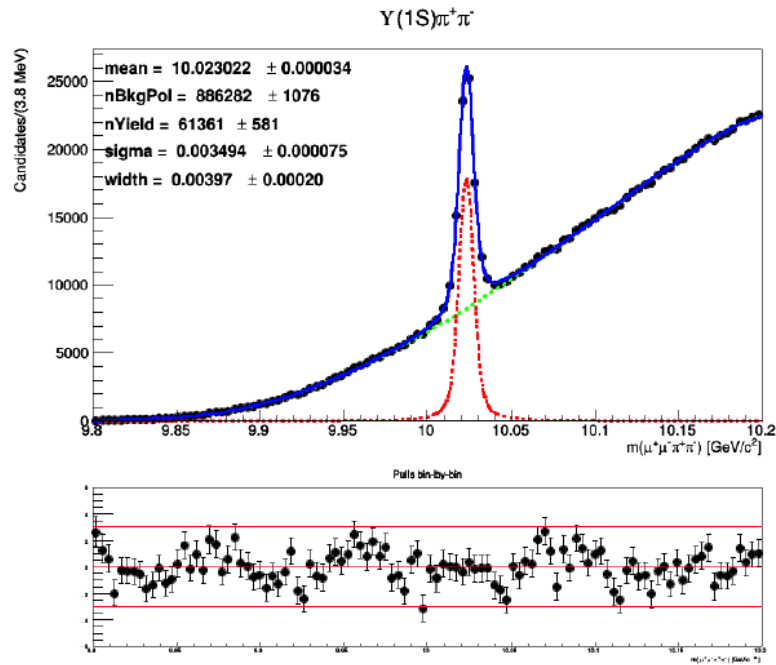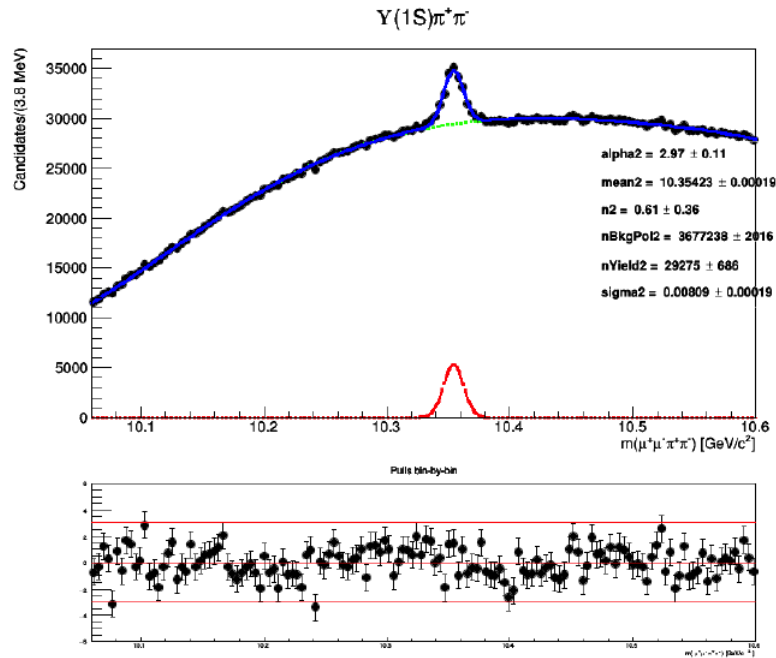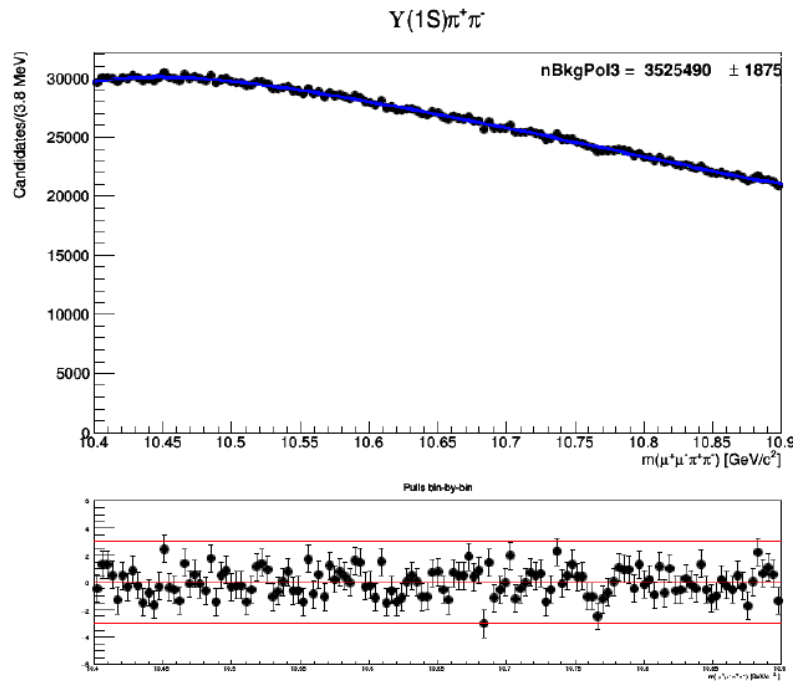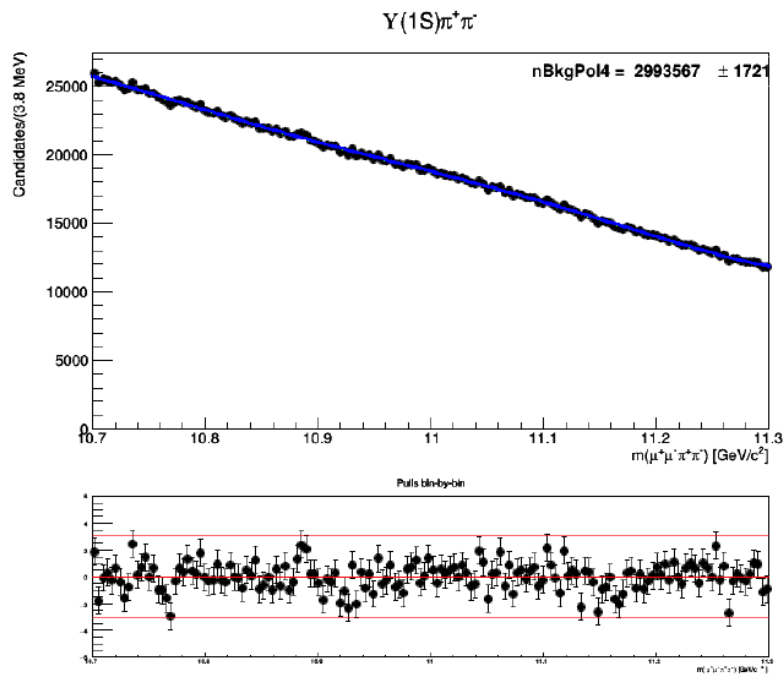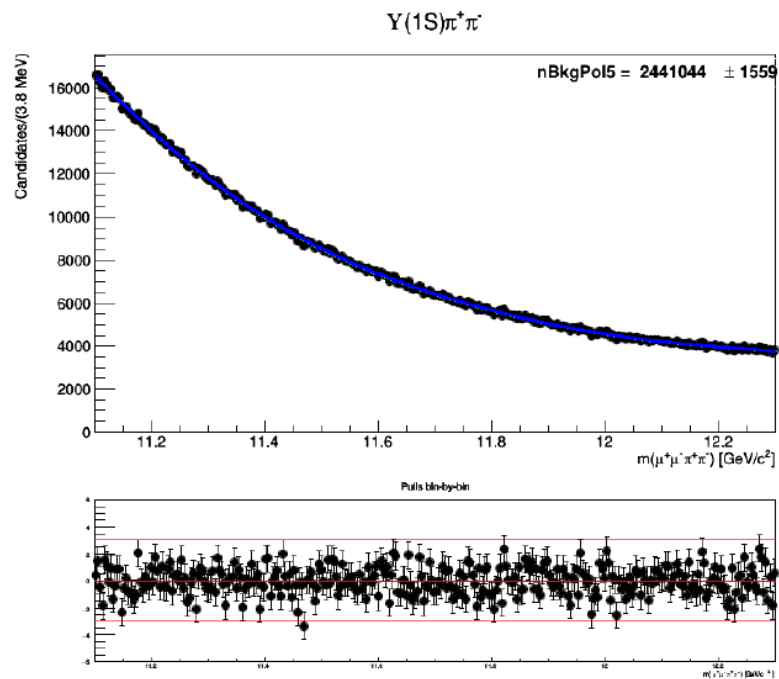
FIGURE 5.9: Background shape determination by fitting with Bernstein polynomials the fifth part of the $\Upsilon(1S)\pi^+\pi^-$ mass spectrum in the data. Bin-by-bin pulls provide the goodness-of-fit.

5.1.3 *p*-value calculation and upper limit estimation

Now it is possible to proceed with the *p*-value calculation and the upper limit estimation for the rate R given by (Eq. 5.2). The local *p*-values are calculated, as a function of the X_b mass, by using a profile likelihood ratio as test statistics and an asymptotic approach, as already mentioned at the beginning of this chapter. The expected and observed 95% confidence level upper limits on R are derived, as a function of the X_b mass, by using a modified frequentist approach (asymptotic CLs method), as already mentioned in the introduction of this chapter as well.

Both *p*-value and upper limit on R are provided in the mass range [10.08, 12.2] GeV and excluding both the lowest mass region with the $\Upsilon(2S)$ signal and the $\Upsilon(3S)$ signal mass region defined as [10.31, 10.39] GeV. As background models (one for each region) it has been used the ones extracted in the last subsection , whereas as a signal it is used a simple gaussian with its standard deviation strictly related to the mass resolution as previously discussed.

The local *p*-value is presented in Figure 5.10, whereas the upper limits on R are presented in Figure 5.11. The smallest local *p*-value is 0.004 at 10.3 GeV, corresponding to a statistical significance of 2.5σ which would be certainly reduced below 1 when taking into account the look-elsewhere effect. The observed upper limits on R are in the range $0.35 - 2.5\%$ at 95% CL depending on the X_b assumed mass. No systematic uncertainties are included when quoting this range of values.
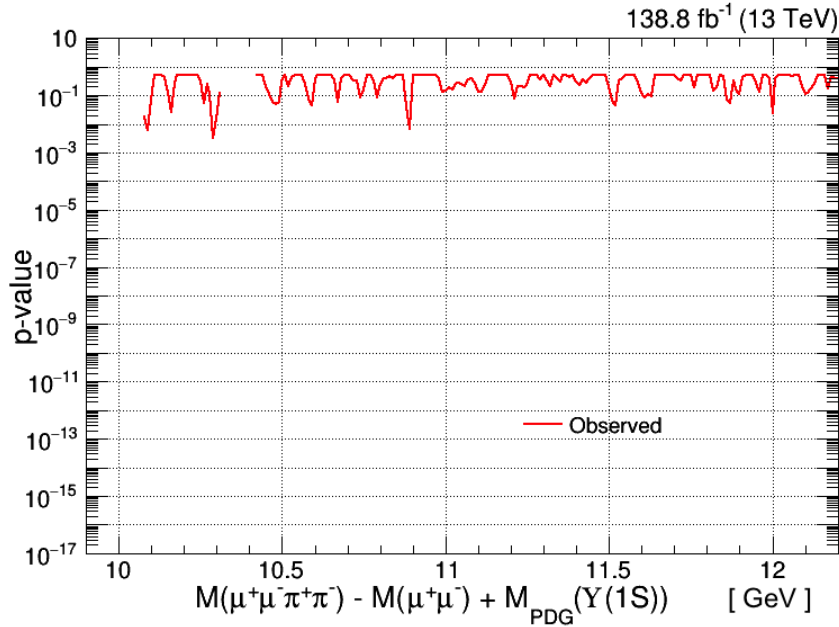

FIGURE 5.10: Observed local *p*-value for $X_b \to \Upsilon(1S)\pi^+\pi^-$ as a function of the assumed X_b mass. No systematic uncertainty is included.
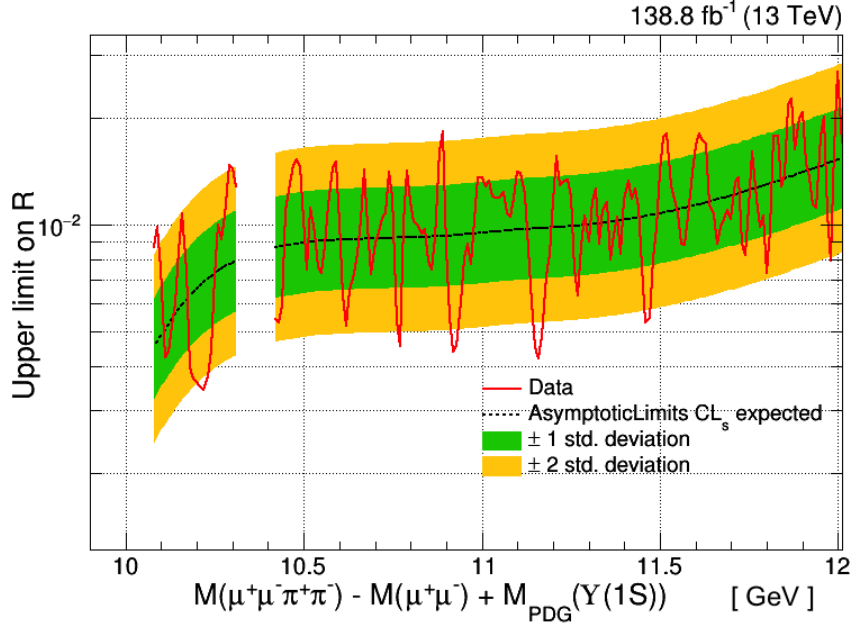
FIGURE 5.11: Upper limits at the 95% confidence level on R defined by Equations (Eq.5.1 and Eq.5.2). The solid red curve shows the observed limit while the solid black curve represents the expected limits in the absence of a signal, with the two shaded regions of this Brazil plot giving the $\pm 1\sigma$ and $\pm 2\sigma$ statistical uncertainty region with respect to the expected limits. No systematic uncertainty is included.

5.2 Upper limit for production of the X_b decaying to $\chi_b(1P)\pi^+\pi^-$

The calculation of the upper bound for the production of $X_b \to \chi_b(1P)\pi^+\pi^-$, where the $\chi_{b1}(1P)$ decays to $\Upsilon(1S)\gamma$, has been performed with respect to the production of $\chi_{b1}(1P) \to \Upsilon(1S)\gamma$.

Specifically the upper limit has been provided for the rate

$$R = \frac{\sigma(pp \to X_b + X) \times B(\to \chi_b(1P)\pi^+\pi^-) \times B(\chi_{b1}(1P) \to \Upsilon(1S)\gamma)}{\sigma(pp \to \chi_{b1}(1P) + X) \times B(\chi_{b1}(1P) \to \Upsilon(1S)\gamma)} \qquad (5.3)$$

namely, by removing from both nominator and denominator the common $B(\chi_{b1}(1P) \to \Upsilon(1S)\gamma)$:

$$R = \frac{\sigma(pp \to X_b + X) \times B(\to \chi_b(1P)\pi^+\pi^-)}{\sigma(pp \to \chi_{b1}(1P) + X)} \qquad (5.4)$$

that represents the inclusive production cross section in pp collisions of the hypothetical X_b state times its unknown branching fraction for its decay to $\chi_b(1P)\pi^+\pi^-$ final state, divided by the production cross section of the $\chi_{b1}(1P)$, where the $\chi_{b1}(1P)$ is in both cases (in both decay chains) reconstructed in its decay to $\Upsilon(1S)\gamma$.

Experimentally this ratio can be determined as the product of the ratio of the yields of X_b decaying to the $\chi_b(1P)\pi^+\pi^-$ final state (with the $\chi_{b1}(1P)$ subsequently decaying to

$\Upsilon(1S)\gamma$) and $\chi_{b1}(1P)$ (subsequently decaying to the same final state $\Upsilon(1S)\gamma$) multiplied by the inverse ratio of the corresponding reconstruction efficiencies:

$$R = \frac{N_{X_b}}{N_{\chi_{b1}(1P)}} \times \frac{\epsilon_{\chi_{b1}(1P)}}{\epsilon_{X_b}} \tag{5.5}$$

where:

- N_{X_b} is the $X_b \to \chi_b(1P)\pi^+\pi^-$ yield (with $\chi_{b1}(1P) \to \Upsilon(1S)\gamma$),

- $N_{\chi_{b1}(1P)}$ is the $\chi_{b1}(1P) \to \Upsilon(1S)\gamma$ yield,

- $\epsilon_{\chi_{b1}(1P)}$ is the reconstruction (and selection) efficiency of the $\chi_{b1}(1P) \to \Upsilon(1S)\pi^+\pi^-$ signal,

- ϵ_{X_b} is the reconstruction (and selection) efficiency of the $X_b \to \chi_b(1P)\pi^+\pi^-$ signal (with the $\chi_{b1}(1P)$ subsequently decaying to $\Upsilon(1S)\gamma$).

5.2.1 Efficiency estimation

Monte Carlo samples for the decay $X_b \to \chi_b(1P)\pi^+\pi^-$ and $\chi_{b1}(1P) \to \Upsilon(1S)\gamma$, have been used to estimate the total reconstruction efficiency for each decay channel. To correctly estimate the efficiency the reconstructed candidates (muons, other tracks, photons) need to be matched to the generated particles in order to remove the purely combinatorial background and the possible reconstruction multiplicity mostly induced by pileup events.

The total efficiency is defined as the ratio between the number of reconstructed candidates at the end of the whole selection chain and the number of generated candidates in the sample.

The relative efficiency has been estimated as the inverse of the ratio of the total reconstruction efficiency for $\chi_{b1}(1P) \to \Upsilon(1S)\gamma$ and of that for $X_b \to \chi_b(1P)\pi^+\pi^-$ (with $\chi_{b1}(1P) \to \Upsilon(1S)\gamma$).

The results of these calculations are listed in Table 5.12 for 5 different X_b mass values used at generation level, also considering different conditions corresponding to the 3 different years of data taking. These values of the reconstruction efficiency for $X_b \to \chi_b(1P)\pi^+\pi^-$ are also reported in the plot shown in Figure 5.13, whereas the corresponding values of the reconstruction efficiency for $\chi_{b1}(1P) \to \Upsilon(1S)\gamma$ are reported in the plot shown in Figure 5.13.

5.2.2 Mass Resolution estimation for signal modelling

Another ingredient needed in the upper bound extraction for the rate R is the parametrization of the signal and background PDFs. Let us start from the signal model that requires

58

Chapter 5. Estimation of an upper limit on the production of X_b decaying into $\Upsilon(1S)\pi^+\pi^-$ and $\chi_b(1P)\pi^+\pi^-$ final states

M[X_b]	**2016 MC samples**		**2017 MC samples**		**2018 MC samples**	
	ϵ_{X_b}	ϵ_{rel}	ϵ_{X_b}	ϵ_{rel}	ϵ_{X_b}	ϵ_{rel}
10.3	0.003	0.681	0.004	0.694	0.004	0.718
10.5	0.002	0.598	0.002	0.621	0.003	0.633
10.7	0.002	0.538	0.002	0.572	0.002	0.574
10.9	0.001	0.505	0.002	0.488	0.002	0.518
11.1	0.001	0.437	0.002	0.461	0.002	0.460

FIGURE 5.12: Summary table for the efficiency calculations of $X_b \rightarrow \chi_b(1P)\pi^+\pi^-$ for 2016, 2017 and 2018 MC samples, as a function of the generated X_b mass. The efficiency ratio (as defined in the text) is also provided for the three years.
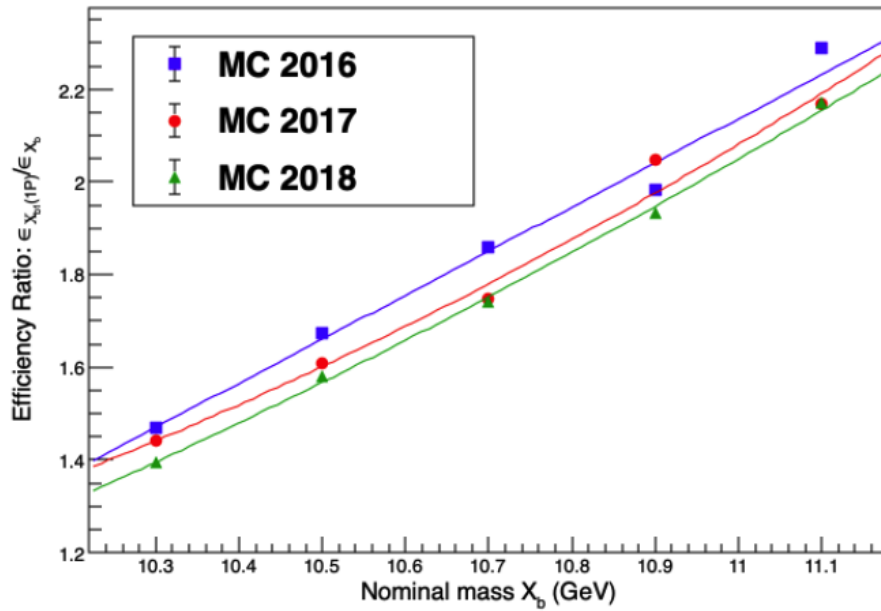

FIGURE 5.13: Fits on the efficiency ratios, ϵ_{ratio}, obtained from 2016, 2017 and 2018 MC samples.

the prior knowledge of the mass resolution as a function of the mass itself. The procedure for the determination of the mass resolution consists in generating a set of signal MC samples, one for each of the three years of data taking, with the generated X_b candidates' width set to zero. In this case the width of the signal associated to the reconstructed X_b candidates in the mass spectrum of interest, would represent the estimate of the experimental mass resolution. Five generation values of the mass of the signal X_b candidate have been chosen Table 5.14.

The 5 estimated mass resolutions are plotted as a function of the 5 generated invariant masses for all the three considered years in Fig 5.15.

M[X_b]	2016 MC samples σ_{X_b}[MeV]	2017 MC samples σ_{X_b}[MeV]	2018 MC samples σ_{X_b}[MeV]
10.3	3.350	3.080	2.960
10.5	5.970	5.250	5.640
10.7	8.420	7.740	7.710
10.9	10.510	9.840	9.820
11.1	12.610	12.410	12.010

FIGURE 5.14: Summary table of the mass resolution values characterizing the decay $X_b \to \chi_b(1P)\pi^+\pi^-$ and estimated by exploiting the 2016, 2017 and 2018 MC samples.

5.2.3 Background modelling

The background model has been extracted from data by fitting the full $\chi_b(1P)\pi^+\pi^-$ mass spectrum. Since the spectrum is very wide, it has been divided in 4 parts. The PDFs chosen for the background consist in Bernstein polynomial functions ranging from 4 to 6 degrees of freedom according to the fitted part of the spectrum. The four parts of the spectrum have been fitted with a background-only model, using Bernstein polynomials. The resulting fits are presented in Figures from 5.16 to 5.19. The overlap between the 4 mass regions has been considered on purpose to allow smooth transitions when determining the upper limit for the rate R.
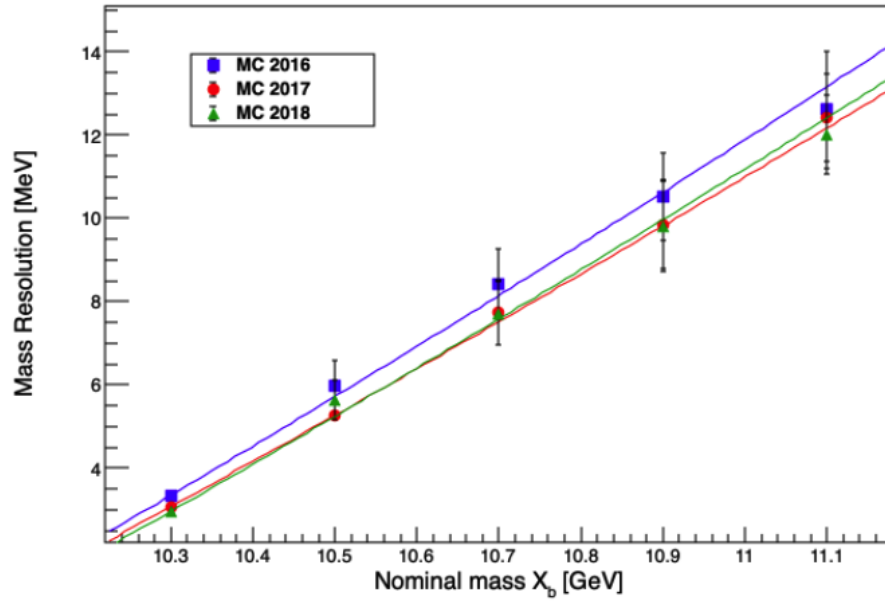
FIGURE 5.15: Superimposed fits to the estimated mass resolutions (points), obtained for 2016, 2017 and 2018 MC samples.
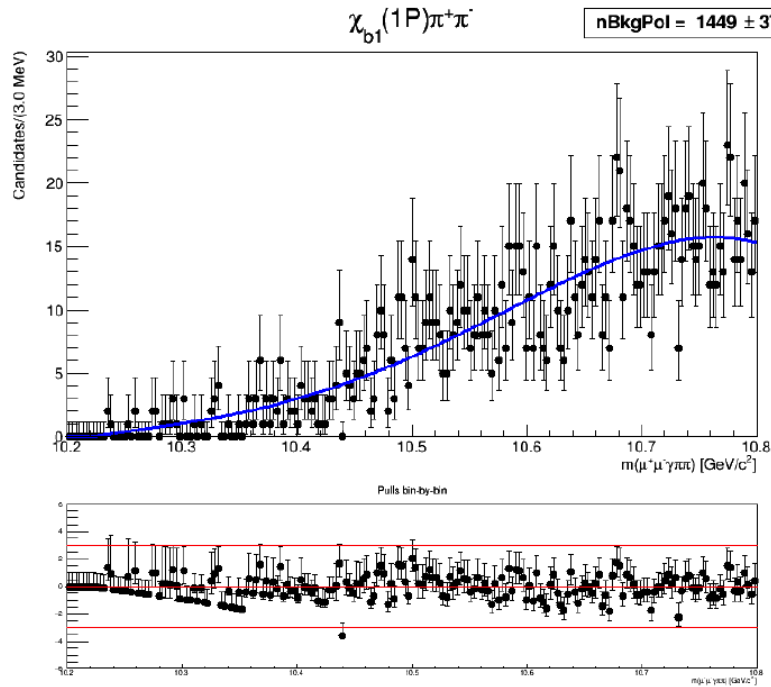

FIGURE 5.16: Background shape determination by fitting with Bernstein polynomials the first part of the $\chi_b(1P)\pi^+\pi^-$ mass spectrum in the data. Bin-by-bin pulls provide the goodness-of-fit.
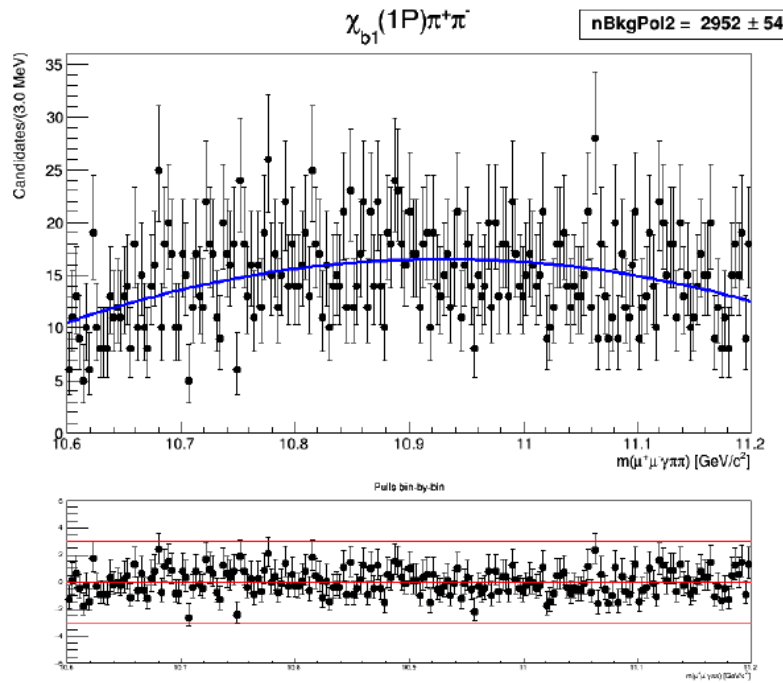
FIGURE 5.17: Background shape determination by fitting with Bernstein polynomials the second part of the $\chi_b(1P)\pi^+\pi^-$ mass spectrum in the data. Bin-by-bin pulls provide the goodness-of-fit.

FIGURE 5.18: Background shape determination by fitting with Bernstein polynomials the third part of the $\chi_b(1P)\pi^+\pi^-$ mass spectrum in the data. Bin-by-bin pulls provide the goodness-of-fit.

FIGURE 5.19: Background shape determination by fitting with Bernstein polynomials the fourth part of the $\chi_b(1P)\pi^+\pi^-$ mass spectrum in the data. Bin-by-bin pulls provide the goodness-of-fit.
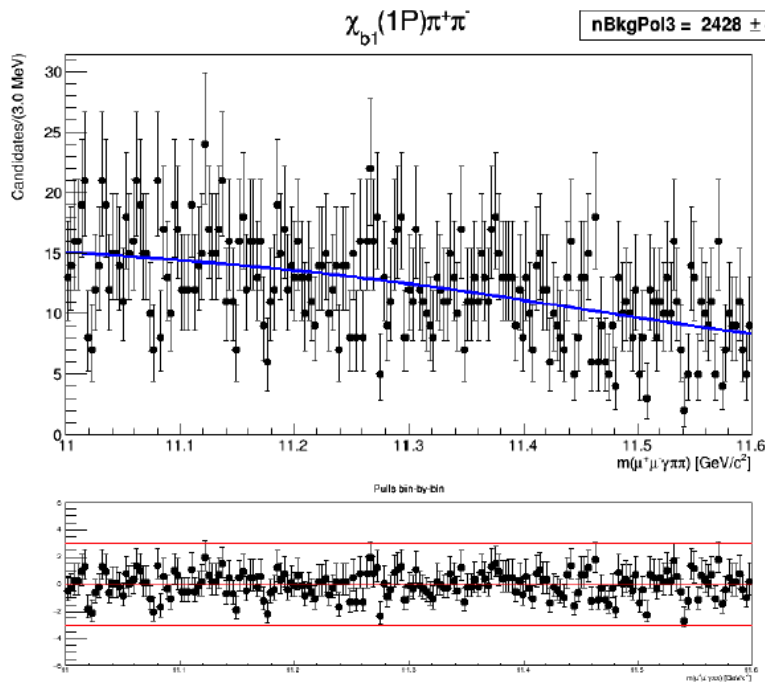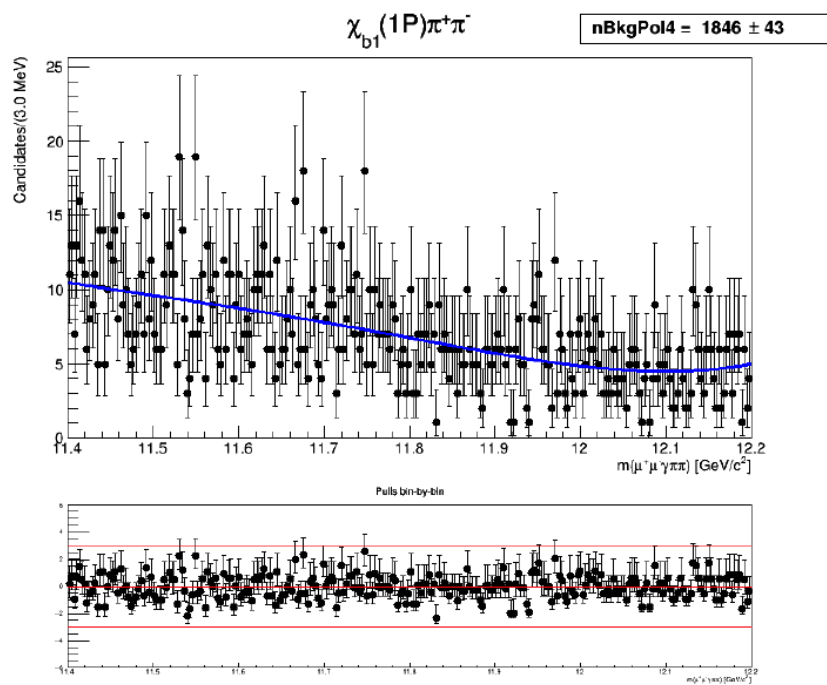
5.2.4 *p*-value calculation and upper limit estimation

Now that all the ingredients for the upper limit extraction have been set up it is possible to proceed with the *p*-value calculation and the upper limit estimation for the rate R. The local *p*-values are calculated, as a function of the X_b mass, by using a profile likelihood ratio as test statistics and an asymptotic approach, as already mentioned at the beginning of this chapter. The expected and observed 95% confidence level upper limits on R are derived, as a function of the X_b mass, by using a modified frequentist approach (asymptotic CLs method), as already mentioned.

Both *p*-value and upper limit on R are provided in the mass range [10.25, 12.0] GeV. As background models (one for each region) have been used the ones extracted in the last subsection, whereas as a signal it is used a simple gaussian with its standard deviation strictly related to the mass resolution as previously discussed. The local *p*-value is presented in Figure 5.20, whereas the upper limits on R are presented in Figure 5.21. The smallest local p-value is ~ 0.004 at ~ 10.5 GeV, corresponding to a statistical significance of $\sim 2.5\sigma$. This would be certainly rather diluted when taking into account the lookelsewhere effect if dealing with an hypothetical exotic X_b state. The observed upper limits on R are in the range 0:08 - 1.5% at 95% CL depending on the X_b assumed mass. No systematic uncertainties are included when quoting this range of values.
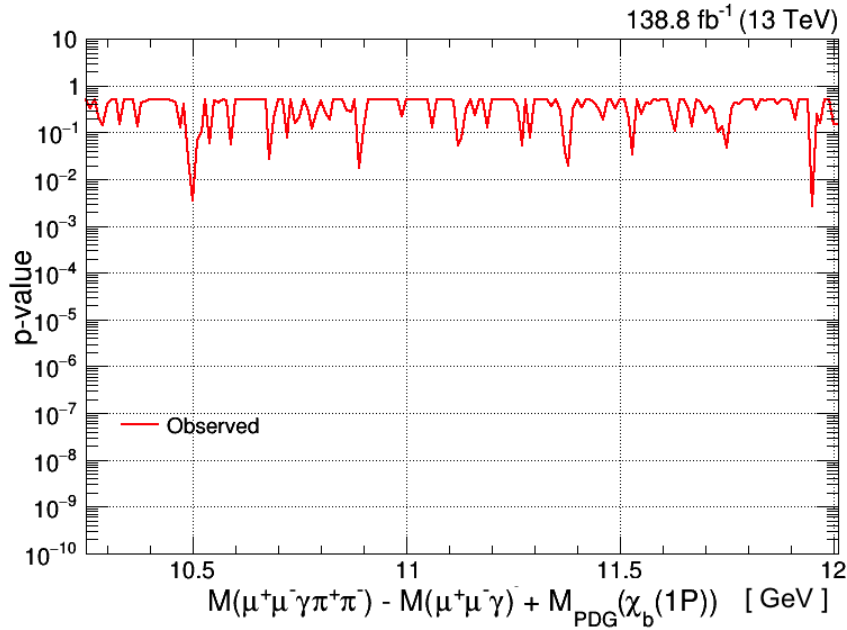

FIGURE 5.20: Observed mass dependent p-value for $X_b \to \Upsilon(1S)\pi^+\pi^-$ final state. No systematic uncertainty included.
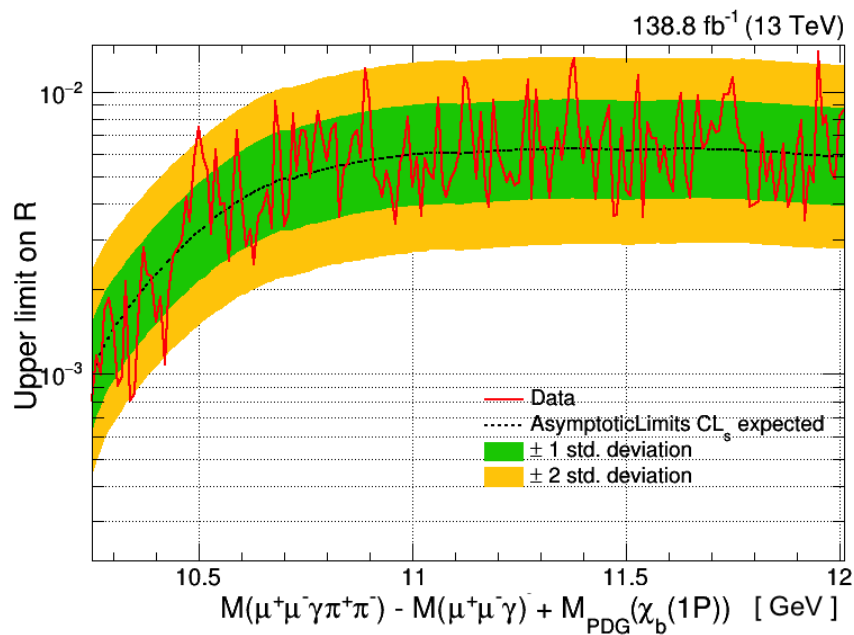
FIGURE 5.21: Upper limits at the 95% confidence level on R. The solid red curve shows the observed limit while the solid black curve represents the expected limits in the absence of a signal, with the two shaded regions of this Brazil plot giving the $\pm 1\sigma$ and $\pm 2\sigma$ statistical uncertainty region with respect to the expected limits. No systematic uncertainty is included.

Chapter 6

Conclusions

In this thesis two independent analysis were presented; The search for the $B_c(2S)^+$ and $B_c(2S)^{*+}$ states performed at the CMS experiment with an event sample of pp collisions, corresponding to an integrated luminosity of 140 fb^{-1}, at a center-of-mass energy of 13 TeV, collected in 2016, 2017 and 2018. We reconstruct signals consistent with $B_c(2^1S_0)^+$ and $B_c(2^3S_1)^+$ with a local significance larger than six standard deviations. This result shows for the first time the two-peak structure of the $B_c(2S)^{(*)+}$ system. The measured masses of this two-peaks structure is:

$$\Delta M = 29.0 \pm 1.5 \,(\text{stat}) \pm 0.7 \,(\text{syst}) \,\text{MeV}, \tag{6.1}$$

$$M(B_c(2S)^+) = 6871.0 \pm 1.2 \,(\text{stat}) \pm 0.8 \,(\text{syst}) \pm 0.8 (B_c^+) \,\text{MeV} \tag{6.2}$$

the last result uses the B_c^+ mass $M(B_c^+) = 6274.9 \pm 0.8$ MeV [38].

The mass measurements of this structure on the observed decay modes are consistent with expectations of $B_c(2S)^+$ and $B_c(2S)^{*+}$, and will provide essential information on the nature and production mechanism of the $(c\bar{b})$ system.

After the observation of the $B_c(2S)^+$ and $B_c(2S)^{*+}$ states presented here, perspective analysis involves the measurement of production ratios and other characteristics. The determination of the production rates would provide useful information to improve the knowledge of the B_c^+ family. Further studies to characterize the new observed states are also important. In this sense, it is interesting to see whether the dipion mass spectra in the cascade decays $B_c(2S)^{*+} \rightarrow B_c^+ \pi^+ \pi^-$ and $B_c(2S)^+ \rightarrow_c^+ \pi^+ \pi^-$ follow the pattern seen in $\psi(2S) \rightarrow J/\psi \pi^+ \pi^-$ and $\Upsilon(2S) \rightarrow \Upsilon(1S)\pi^+\pi^-$ decays.

In the second work an analysis of $\Upsilon(1S)\pi^+\pi^-$ and $\chi_b(1P)\pi^+\pi^-$ final states, with the aim to search for exotic bottomonium-like signals, is presented by exploiting the full data sample collected during the 2106-2018 data taking by the CMS experiment; this Run-II subsample, corresponding to an integrated luminosity of 139 fb^{-1}, was collected at the LHC, in proton-proton collisions at a center-of-mass energy of 13 TeV, by using

dedicated triggers based on the selection of two muons coming from a $\Upsilon(1S)$ decay.

Within this preliminary study no significant exotic peaking structures have been reported across the whole two investigated mass spectra. Consequently the mass-dependent Upper Limits on the relative production rate of any X_b state with respect to $\Upsilon(2S)$ and χ_{b1} production have been calculated by exploiting the $\Upsilon(1S)\pi^+\pi^-$ and $\chi_b(1P)\pi^+\pi^-$ final states respectively, and by using the CMS combine statistical tool.

The presented analysis introduces also the calculation of some expected systematic uncertainties, although further studies will be needed to determine deeper its behavior and impact on the final upper limits setting. With respect to the selection criteria, a new approach is being investigated by applying machine learning algorithms. These steps are the route towards the CMS publication.

Appendix A

Cross checks B_c^+ analysis

In order to check the consistency of the analysis, we have performed the usual splitting sample tests, where we have divided the data sample in two halves based of kinematical regions, which could give some information about inconsistencies in the reconstruction of the B_c^+ $\pi^+\pi^-$ system.

Figure A.1 shows the mass distributions when we consider the regions 15–25 GeV, and 15–30 GeV for the lower p_T region of B_c^+. For higher p_T we consider the complementary regions, e.g. greater than 25 and 30 GeV. It is clear that for higher p_T of B_c^+, the significance improves, which is expected, due to the reduced phase space of the system, a higher p_T will imply that the soft pions could have higher p_T, making them easier to reconstruct.

Figure A.2 shows the mass distributions for two regions of the detector: the barrel region, $|y|$ of B_c^+ lower than 0.8 units, and the forward region, $0.8 < |y| < 2.4$. The distributions are more significant for the barrel region as expected, since the mass resolutions in that part of the detector is usually better. The signal almost vanishes for the forward region.

Figure A.3 shows the mass distributions for the 2016 and 2017 data taking periods. It is clear than the quality of the data for the 2017 data is better than for 2016. This has been observed in other analyses. The higher PU is compensate by the high p_T applied in the current analysis.

A.1 Other signal models

For $B_c(2S)^+$ and $B_c(2S)^{*+}$, besides of the Single Gaussian and Breit Wigner functions, other models were tested. Figure A.4 shows the mass distributions when we have changed to Crystal Ball (left) and Double-side Crystal Ball (right). We have determined the parameters of the tails in those Crystal Ball and Double-side Crystal Ball functions based on previous experience. The fits results are not used in the current analysis. Besides Figure A.5 shows a fit with the width fixed from MC samples in the left plot, while in the right one is the fit, when the ratio of the widths is fixed from the ratio of the
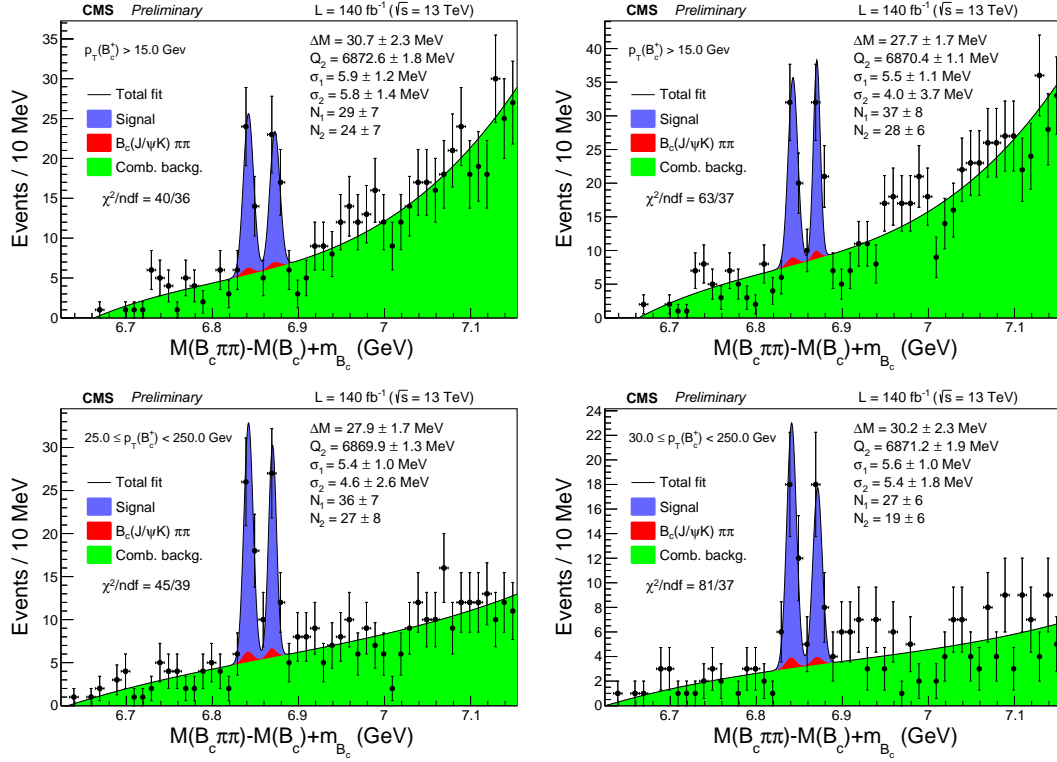
FIGURE A.1: Upper plots show the B$_c^+$ $\pi^+\pi^-$ mass distributions for p_T of the B$_c^+$ in the 15–25, and 15–30 GeV range. Lower plots show the same distributions for p_T of B$_c^+$ greater than 25 and 30 GeV.
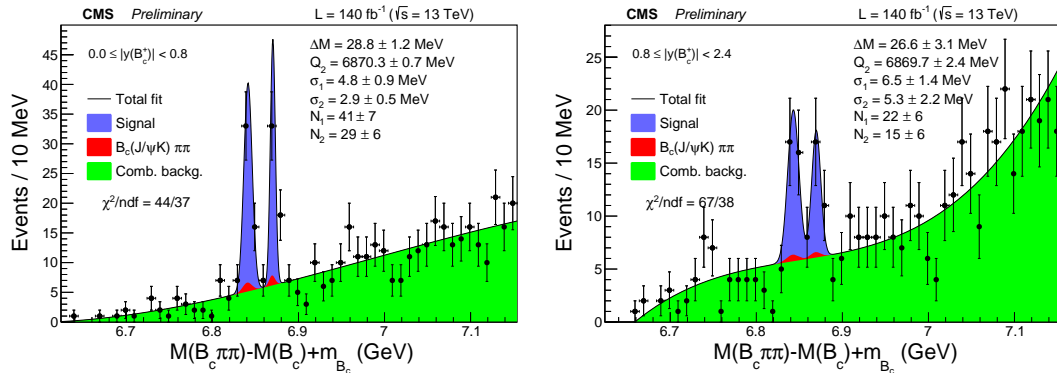

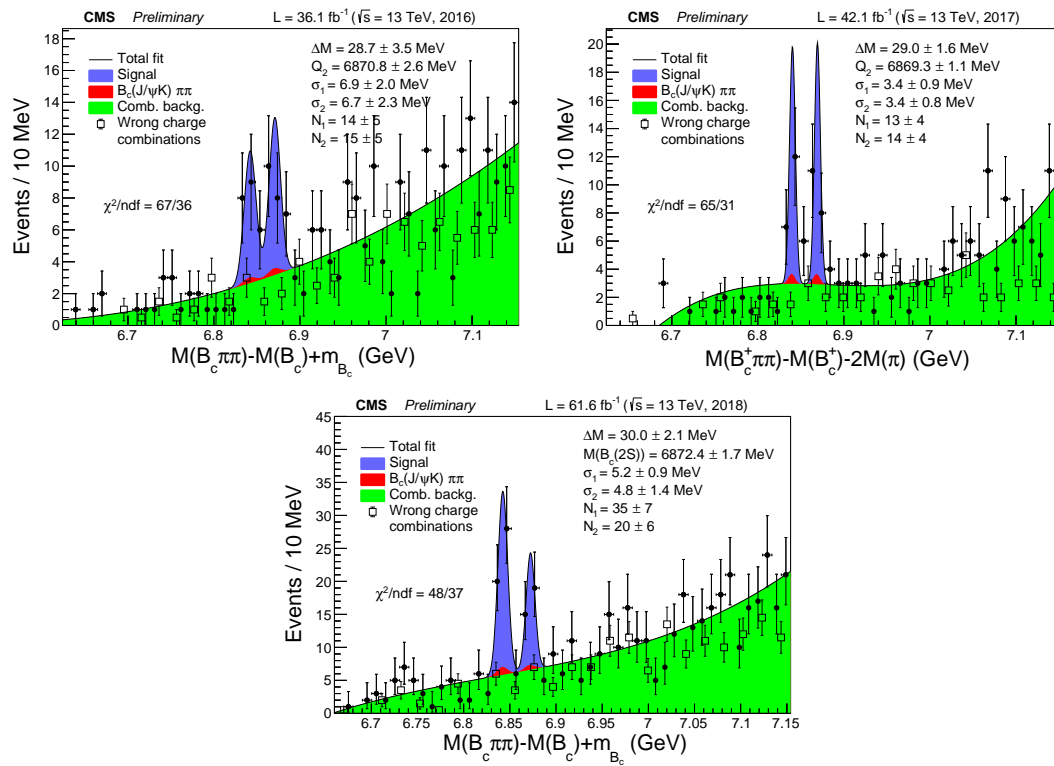FIGURE A.2: B$_c^+$ $\pi^+\pi^-$ mass distributions for central and forward B$_c^+$ mesons.

FIGURE A.3: $B_c^+ \pi^+\pi^-$ mass distributions for 2016, 2017 and 2018 data taking periods.

widths in MC. The significance of these two latest fits is 6.07 and 6.18 for the left plot, and 6.09 and 6.18 for the right plot, respectively for the two peaks as shown in each Q distribution.
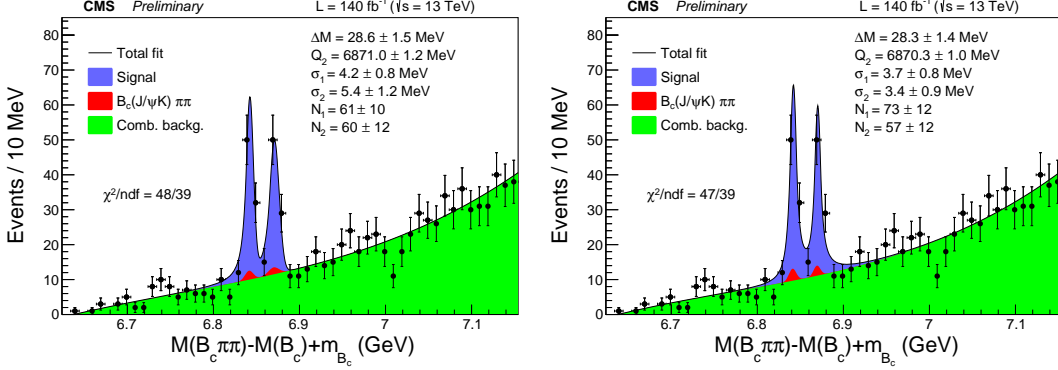

FIGURE A.4: The Q invariant mass distribution (2016+2017+2018), using alternative signal models. Crystal Ball (left) and Double-side Crystal Ball (right).
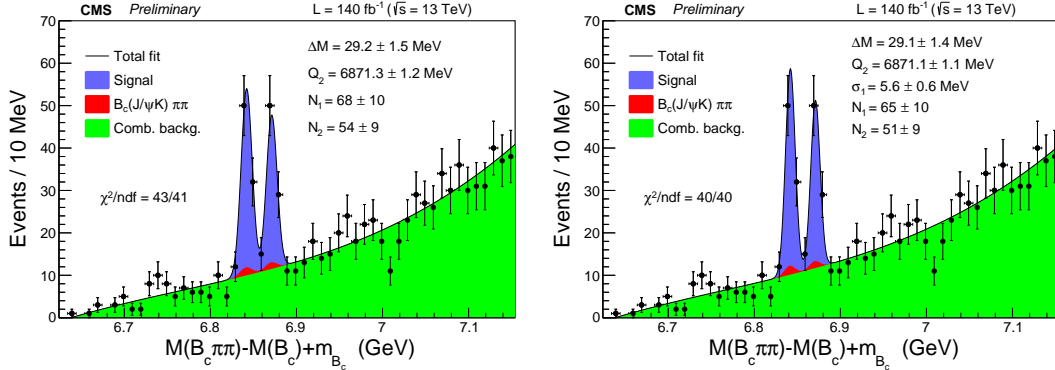

FIGURE A.5: The Q invariant mass distribution (2016+2017+2018), using width fixed from MC samples (left) and ratio of the widths fixed from MC.

A.2 Wrong-sign background and side-band studies

From Figure 3.5 the Wrong-Sign (WS) normalization looks slighter lower than the Right-Sign (RS), however they are consistent, as can be seen in the following Figure A.6. The left plot show the nominal RS fit (with a band, showing the statistical uncertainty) on top of the WS data. The right plot, shows the RS and WS distributions with the band for RS and a fit to the WS.

On the other hand in figure A.7 the Q distribution for the B_c^+ side-bands is shown. The B_c^+ side-bands are defined as $5\sigma < |M(J/\psi + \pi) - M(B_c(\text{fitted}))| < 10\sigma$. No-peak

structure is observed above the background shape. The WS background distribution is also overlayed in the plot.
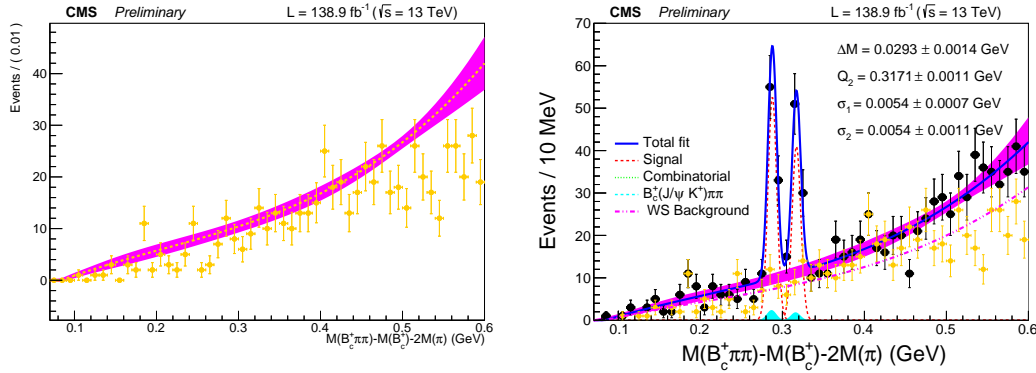

FIGURE A.6: Right-Sign (RS) fit (with a band, showing the stat uncertainty) on top of the Wrong-Sign (WS) data (left). RS and WS distributions with the band for RS and a fit to the WS (right).
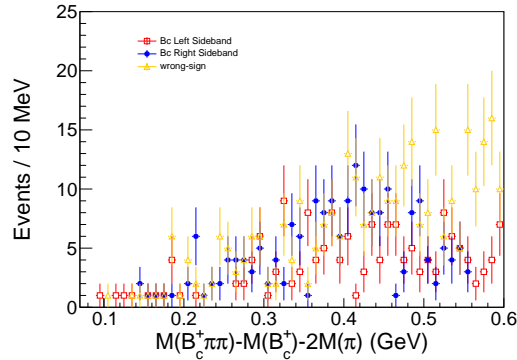

FIGURE A.7: Q distribution for the B_c side-bands and WS distributions.

A.3 Kinematical selection

Figure A.8 shows the significance of B_c^+ for different cut combinations in p_T (B_c^+) and p_T (π_1). The nominal selection of B_c^+ is based on previous PAG studies, but the study performed here, shows that the combination of p_T (B_c^+)> 15 and p_T (π_1)> 3.5 is indeed a good choice, making the current analysis selection robust enough for the B_c^+ selection.

Having B_c^+ already robust enough, we look at the remaining cuts: those for the "soft pions" and the vertex signal candidate $B_c\pi\pi$. Tables A.1 show the number of events after the given cut for data side-bands in Q distribution and Monte Carlo simulated signal events. Taking the ratio of the number of MC events over the number of side-band events or the number of MC events over the square root of the sum of MC and side-band events (significance-like) show that the cut on $p_T(\pi_2)$ and the chosen of the
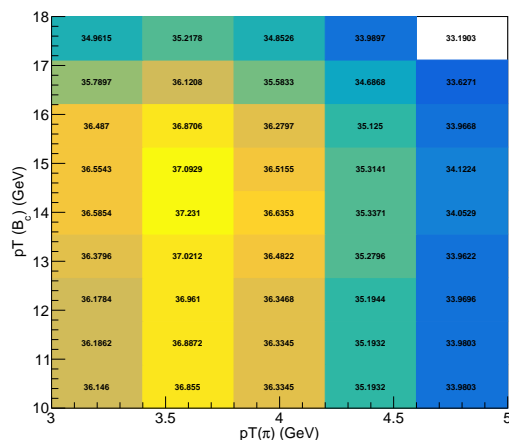
FIGURE A.8: Significance of B$_c^+$ as a function of p_T (B$_c^+$) and p_T (π_1).

best candidate are robust enough. For $p_T(\pi_3)$ the numbers may suggest that the cut at 0.5 GeV is slightly better, however a compromise of a bigger background rejection, tend to suggest that the higher we can go would be better. Then the current selection looks robust enough.

Figure A.9 shows the mass distributions when the p_T of the charged hadron tracks π_1 and the p_T of the B$_c^+$ hadrons are required to have different cuts. The distributions are consistent across the combinations tested. The different p_T used are shown in the legends.

A.4 Test of the fitting algorithm with pseudo-experiments

The fitting algorithm is tested in samples generated randomly according to the likelihood defined in section 3.2.3, with known input parameters (equal to the results of the nominal fit to data). The total number of events in each sample correspond to the number of events in the data sample. This study allows to calculate a possible statistic bias due to the fitting algorithm. The results of the toy study made of the ΔM and Q_2 and distributions of the pulls (difference of the fitted values obtained for each sample with respect to input valued divided by the uncertainties) are plotted in Fig. A.10, showing no significant biases or uncertainties misestimations.
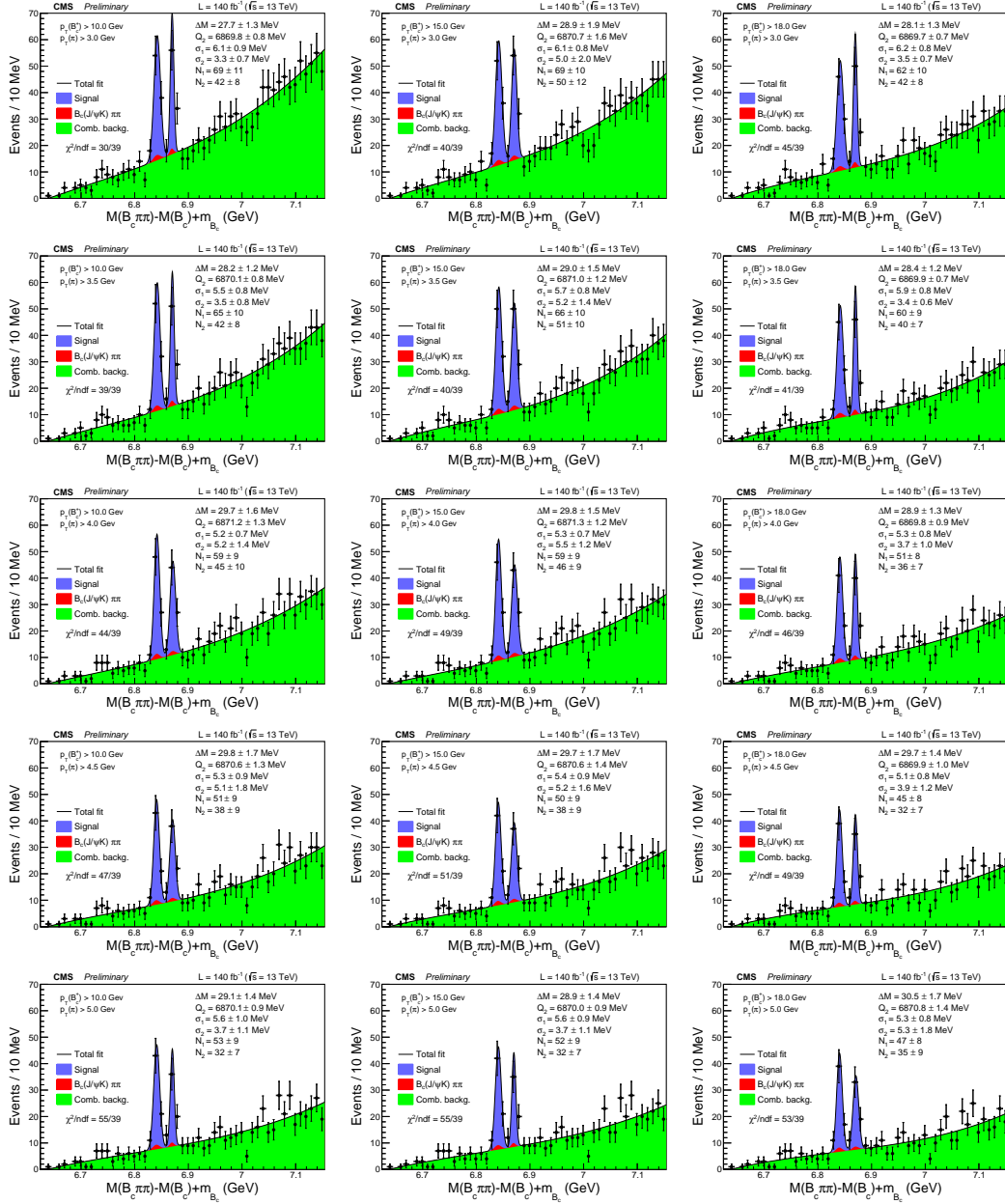
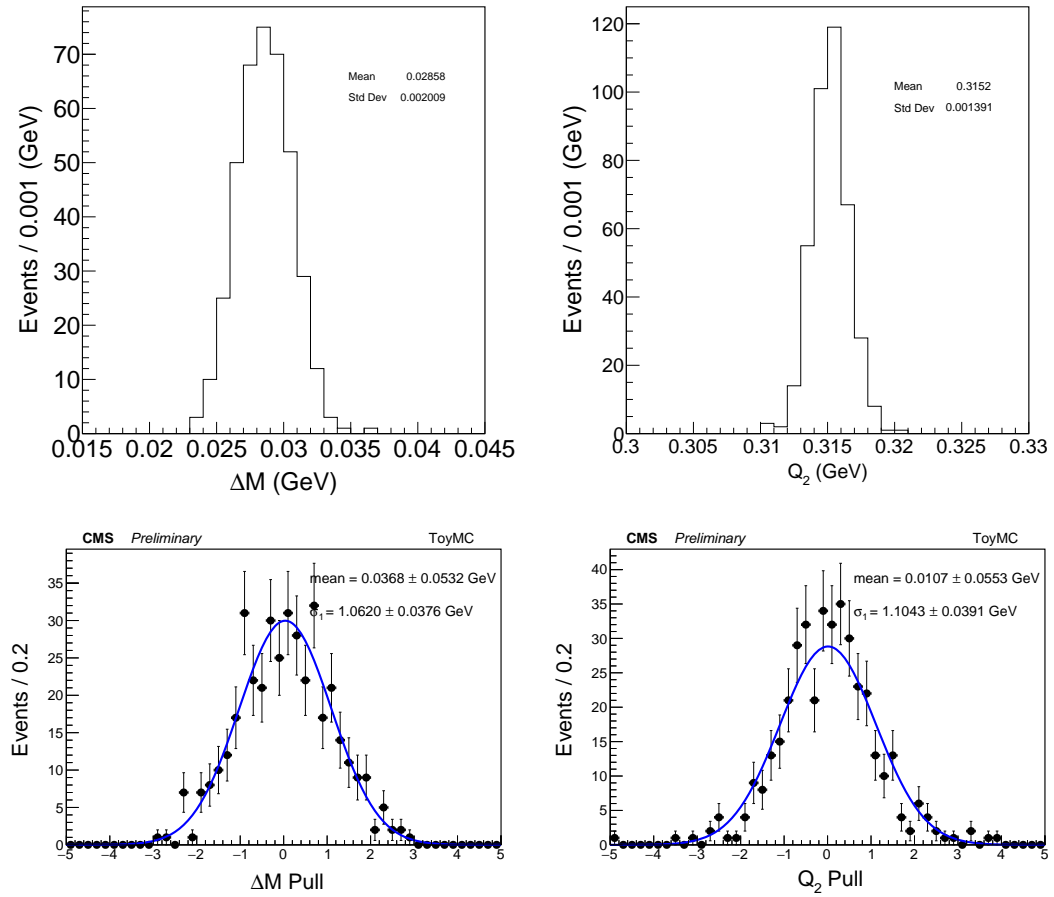FIGURE A.9: The Q invariant mass distribution (2016+2017+2018), using alternative B_c^+ and π_1 cuts.

FIGURE A.10: Verification that the fit is unbiased and that the statistical uncertainties are properly computed, for the fitted ΔM and Q_2 values, using a toy study

cut	data side-band	MC signal	significance-like	B reject
$p_T(\pi_2) > 0.50\,\text{GeV}$	416	2045	41.2	1.00
$p_T(\pi_2) > 0.55\,\text{GeV}$	409	2045	41.3	0.98
$p_T(\pi_2) > 0.60\,\text{GeV}$	399	2045	41.4	0.96
$p_T(\pi_2) > 0.65\,\text{GeV}$	385	2037	41.4	0.93
$p_T(\pi_2) > 0.70\,\text{GeV}$	370	2022	41.3	0.89
$p_T(\pi_2) > 0.75\,\text{GeV}$	350	2010	41.4	0.84
$p_T(\pi_2) > 0.80\,\text{GeV}$	337	1984	41.2	0.81
$p_T(\pi_2) > 0.85\,\text{GeV}$	321	1946	40.9	0.77
$p_T(\pi_2) > 0.90\,\text{GeV}$	309	1907	40.5	0.74
$p_T(\pi_3) > 0.50\,\text{GeV}$	377	2257	44.0	0.91
$p_T(\pi_3) > 0.55\,\text{GeV}$	358	2132	42.7	0.86
$p_T(\pi_3) > 0.60\,\text{GeV}$	337	1984	41.2	0.81
$p_T(\pi_3) > 0.65\,\text{GeV}$	321	1838	39.6	0.77
$p_T(\pi_3) > 0.70\,\text{GeV}$	301	1694	37.9	0.72
candidate on p_T	337	1984	41.2	0.81
candidate on vtx prob.	329	1960	41.0	0.79

TABLE A.1: Number of events after each cut in the Q mass distribution for $B_c^+ \pi\pi$ reconstruction in data side-bands and MC signal simulations. significance-like numbers and background rejection are also presented.

Appendix B

Cross checks X_b analysis

B.1 Mass resolution studies

### B.1.1 $X_b \to \Upsilon(1S)\pi^+\pi^-$ decay mode

The mass resolution in the reconstruction of the decay $X_b \to \Upsilon(1S)\pi^+\pi^-$ has been studied generating signal MC samples with different X_b masses, all of them with a null generated width. These distributions are presented with superimposed the result of the fit with two Gaussian functions sharing the same mean. The mass resolution is calculated as the weighted average of the two standard deviations.

$X_b[10.1] \to \Upsilon(1S)\pi^+\pi^-$
$X_b[10.3] \to \Upsilon(1S)\pi^+\pi^-$
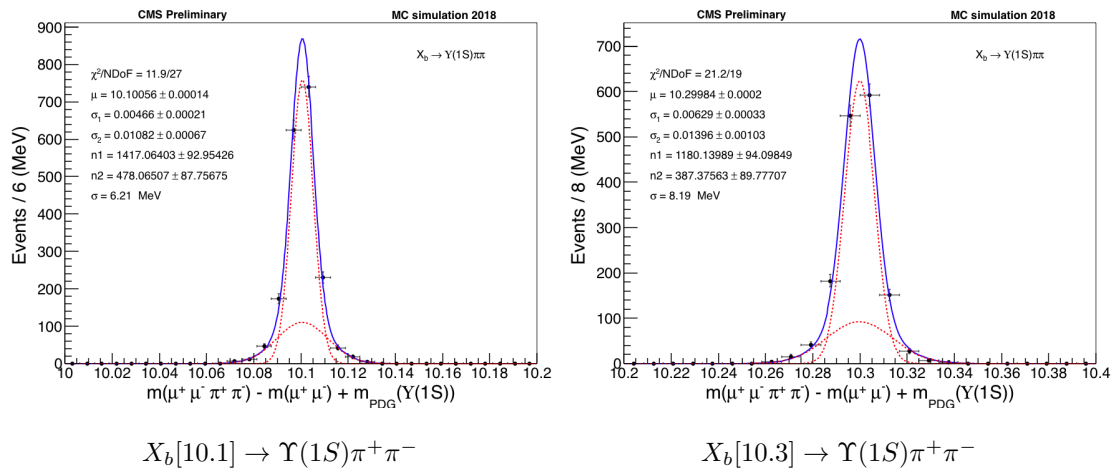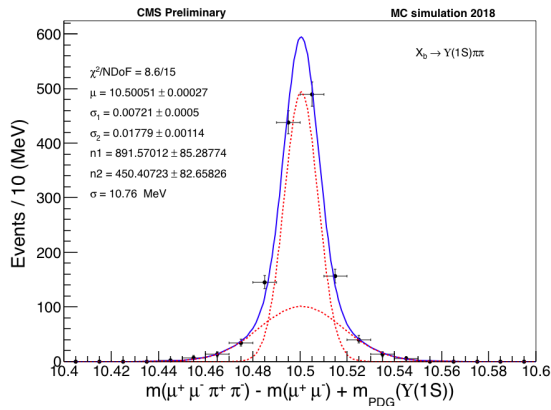
$X_b[10.5] \to \Upsilon(1S)\pi^+\pi^-$.
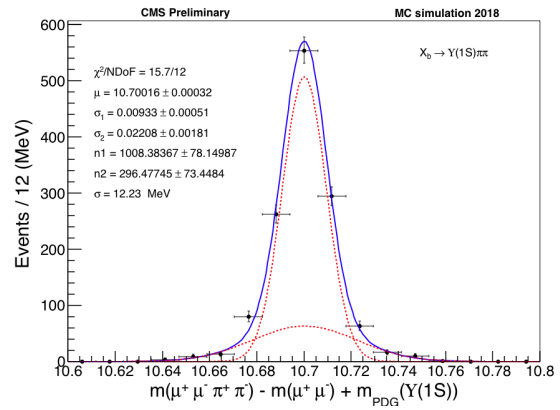
$X_b[10.7] \to \Upsilon(1S)\pi^+\pi^-$.
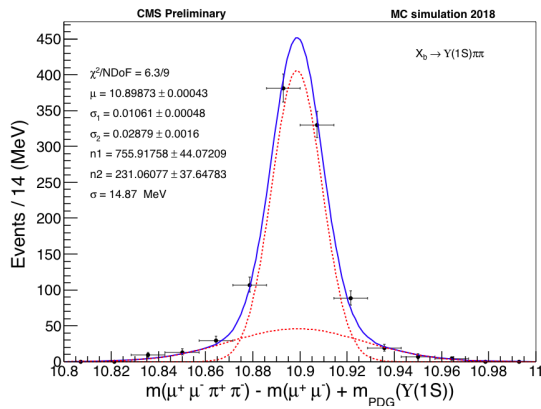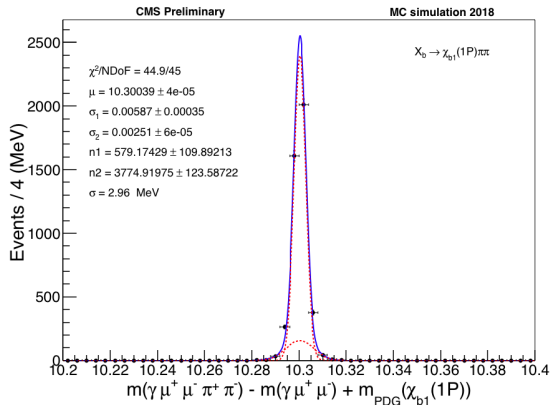

$X_b[10.9] \to \Upsilon(1S)\pi^+\pi^-$.
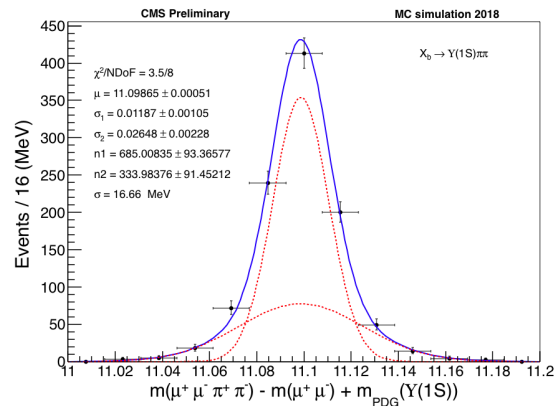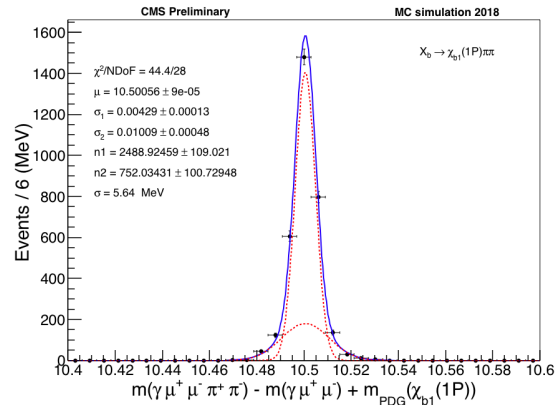

$X_b[11.1] \to \Upsilon(1S)\pi^+\pi^-$.

B.1.2 $X_b \to \chi_{b1}(1P)\pi^+\pi^-$ decay mode

$$X_b[10.3] \to \chi_{b1}\pi^+\pi^-$$

$$X_b[10.5] \to \chi_{b1}\pi^+\pi^-$$
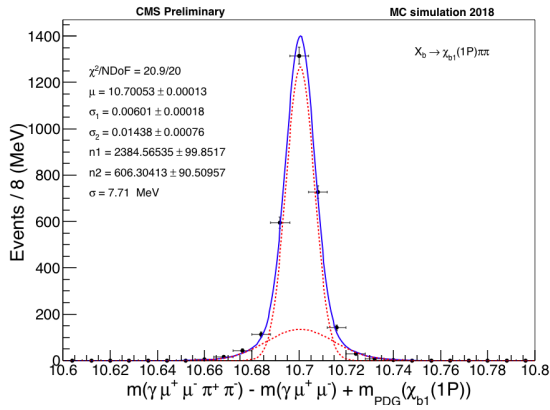
$$X_b[10.7] \to \chi_{b1}\pi^+\pi^-$$
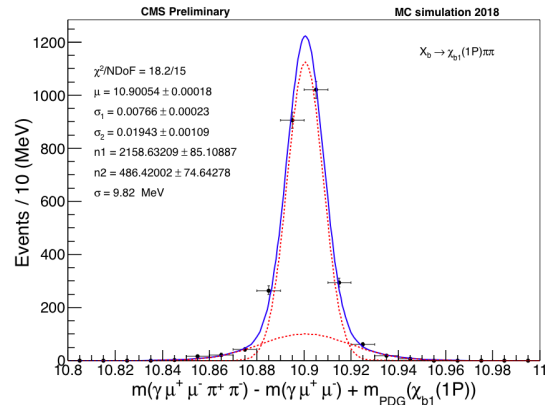
$$X_b[10.9] \to \chi_{b1}\pi^+\pi^-$$

B.2　Data and MC comparison

Comparison between data and simulated events (MC) has been checked to be sure there were no striking discrepancies that might have required to think about a re-weighting procedure for $X_b \to \Upsilon(1S)\pi^+\pi^-$ and $X_b \to \chi_{b1}(1P)\pi^+\pi^-$ decay modes.

B.2.1　$X_b \to \Upsilon(1S)\pi^+\pi^-$ **decay mode**

p_T　distribution　of $\Upsilon(1S)\pi^+\pi^-$ candidates.

η　distribution　of $\Upsilon(1S)\pi^+\pi^-$ candidates.

p_T distribution of $\Upsilon(1S)$ candidates.

η distribution of $\Upsilon(1S)$ candidates.

P_T distribution of leading π.

η distribution of leading π.
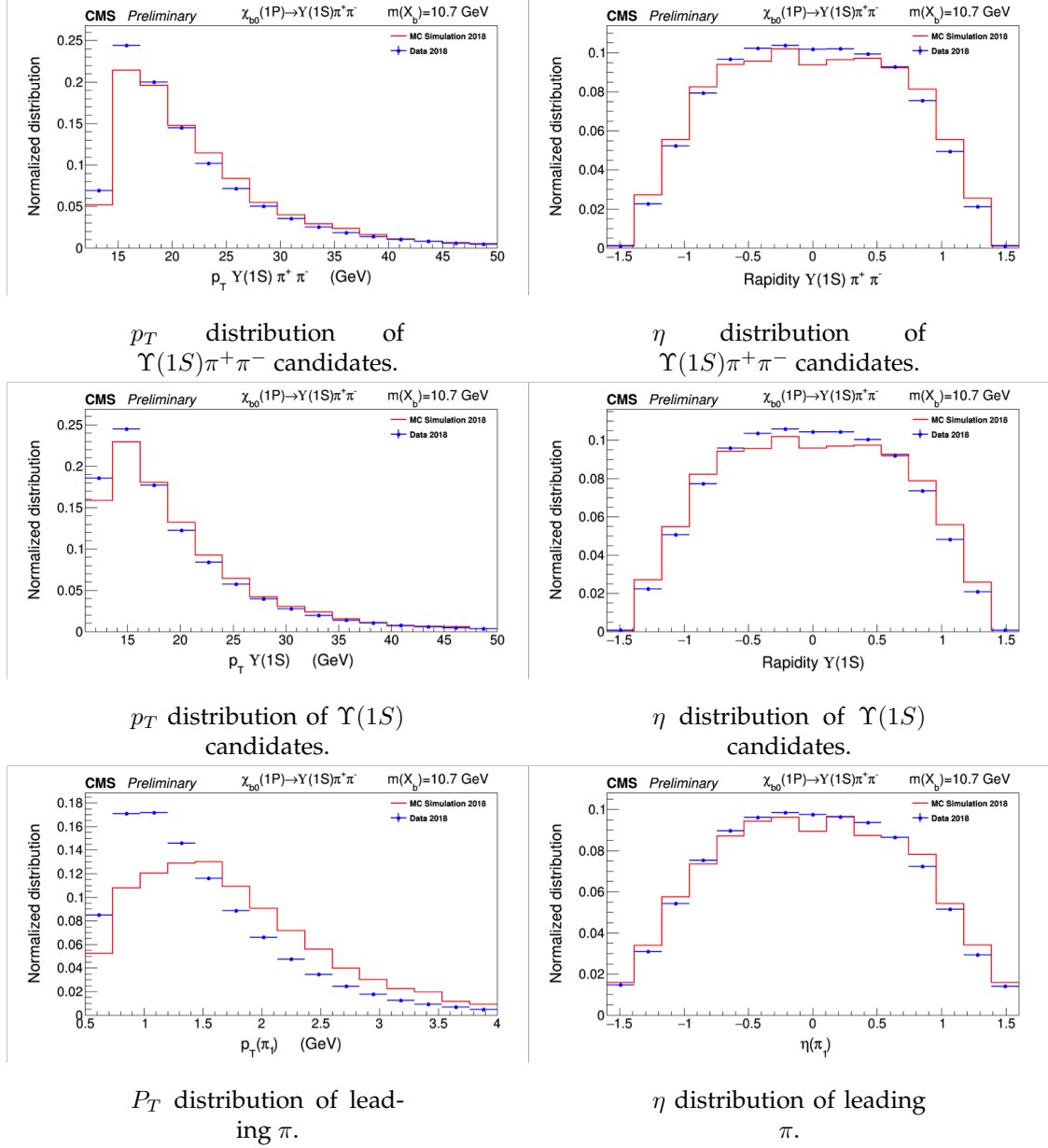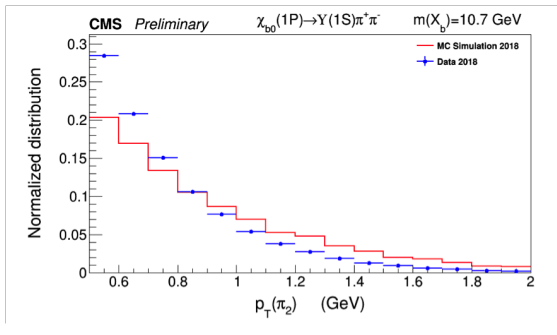
P_T distribution of softer π.
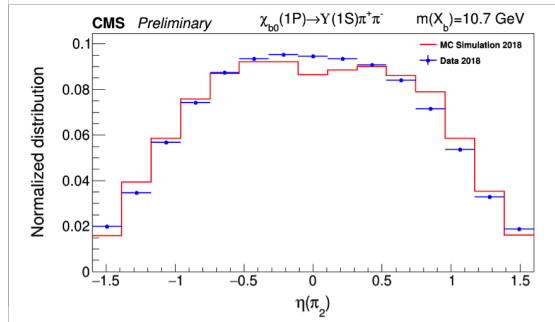
η distribution of softer π.
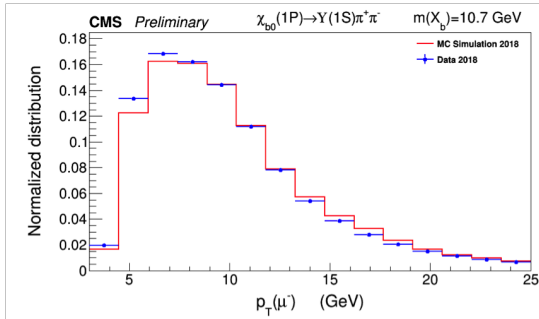
P_T distribution of $^-$.
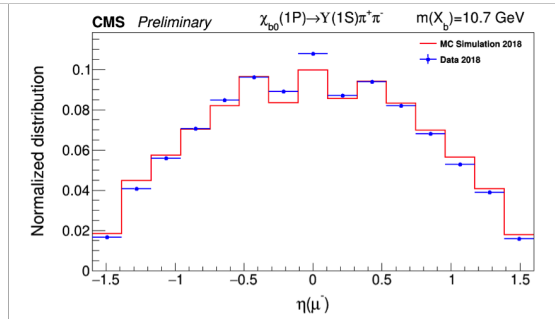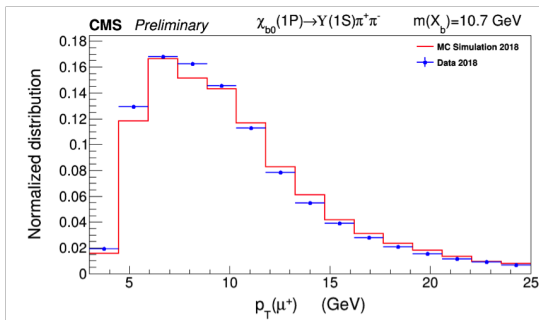
η distribution of $^-$.

P_T distribution of $^+$.
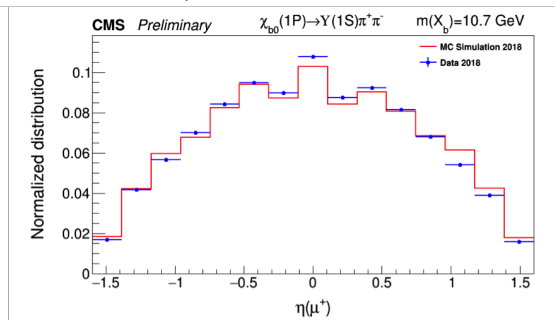
η distribution of $^+$.

B.2.2 $X_b \to \chi_{b1}(1P)\pi^+\pi^-$ decay mode
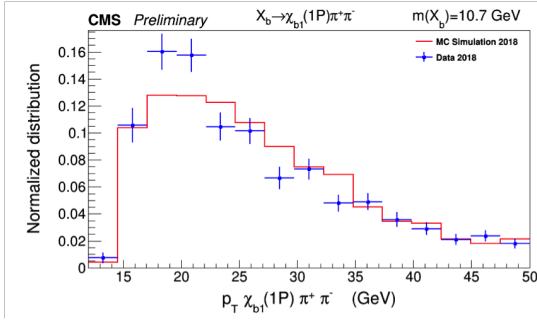
p_T distribution of $\chi_{b1}(1P)\pi^+\pi^-$ candidates.
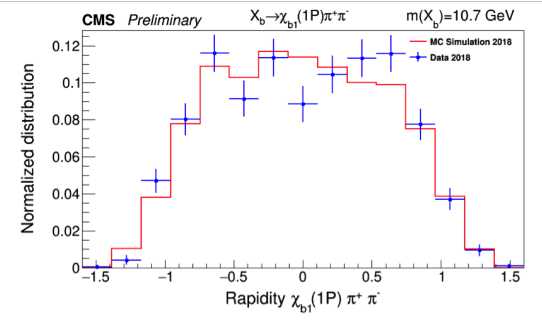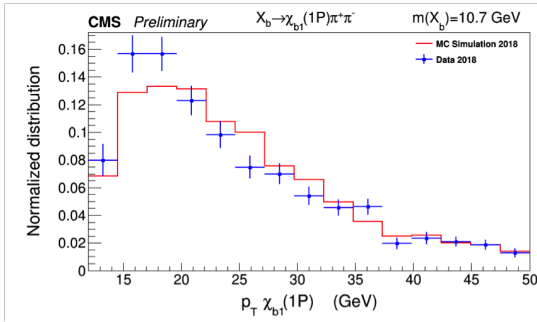
η distribution of $\chi_{b1}(1P)\pi^+\pi^-$ candidates.

p_T distribution of $\chi_{b1}(1P)$ candidates.
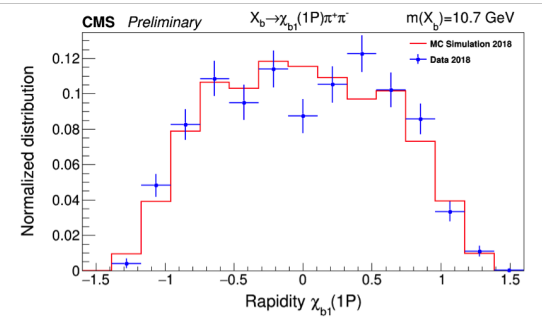
η distribution of $\chi_{b1}(1P)$ candidates.
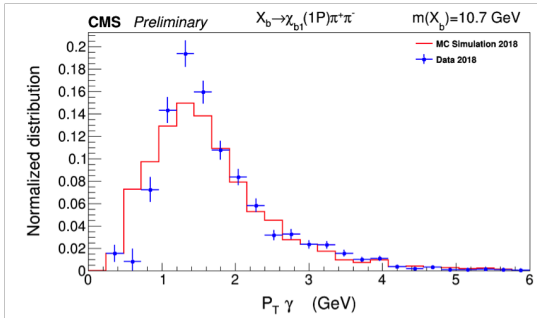
p_T distribution of γ candidates.
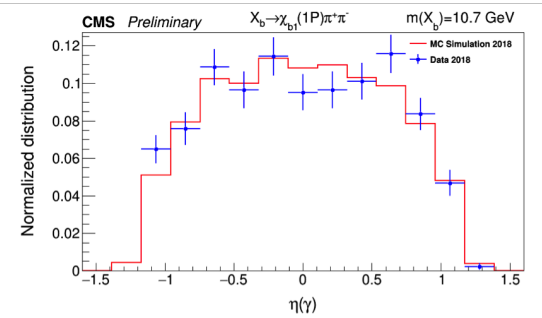
η distribution of γ candidates.
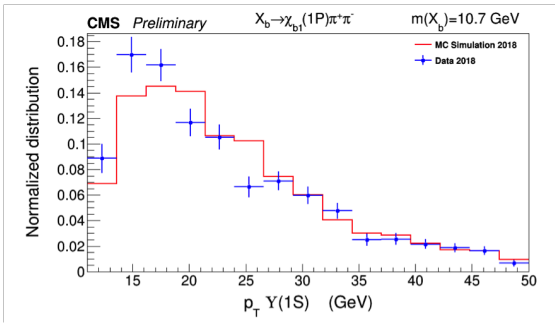
FIGURE B.29: p_T distribution of $\Upsilon(1S)$ candidates.

η distribution of $\Upsilon(1S)$ candidates.

P_T distribution of leading π.

η distribution of leading π.

P_T distribution of softer π.

η distribution of softer π.

P_T distribution of μ^-.

η distribution of μ^-.

P_T distribution of μ^+.　　　　　　　　　P_T distribution of μ^-.

Bibliography

[1] Jianming Bian. "A Review of Heavy Exotic States". In: (Nov. 2014).

[2] J. J. Aubert et al. "Experimental Observation of a Heavy Particle J". In: *Phys. Rev. Lett.* 33 (23 1974), pp. 1404–1406. DOI: `10.1103/PhysRevLett.33.1404`. URL: `https://link.aps.org/doi/10.1103/PhysRevLett.33.1404`.

[3] J. E. Augustin et al. "Discovery of a Narrow Resonance in e^+e^- Annihilation". In: *Phys. Rev. Lett.* 33 (23 1974), pp. 1406–1408. DOI: `10.1103/PhysRevLett.33.1406`. URL: `https://link.aps.org/doi/10.1103/PhysRevLett.33.1406`.

[4] S. L. Glashow, J. Iliopoulos, and L. Maiani. "Weak Interactions with Lepton-Hadron Symmetry". In: *Phys. Rev. D* 2 (7 1970), pp. 1285–1292. DOI: `10.1103/PhysRevD.2.1285`. URL: `https://link.aps.org/doi/10.1103/PhysRevD.2.1285`.

[5] S. W. Herb et al. "Observation of a Dimuon Resonance at 9.5 GeV in 400-GeV Proton-Nucleus Collisions". In: *Phys. Rev. Lett.* 39 (5 1977), pp. 252–255. DOI: `10.1103/PhysRevLett.39.252`. URL: `https://link.aps.org/doi/10.1103/PhysRevLett.39.252`.

[6] Eric Braaten, Christian Langmack, and D. Hudson Smith. "Born-Oppenheimer Approximation for the XYZ Mesons". In: *Phys. Rev. D* 90.1 (2014), p. 014044. DOI: `10.1103/PhysRevD.90.014044`. arXiv: `1402.0438 [hep-ph]`.

[7] S.-K. Choi et al. "Observation of a Narrow Charmoniumlike State in Exclusive $B^{\pm} \to K^{\pm}\pi^+\pi^- J/\psi$ Decays". In: *Phys. Rev. Lett.* 91 (26 2003), p. 262001. DOI: `10.1103/PhysRevLett.91.262001`. URL: `https://link.aps.org/doi/10.1103/PhysRevLett.91.262001`.

[8] Kamal K. Seth. "Heavy Quarkonia Results from CLEO". In: *Nuclear Physics B - Proceedings Supplements* 140 (2005). LATTICE 2004, pp. 344–346. ISSN: 0920-5632. DOI: `https://doi.org/10.1016/j.nuclphysbps.2004.11.294`. URL: `https://www.sciencedirect.com/science/article/pii/S0920563204008011`.

[9] S. Chatrchyan et al. "Search for a new bottomonium state decaying to œí(1S)œÄ+œÄ,àí in pp collisions at s=8 TeV". In: *Physics Letters B* 727.1 (2013), pp. 57–76. ISSN: 0370-2693. DOI: `https://doi.org/10.1016/j.physletb.2013.10.`

016. URL: `https://www.sciencedirect.com/science/article/pii/S0370269313008095`.

[10] Marek Karliner and Jonathan L. Rosner. "$X(3872)$, X_b, and the $\chi_{b1}(3P)$ state". In: *Phys. Rev. D* 91 (1 2015), p. 014014. DOI: `10.1103/PhysRevD.91.014014`. URL: `https://link.aps.org/doi/10.1103/PhysRevD.91.014014`.

[11] X. H. He et al. "Observation of $e^+e^- \to \pi^+\pi^-\pi^0\chi_{bJ}$ and Search for $X_b \to \omega\Upsilon(1S)$ at $\sqrt{s} = 10.867$ GeV". In: *Phys. Rev. Lett.* 113 (14 2014), p. 142001. DOI: `10.1103/PhysRevLett.113.142001`. URL: `https://link.aps.org/doi/10.1103/PhysRevLett.113.142001`.

[12] W Erdmann et al. "Upgrade plans for the CMS pixel barrel detector". In: *Nuclear Instruments and Methods in Physics Research Section A: Accelerators, Spectrometers, Detectors and Associated Equipment* 617.1-3 (2010), pp. 534–537.

[13] V Karimaki et al. *The CMS tracker system project: Technical Design Report*. Technical Design Report CMS. Geneva: CERN, 1997. URL: `https://cds.cern.ch/record/368412`.

[14] *The CMS electromagnetic calorimeter project: Technical Design Report*. Technical Design Report CMS. Geneva: CERN, 1997. URL: `https://cds.cern.ch/record/349375`.

[15] *The CMS hadron calorimeter project: Technical Design Report*. Technical Design Report CMS. The following files are from <a href=. Geneva: CERN, 1997. URL: `https://cds.cern.ch/record/357153`.

[16] *The CMS muon project: Technical Design Report*. Technical Design Report CMS. Geneva: CERN, 1997. URL: `https://cds.cern.ch/record/343814`.

[17] David Barney. "CMS Slice". In: (2015). URL: `https://cds.cern.ch/record/2628641`.

[18] F. Abe et al. "Observation of the B_c meson in $p\bar{p}$ collisions at $\sqrt{s} = 1.8$ TeV". In: *Phys. Rev. Lett.* 81 (1998), pp. 2432–2437. DOI: `10.1103/PhysRevLett.81.2432`. arXiv: `hep-ex/9805034 [hep-ex]`.

[19] Georges Aad et al. "Observation of an Excited $B_c^{\pm}$ Meson State with the ATLAS Detector". In: *Phys. Rev. Lett.* 113.21 (2014), p. 212004. DOI: `10.1103/PhysRevLett.113.212004`. arXiv: `1407.1032 [hep-ex]`.

[20] Stephen Godfrey. "Spectroscopy of B_c mesons in the relativized quark model". In: *Phys. Rev. D* 70 (5 2004), p. 054017. DOI: `10.1103/PhysRevD.70.054017`. URL: `https://link.aps.org/doi/10.1103/PhysRevD.70.054017`.

[21] D. Ebert, R. N. Faustov, and V. O. Galkin. "Properties of heavy quarkonia and B_c mesons in the relativistic quark model". In: *Phys. Rev.* D67 (2003), p. 014027. DOI: 10.1103/PhysRevD.67.014027. arXiv: hep-ph/0210381 [hep-ph].

[22] Lewis P. Fulcher. "Phenomenological predictions of the properties of the B_c system". In: *Phys. Rev.* D60 (1999), p. 074006. DOI: 10.1103/PhysRevD.60.074006. arXiv: hep-ph/9806444 [hep-ph].

[23] V. V. Kiselev, A. K. Likhoded, and A. V. Tkabladze. "B(c) spectroscopy". In: *Phys. Rev.* D51 (1995), pp. 3613–3627. DOI: 10.1103/PhysRevD.51.3613. arXiv: hep-ph/9406339 [hep-ph].

[24] Estia J. Eichten and Chris Quigg. "Mesons with beauty and charm: Spectroscopy". In: *Phys. Rev. D* 49 (11 1994), pp. 5845–5856. DOI: 10.1103/PhysRevD.49.5845. URL: https://link.aps.org/doi/10.1103/PhysRevD.49.5845.

[25] Suraj N. Gupta and James M. Johnson. "B(c) spectroscopy in a quantum chromodynamic potential model". In: *Phys. Rev.* D53 (1996), pp. 312–314. DOI: 10.1103/PhysRevD.53.312. arXiv: hep-ph/9511267 [hep-ph].

[26] J. Zeng, J. W. Van Orden, and W. Roberts. "Heavy mesons in a relativistic model". In: *Phys. Rev.* D52 (1995), pp. 5229–5241. DOI: 10.1103/PhysRevD.52.5229. arXiv: hep-ph/9412269 [hep-ph].

[27] C. T. H. Davies et al. "B(c) spectroscopy from lattice QCD". In: *Phys. Lett.* B382 (1996), pp. 131–137. DOI: 10.1016/0370-2693(96)00650-8. arXiv: hep-lat/9602020 [hep-lat].

[28] Roel Aaij et al. "Search for excited B_c^+ states". In: *JHEP* 01 (2018), p. 138. DOI: 10.1007/JHEP01(2018)138. arXiv: 1712.04094 [hep-ex].

[29] Bruno Alves. "Search for the Bc(2S) meson at CMS. CMS - Compact Muon Solenoid". In: (2016). URL: https://cds.cern.ch/record/2215476.

[30] CMS luminosity group. "brilcalc documentation". CMS internal documentation available at http://cms-service-lumi.web.cern.ch/cms-service-lumi/brilwsdoc.html. 2015.

[31] Torbjörn Sjöstrand, Stephen Mrenna, and Peter Skands. "A brief introduction to PYTHIA 8.1". In: *Comp. Phys. Comm.* 178 (2008), p. 852. DOI: 10.1016/j.cpc.2008.01.036. arXiv: 0710.3820 [hep-ph].

[32] Chao-Hsi Chang, Xian-You Wang, and Xing-Gang Wu. "BCVEGPY2.2: A newly upgraded version for hadronic production of the meson Bc and its excited states". In: *Comput. Phys. Commun.* 197 (2015), pp. 335–338. DOI: 10.1016/j.cpc.2015.07.015. arXiv: 1507.05176 [hep-ph].

[33] Johan Alwall et al. "A Standard format for Les Houches event files". In: *Comput. Phys. Commun.* 176 (2007), pp. 300–304. DOI: `10.1016/j.cpc.2006.11.010`. arXiv: `hep-ph/0609017 [hep-ph]`.

[34] D.J. Lange. "The EvtGen particle decay simulation package". In: *Nucl. Instrum. Meth. A* 462 (2001), p. 152.

[35] E. Barberio and Z. Was. "PHOTOS - a universal Monte Carlo for QED radiative corrections: version 2.0". In: *Comput. Phys. Commun. 79* (1994), p. 291.

[36] A. M. Sirunyan et al. "Measurement of quarkonium production cross sections in pp collisions at $\sqrt{s} = 13$ TeV". In: *Phys. Lett.* B780 (2018), pp. 251–272. DOI: `10.1016/j.physletb.2018.02.033`. arXiv: `1710.11002 [hep-ex]`.

[37] Muon POG. "Baseline muon selections for Run-II". Available at `https://twiki.cern.ch/twiki/bin/viewauth/CMS/SWGuideMuonIdRun2`. 2015. URL: `https://twiki.cern.ch/twiki/bin/viewauth/CMS/SWGuideMuonIdRun2`.

[38] Particle Data Group, C. Patrignani, et al. "Review of particle physics". In: *Chin. Phys. C* 40 (2016), p. 100001. DOI: `10.1088/1674-1137/40/10/100001`.

[39] Roel Aaij et al. "Measurement of the ratio of branching fractions $\mathcal{B}(B_c^+ \to J/\psi K^+)/\mathcal{B}(B_c^+ \to J/\psi \pi^+)$". In: *JHEP* 09 (2016), p. 153. DOI: `10.1007/JHEP09(2016)153`. arXiv: `1607.06823 [hep-ex]`.

[40] A. M. Sirunyan et al. "Search for the X(5568) state decaying into $B_s^0 \pi^\pm$ in proton-proton collisions at $\sqrt{s} = 8$ TeV". In: *Phys. Rev. Lett.* 120 (2018), p. 202005. DOI: `10.1103/PhysRevLett.120.202005`. arXiv: `1712.06144 [hep-ex]`.

[41] D.J. Lange. "The EvtGen particle decay simulation package". In: *Nucl. Instrum. Meth.* A462 (2001), pp. 152–155. DOI: `10.1016/S0168-9002(01)00089-4`.

[42] Elisabetta Barberio, Bob van Eijk, and Zbigniew Was. "PHOTOS: A Universal Monte Carlo for QED radiative corrections in decays". In: *Comput. Phys. Commun.* 66 (1991), pp. 115–128. DOI: `10.1016/0010-4655(91)90012-A`.

[43] S. Agostinelli et al. "Geant4 simulation toolkit". In: *Nucl. Instr. Meth. A* 506 (2003), p. 250. ISSN: 0168-9002. DOI: `10.1016/S0168-9002(03)01368-8`. URL: `http://www.sciencedirect.com/science/article/pii/S0168900203013688`.

[44] Stephen Godfrey and Kenneth Moats. "Bottomonium mesons and strategies for their observation". In: *Phys. Rev. D* 92 (5 2015), p. 054034. DOI: `10.1103/PhysRevD.92.054034`. URL: `https://link.aps.org/doi/10.1103/PhysRevD.92.054034`.

[45]   A. M. Sirunyan et al. "Observation of the $\chi_{b1}(3P)$ and $\chi_{b2}(3P)$ and Measurement of their Masses". In: *Phys. Rev. Lett.* 121 (9 2018), p. 092002. DOI: `10.1103/ PhysRevLett.121.092002`. URL: `https://link.aps.org/doi/10.1103/ PhysRevLett.121.092002`.

Observation of Two Excited B_c^+ States and Measurement of the $B_c^+(2S)$ Mass in pp Collisions at $\sqrt{s} = 13$ TeV

A. M. Sirunyan *et al.*[*]

(CMS Collaboration)

Signals consistent with the $B_c^+(2S)$ and $B_c^{*+}(2S)$ states are observed in proton-proton collisions at $\sqrt{s} = 13$ TeV, in an event sample corresponding to an integrated luminosity of 143 fb^{-1}, collected by the CMS experiment during the 2015–2018 LHC running periods. These excited $\bar{b}c$ states are observed in the $B_c^+\pi^+\pi^-$ invariant mass spectrum, with the ground state B_c^+ reconstructed through its decay to $J/\psi\pi^+$. The two states are reconstructed as two well-resolved peaks, separated in mass by $29.1 \pm 1.5\text{(stat)} \pm 0.7\text{(syst)}$ MeV. The observation of two peaks, rather than one, is established with a significance exceeding five standard deviations. The mass of the $B_c^+(2S)$ meson is measured to be $6871.0 \pm 1.2\text{(stat)} \pm 0.8\text{(syst)} \pm 0.8(B_c^+)$ MeV, where the last term corresponds to the uncertainty in the world-average B_c^+ mass.

The B_c family consists of charged mesons composed of a beauty quark and a charm antiquark (or vice versa). The ground state was discovered in 1998 by the CDF Collaboration [1]. The spectrum of this heavy quarkonium family is predicted to be very populated [2–13], but spectroscopic observations and measurements of production properties remain scarce. Indeed, their production yields are significantly smaller than those of the charmonium and bottomonium states, the $\bar{b}c$ production cross sections being proportional to the fourth power of the strong coupling constant, α_S^4 (since two pairs of heavy quarks need to be produced). While the masses and sizes of these beauty-charm quark-antiquark pairs place them between the charmonium and bottomonium systems, so that many properties can be theoretically inferred by interpolation of existing knowledge, the unequal quark masses and velocities could lead to more complex dynamics, where some (nonrelativistic) approximations might break down. Since the $\bar{b}c$ mesons cannot annihilate into gluons, the excited states decay to the ground state via the cascade emission of photons or pion pairs, leading to total widths that are less than a few hundred keV. Figure 1 shows the transitions between the lightest B_c states.

The high collision energies and integrated luminosities provided by the LHC have opened the way for a series of new measurements. The ATLAS Collaboration observed a state with a mass of $6842 \pm 4\text{(stat)} \pm 5\text{(syst)}$ MeV,

consistent with the values predicted for the $B_c^+(2S)$, using data collected at 7 and 8 TeV [14], while the LHCb Collaboration reported that their 8 TeV data sample did not show any significant sign of the $B_c^+(2S)$ or $B_c^{*+}(2S)$ states [15]. The peak observed by ATLAS could be the superposition of the $B_c^+(2S)$ and $B_c^{*+}(2S)$ states, too closely spaced with respect to the resolution of the measurement. The mass difference between the B_c^{*+} and B_c^+ hyperfine partners is predicted to be around 55 MeV, while the corresponding difference between the $B_c^{*+}(2S)$ and $B_c^+(2S)$ masses should be around 35 MeV [11–13].

While the $B_c^+(2S)$ decays directly to $B_c^+\pi^+\pi^-$, the $B_c^{*+}(2S)$ is expected to decay predominantly to $B_c^{*+}\pi^+\pi^-$, followed by the $B_c^{*+} \to B_c^+\gamma$ decay. The emitted photon has a very low energy and its detection is very challenging, so that the $B_c^{*+}(2S)$ peak should be seen in the $B_c^+\pi^+\pi^-$ mass spectrum at the mass $M[B_c^+(2S)] - \Delta M$, where $\Delta M \equiv [M(B_c^{*+}) - M(B_c^+)] - \{M[B_c^{*+}(2S)] - M[B_c^+(2S)]\}$. If the ΔM value is larger than the experimental resolution, the $B_c^+\pi^+\pi^-$ invariant mass distribution will show a two-peak structure. Since $M(B_c^{*+}) - M(B_c^+)$ is predicted to be larger than $M[B_c^{*+}(2S)] - M[B_c^+(2S)]$, the $B_c^{*+}(2S)$ state will be the lower mass peak.

This Letter reports the observation of well-resolved signals consistent with the $B_c^+(2S)$ and $B_c^{*+}(2S)$ states, as well as the first measurement of the $B_c^+(2S)$ mass. Although strictly speaking we should refer to these two signals as $B_c^+(2S)$ and $B_c^{*+}(2S)$ candidates, in the remainder of this Letter, we will skip the word candidates for improved readability. The result is based on the analysis of proton-proton data samples collected by the CMS experiment at a center-of-mass energy of 13 TeV, in 2015, 2016, 2017, and 2018 (the full LHC Run 2), corresponding to integrated luminosities of 2.8, 36.1, 42.1, and 61.6 fb^{-1}, respectively.
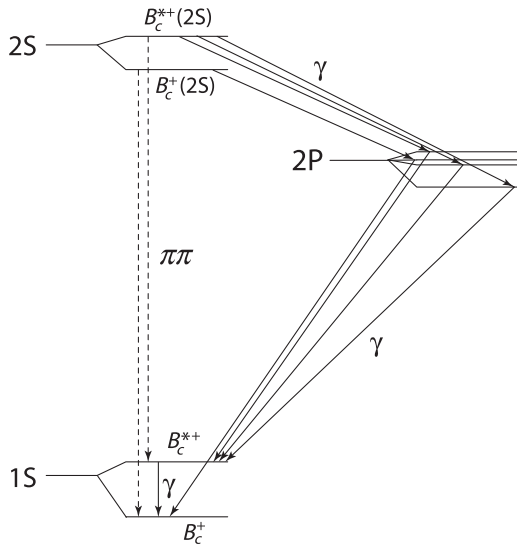
FIG. 1. Transitions between the lightest B_c states, with solid and dashed lines indicating the emission of photons and pion pairs, respectively [2].

The central feature of the CMS apparatus is a superconducting solenoid of 6 m internal diameter, providing a magnetic field of 3.8 T. Within the solenoid volume are a silicon pixel and strip tracker, a lead tungstate crystal electromagnetic calorimeter, and a brass and scintillator hadron calorimeter, each composed of a barrel and two end cap sections. Forward calorimeters extend the pseudorapidity coverage provided by the barrel and end cap detectors. Muons are detected in gas-ionization chambers embedded in the steel flux-return yoke outside the solenoid. A more detailed description of the CMS detector, together with a definition of the coordinate system used and the relevant kinematic variables, can be found in Ref. [16].

The event samples used in this analysis were collected with a two-level trigger system [17]. The first level consists of custom hardware processors and uses information from the muon system to select events with two muons. The high-level trigger requires two oppositely charged muons with pseudorapidity $|\eta| < 2.5$ and transverse momentum $p_T > 4$ GeV, a distance of closest approach between the two muons smaller than 0.5 cm, a dimuon vertex fit χ^2 probability larger than 10%, a dimuon invariant mass in the range 2.9–3.3 GeV, and a distance between the dimuon vertex and the beam axis larger than three times its uncertainty. In addition, the dimuon p_T must be aligned with the transverse displacement vector: $\cos\theta > 0.9$, where $\cos\theta = \vec{L}_{xy}\vec{p}_T/(L_{xy}p_T)$, with $\vec{L}_{xy}$ representing the transverse decay displacement vector of the dimuon. Finally, there must exist a third track in the event compatible with being produced at the dimuon vertex. The offline reconstruction requires two oppositely charged muons matching those that triggered the detector readout, with some requirements being stricter than at the trigger level,

such as $|\eta| < 2.4$ and $\cos\theta > 0.98$. The muons must fulfill the "soft muon identification" requirements [18] and be close to each other in angular space: $\sqrt{(\Delta\eta)^2 + (\Delta\phi)^2} < 1.2$, where $\Delta\eta$ and $\Delta\phi$ are differences in pseudorapidity and azimuthal angle, respectively, between the directions of the two muons.

Several simulated samples were used in the analysis. The B_c^+, $B_c^+(2S)$, and $B_c^{*+}(2S)$ signal samples are generated with the BCVEGPY 2.2 [19] Monte Carlo generator, interfaced with the PYTHIA 8.230 package [20] to simulate the hadronization step, and with EVTGEN 1.6.0 [21] for the decays. Final-state radiation is modeled with PHOTOS 3.61 [22]. The generated events are then processed through a detailed simulation of the CMS detector, based on the GEANT4 package [23], using the same trigger and reconstruction algorithms as used for the collision data. The simulated events include multiple proton-proton interactions in the same or nearby beam crossings, with a distribution matching the measured one. Charge-conjugated states are implied throughout this Letter.

All the physics objects used in this analysis, including the muon tracks, must pass high-purity track quality requirements [24]. The B_c^+ candidates are reconstructed by combining the dimuon with a track, assumed to be a pion. This track must have $|\eta| < 2.4$, $p_T > 3.5$ GeV, at least one hit in the pixel layers, at least five hits in the tracker (pixel and strip layers), and an impact parameter in the transverse plane larger than two times its uncertainty. The B_c^+ candidate is obtained by performing a kinematic fit, imposing a common vertex on the dimuon and pion tracks, and constraining the dimuon invariant mass to be the world-average J/ψ mass [25]. The primary vertex (PV) associated with the candidate B_c^+ is selected among all the reconstructed vertices [26] as the one with the smallest angle between the reconstructed B_c^+ momentum and the vector joining the PV with the B_c^+ decay vertex. Studies based on simulation show that the probability of selecting a wrong vertex is less than 1%. The decay length of the B_c^+, denoted by l, is computed as the (three-dimensional) distance between the PV and the $J/\psi\pi^+$ vertex (assumed to be, respectively, the B_c^+ production and decay vertices). To avoid biases in the determination of l, the PV is refitted without the tracks associated with the muons and the pion.

Similarly to what has been previously done in Refs. [27,28], the B_c^+ candidates are required to have $p_T > 15$ GeV, rapidity $|y| < 2.4$, $l > 100$ μm, and a kinematic fit χ^2 probability larger than 10%. If several B_c^+ candidates are found in the same event, only the one with the highest p_T is kept. The invariant mass distribution of the selected $B_c^+ \to J/\psi\pi^+$ candidates, shown in Fig. 2, is fitted to the expected B_c^+ signal peak, modeled as a sum of two Gaussian functions with a common mean, superimposed on a background composed of three sources of events: (i) the combinatorial background resulting from associating the J/ψ with uncorrelated charged particles, parametrized by a
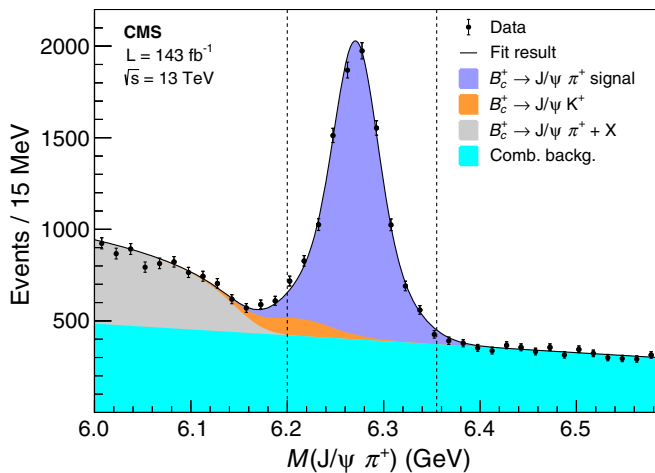
FIG. 2. The invariant mass distribution of the B_c^+ candidates. The vertical dashed lines indicate the mass window retained for the reconstruction of the $B_c^+(2S)$ and $B_c^{*+}(2S)$ candidates. The vertical bars on the points represent the statistical uncertainty in the data. The contributions from various sources are shown by the stacked distributions. The solid line represents the result of the fit.

first-order Chebyshev polynomial function; (ii) partially reconstructed B_c^+ decays, $B_c^+ \to J/\psi \pi^+ X$, only relevant for mass values below 6.2 GeV, described by a (generalized) ARGUS function [29] convolved with a Gaussian resolution function; (iii) a small contribution from $B_c^+ \to J/\psi K^+$ decays, with a shape determined from simulation studies and a normalization fixed relative to the $B_c^+ \to J/\psi \pi^+$ yield, using the ratio of their branching fractions [30] and the ratio of the reconstruction efficiencies. The unbinned maximum-likelihood fit gives a B_c^+ signal yield of 7629 ± 225 events, a B_c^+ mass of $M(B_c^+) = 6271.1 \pm 0.5$ MeV, and a mass resolution of 33.5 ± 2.5 MeV, where the uncertainties are statistical only. The measured mass resolution is consistent with the value expected from the simulation studies. The quality of the fit was evaluated by computing the χ^2 between the binned distribution and the fit function, the result being $\chi^2 = 35$ for 30 degrees of freedom.

The $B_c^+(2S)$ and $B_c^{*+}(2S)$ candidates are reconstructed by performing a kinematic fit, combining a B_c^+ candidate with two opposite-sign tracks and imposing a common vertex. Only B_c^+ candidates with invariant mass in the range 6.2–6.355 GeV are selected. This mass window, indicated in Fig. 2, reflects the measured B_c^+ mass and resolution, with a low-mass edge that, while corresponding to a smaller peak coverage than the high-mass edge, suppresses the contamination from partially reconstructed decays. The lifetimes of the $B_c^+(2S)$ and $B_c^{*+}(2S)$ are assumed to be negligible with respect to the measurement resolution, so that the production and decay vertices essentially overlap. Therefore, the daughter pions are required to be tracks used in the refitted PV (a procedure previously followed in

Refs. [31,32]). One of the pion candidates must have $p_T > 0.8$ GeV and the other $p_T > 0.6$ GeV. The $B_c^+ \pi^+ \pi^-$ candidates must have $|y| < 2.4$ and a vertex χ^2 probability larger than 10%. If several $B_c^+ \pi^+ \pi^-$ candidates are found in the same event, only the one with the highest p_T is kept. Studies with simulated signal samples (providing S) and measured sideband events (providing B) have shown, through the $S/\sqrt{S+B}$ figure of merit, that these are optimal event-selection criteria.

Figure 3 shows the $M(B_c^+ \pi^+ \pi^-) - M(B_c^+) + m_{B_c^+}$ distribution, where $M(B_c^+ \pi^+ \pi^-)$ and $M(B_c^+)$ are, respectively, the reconstructed invariant masses of the $B_c^+ \pi^+ \pi^-$ and B_c^+ candidates, and $m_{B_c^+}$ is the world-average B_c^+ mass [25]. This variable is measured with a better resolution than $M(B_c^+ \pi^+ \pi^-)$ and is, hence, advantageous when searching for peaks in the mass distribution. The measured distribution is fitted to a superposition of two Gaussian functions, representing the $B_c^+(2S)$ and $B_c^{*+}(2S)$ signal peaks, plus a third-order Chebyshev polynomial, modeling the continuum background, with all parameters left free in the fit. The two contributions arising from $B_c^+ \to J/\psi K^+$ decays are also considered; they have shapes identical to the signal peaks, neglecting a shift to lower mass values that should be smaller than 1 MeV, and normalizations constrained by the ratio of the $B_c^+ \to J/\psi K^+$ and $B_c^+ \to J/\psi \pi^+$ signal yields, as previously mentioned. The unbinned extended maximum-likelihood fit gives 67 ± 10 and 51 ± 10 events for the lower-mass and higher-mass peak, respectively. Since these yields are not corrected for detection efficiencies and acceptances, they cannot be used to infer ratios of production cross sections. The two signals are well resolved, their mass difference being $\Delta M = 29.1 \pm 1.5$ MeV, where the uncertainty is statistical only. The widths of the peaks are consistent with the value expected from simulation studies, which is approximately 6 MeV. The χ^2 between the binned distribution and the fit function is 42 for 39 degrees of freedom.

Studies of simulated samples show that the low-energy photon emitted in the $B_c^{*+}(2S)$ decay has a very small reconstruction efficiency, of order 1%. Consequently, the photon is not detected and the mass of the $B_c^{*+}(2S)$ cannot be measured. Given the predicted mass splittings mentioned before [11–13], the $B_c^{*+}(2S)$ peak is expected to be observed at a mass lower than the $B_c^+(2S)$. The mass of the $B_c^+(2S)$ meson, assumed to be the higher-mass peak in Fig. 3, is measured to be 6871.0 ± 1.2 MeV, where the uncertainty is statistical only.

The $M(B_c^+ \pi^+ \pi^-) - M(B_c^+) + m_{B_c^+}$ distribution has also been fitted with the two peaks modeled by a Breit-Wigner function, convolved with a Gaussian resolution function determined from the simulated samples. The result is that, for both peaks, the natural width parameter of the Breit-Wigner function is consistent with zero, indicating that both natural widths are small in comparison with the experimental resolution.
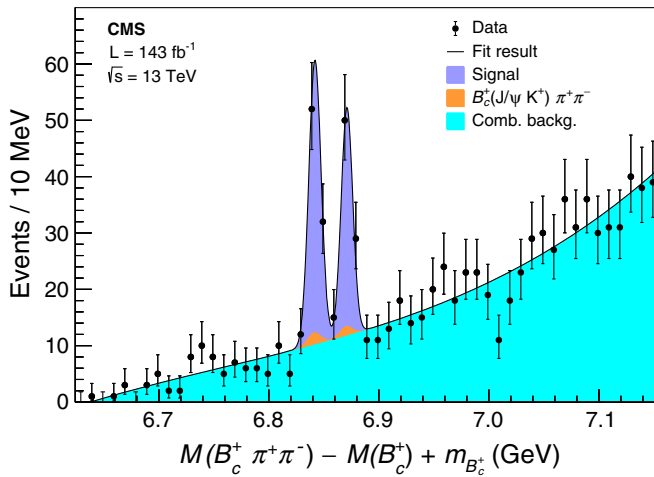
FIG. 3. The $M(B_c^+ \pi^+ \pi^-) - M(B_c^+) + m_{B_c^+}$ distribution. The $B_c^+(2S)$ is assumed to be the right-most peak. The vertical bars on the points represent the statistical uncertainty in the data. The contributions from the various sources are shown by the stacked distributions. The solid line represents the result of the fit.

The fitting procedure was tested using randomly generated event samples, of sizes corresponding to the number of measured events, reflecting the nominal likelihood probability distribution functions and fitted parameters. No significant fit biases were found in the central values and uncertainties.

Several sources of systematic uncertainties have been considered. The mass measurements reported here are expected to be essentially insensitive to the event selection criteria. The analysis was repeated by splitting the data in exclusive subsamples, depending on the B_c^+ rapidity or p_T, or according to the data collection periods. The p_T thresholds were also varied, between 10 and 18 GeV for the B_c^+ and between 3 and 5 GeV for the pion produced in the B_c^+ decay. The results remain unchanged; hence no systematic uncertainty is assigned to the selection criteria. Also, no significant changes are seen in the results when the widths of the Gaussian functions used to describe the two peaks, or their ratio, are fixed to the values evaluated with the simulated event samples. The mass measurements might depend on the models used to describe the signal and background contributions. The impact of the fitting models has been evaluated by varying the considered functional forms. The combinatorial background, nominally represented by a third-order Chebyshev polynomial, has been alternatively modeled by the function $(x - x_0)^\lambda \exp [\nu(x - x_0)]$, where λ, ν, and x_0 are free parameters. For each of the two signal peaks, and corresponding $B_c^+ \to J/\psi K^+$ terms, the default Gaussian function was replaced by a Breit-Wigner parametrization. The differences in the measured observables are taken as the systematic uncertainty associated with the fit modeling. While the alternative background model leads to a negligible change, the systematic uncertainties reflecting the modeling of the

peaks are 0.8 and 0.7 MeV in the $B_c^+(2S)$ mass and in ΔM, respectively.

The nominal fit includes a $B_c^+ \to J/\psi K^+$ component, with the same shape as the signal peaks and normalization defined by the expected ratio of the $B_c^+ \to J/\psi K^+$ and $B_c^+ \to J/\psi \pi^+$ yields in the B_c^+ mass window, corrected by the ratio of the corresponding reconstruction efficiencies. The normalization has been increased by a factor of two, a variation ten times larger than the sum of the uncertainties in the ratio of branching fractions [25] and in the ratio of reconstruction efficiencies, and no significant effect has been seen on the results, so that no systematic uncertainty is associated with this background contribution. The B_c^+ mass distribution includes a contribution from partially reconstructed decays. Their contamination in the $M(B_c^+ \pi^+ \pi^-) - M(B_c^+) + m_{B_c^+}$ distribution is suppressed by the rejection of B_c^+ candidates with invariant mass below 6.2 GeV. To evaluate possible resolution effects associated with this selection, the requirement was changed to 6.1 GeV, a variation that also leads to a larger contamination from $B_c^+ \to J/\psi K^+$ events. The difference between the results, taking into account that the two event samples are strongly correlated, is not statistically significant, so that no systematic uncertainty is assigned. The potential bias introduced in the mass measurement by possible misalignments of the tracker detectors has been evaluated through simulation studies and also by comparing distributions measured in the 2016 and 2017 running periods, a meaningful comparison given that an important fraction of the CMS tracker detector was replaced between these two years. The outcome is that the alignment of the detector leads to a negligible systematic uncertainty in the results of the present analysis. Thus, the total systematic uncertainties are 0.8 and 0.7 MeV in the $B_c^+(2S)$ mass measurement and in ΔM, respectively.

The world-average B_c^+ mass, $m_{B_c^+} = 6274.9 \pm 0.8$ MeV [25], enters in the measurement of the $B_c^+(2S)$ mass, thereby contributing an additional systematic uncertainty of 0.8 MeV. Strictly speaking, however, it is the mass difference $M(B_c^+ \pi^+ \pi^-) - M(B_c^+)$ that is measured event by event, before adding the $m_{B_c^+}$ constant, and it is convenient to report the $B_c^+(2S)$ mass as $M[B_c^+(2S)] - M(B_c^+) = 596.1 \pm 1.2(\text{stat}) \pm 0.8(\text{syst})$ MeV, a value independent of $m_{B_c^+}$. Another interesting mass difference, also unaffected by the uncertainty in the B_c^+ world-average mass, can be derived from the previously reported measurements: $M[B_c^{*+}(2S)] - M(B_c^{*+}) = \{M[B_c^+(2S)] - M(B_c^+)\} - \Delta M = 567.0 \pm 1.0(\text{total})$ MeV. Since the systematic effects previously mentioned cancel almost completely in this mass difference, the total uncertainty is dominated by the statistical term, which was determined by redoing the fit of the $M(B_c^+ \pi^+ \pi^-) - M(B_c^+) + m_{B_c^+}$ distribution setting this new variable as a floating parameter, to properly account for the correlations between the parameters. The observation of two peaks, rather than one, is established

with a significance of 6.5 standard deviations, evaluated with the likelihood-ratio technique confronting the two-peaks (ten free parameters) and one-peak (seven free parameters) hypotheses, using asymptotic formulae [33,34] and accounting for the (dominant) systematic uncertainty in the signal model.

In summary, signals consistent with the $B_c^+(2S)$ and $B_c^{*+}(2S)$ states have been separately observed for the first time by investigating the $B_c^+\pi^+\pi^-$ invariant mass spectrum measured by CMS. The analysis is based on the entire LHC sample of proton-proton collisions at a center-of-mass energy of 13 TeV, corresponding to a total integrated luminosity of 143 fb^{-1}. The two peaks are well resolved, with a measured mass difference of $\Delta M = 29.1 \pm 1.5(\text{stat}) \pm 0.7(\text{syst})$ MeV. The $B_c^+(2S)$ mass is measured to be $6871.0 \pm 1.2(\text{stat}) \pm 0.8(\text{syst}) \pm 0.8(B_c^+)$ MeV, where the last term is the uncertainty in the world-average B_c^+ mass. Because the low-energy photon emitted in the $B_c^{*+} \to B_c^+\gamma$ radiative decay is not reconstructed, the observed $B_c^{*+}(2S)$ peak has a mass lower than the true value, which remains unknown. These measurements contribute significantly to the detailed characterization of heavy meson spectroscopy and provide a rich source of information on the nonperturbative QCD processes that bind heavy quarks into hadrons.

[1] F. Abe *et al.* (CDF Collaboration), Observation of the B_c Meson in $p\bar{p}$ Collisions at $\sqrt{s} = 1.8$ TeV, Phys. Rev. Lett. **81**, 2432 (1998).

[2] E. J. Eichten and C. Quigg, Mesons with beauty and charm: Spectroscopy, Phys. Rev. D **49**, 5845 (1994).

[3] S. S. Gershtein, V. V. Kiselev, A. K. Likhoded, and A. V. Tkabladze, B_c spectroscopy, Phys. Rev. D **51**, 3613 (1995).

[4] J. Zeng, J. W. Van Orden, and W. Roberts, Heavy mesons in a relativistic model, Phys. Rev. D **52**, 5229 (1995).

[5] S. N. Gupta and J. M. Johnson, B_c spectroscopy in a quantum chromodynamic potential model, Phys. Rev. D **53**, 312 (1996).

[6] C. T. H. Davies, K. Hornbostel, G. P. Lepage, A. J. Lidsey, J. Shigemitsu, and J. H. Sloan, B_c spectroscopy from lattice QCD, Phys. Lett. B **382**, 131 (1996).

[7] L. P. Fulcher, Phenomenological predictions of the properties of the B_c system, Phys. Rev. D **60**, 074006 (1999).

[8] D. Ebert, R. N. Faustov, and V. O. Galkin, Properties of heavy quarkonia and B_c mesons in the relativistic quark model, Phys. Rev. D **67**, 014027 (2003).

[9] S. Godfrey, Spectroscopy of B_c mesons in the relativized quark model, Phys. Rev. D **70**, 054017 (2004).

[10] A. Berezhnoy and A. Likhoded, The observation possibility of B_c excitations at LHC, Proc. Sci., QFTHEP2013 (**2013**) 051.

[11] E. B. Gregory, C. T. H. Davies, E. Follana, E. Gamiz, I. D. Kendall, G. P. Lepage, H. Na, J. Shigemitsu, and K. Y. Wong, A Prediction of the B_c^* Mass in Full Lattice QCD, Phys. Rev. Lett. **104**, 022001 (2010).

[12] R. J. Dowdall, C. T. H. Davies, T. C. Hammant, and R. R. Horgan, Precise heavy-light meson masses and hyperfine splittings from lattice QCD including charm quarks in the sea, Phys. Rev. D **86**, 094510 (2012).

[13] N. Mathur, M. Padmanath, and S. Mondal, Precise Predictions of Charmed-Bottom Hadrons from Lattice QCD, Phys. Rev. Lett. **121**, 202002 (2018).

[14] ATLAS Collaboration, Observation of an Excited $B_c^\pm$ Meson State with the ATLAS Detector, Phys. Rev. Lett. **113**, 212004 (2014).

[15] LHCb Collaboration, Search for excited $B_c^\pm$ states, J. High Energy Phys. 01 (2018) 138.

[16] CMS Collaboration, The CMS experiment at the CERN LHC, J. Instrum. **3**, S08004 (2008).

[17] CMS Collaboration, The CMS trigger system, J. Instrum. **12**, P01020 (2017).

[18] CMS Collaboration, Performance of the CMS muon detector and muon reconstruction with proton-proton collisions at $\sqrt{s} = 13$ TeV, J. Instrum. **13**, P06015 (2018).

[19] C.-H. Chang, X.-Y. Wang, and X.-G. Wu, BCVEGPY2.2: A newly upgraded version for hadronic production of the meson B_c and its excited states, Comput. Phys. Commun. **197**, 335 (2015).

[20] T. Sjöstrand, S. Mrenna, and P. Skands, A brief introduction to PYTHIA 8.1, Comput. Phys. Commun. **178**, 852 (2008).

[21] D. J. Lange, The EvtGen particle decay simulation package, Nucl. Instrum. Methods Phys. Res., Sect. A **462**, 152 (2001).

[22] E. Barberio and Z. Wąs, PHOTOS—a universal Monte Carlo for QED radiative corrections: Version 2.0, Comput. Phys. Commun. **79**, 291 (1994).

[23] S. Agostinelli et al. (GEANT4 Collaboration), GEANT4—A simulation toolkit, Nucl. Instrum. Methods Phys. Res., Sect. A **506**, 250 (2003).

[24] CMS Collaboration, Description and performance of track and primary-vertex reconstruction with the CMS tracker, J. Instrum. **9**, P10009 (2014).

[25] M. Tanabashi et al. (Particle Data Group), Review of particle physics, Phys. Rev. D **98**, 030001 (2018).

[26] R. Frühwirth, W. Waltenberger, and P. Vanlaer, Adaptive vertex fitting, J. Phys. G **34**, N343 (2007).

[27] CMS Collaboration, Measurement of the ratio of the production cross sections times branching fractions of $B_c^{\pm} \to J/\psi\pi^{\pm}$ and $B^{\pm} \to J/\psi K^{\pm}$ and $\mathcal{B}(B_c^{\pm} \to J/\psi\pi^{\pm}\pi^{\pm}\pi^{\mp})/\mathcal{B}(B_c^{\pm} \to J/\psi\pi^{\pm})$ in pp collisions at $\sqrt{s} = 7$ TeV, J. High Energy Phys. 01 (2015) 063.

[28] CMS Collaboration, Measurement of b hadron lifetimes in pp collisions at $\sqrt{s} = 8$ TeV, Eur. Phys. J. C **78**, 457 (2018); **78**, 561(E) (2018).

[29] H. Albrecht et al. (ARGUS Collaboration), Search for hadronic $b \to u$ decays, Phys. Lett. B **241**, 278 (1990).

[30] LHCb Collaboration, Measurement of the ratio of branching fractions $\mathcal{B}(B_c^+ \to J/\psi K^+)/\mathcal{B}(B_c^+ \to J/\psi\pi^+)$, J. High Energy Phys. 09 (2016) 153.

[31] CMS Collaboration, Search for the X(5568) State Decaying into $B_s^0\pi^{\pm}$ in Proton-Proton Collisions at $\sqrt{s} = 8$ TeV, Phys. Rev. Lett. **120**, 202005 (2018).

[32] CMS Collaboration, Studies of $B_{s2}^*(5840)^0$ and $B_{s1}(5830)^0$ mesons including the observation of the $B_{s2}^*(5840)^0 \to B^0 K_S^0$ decay in proton-proton collisions at $\sqrt{s} = 8$ TeV, Eur. Phys. J. C **78**, 939 (2018).

[33] S. S. Wilks, The large-sample distribution of the likelihood ratio for testing composite hypotheses, Ann. Math. Stat. **9**, 60 (1938).

[34] G. Cowan, K. Cranmer, E. Gross, and O. Vitells, Asymptotic formulae for likelihood-based tests of new physics, Eur. Phys. J. C **71**, 1554 (2011); **73**, 2501(E) (2013).

A. M. Sirunyan,[1,a] A. Tumasyan,[1] W. Adam,[2] F. Ambrogi,[2] T. Bergauer,[2] J. Brandstetter,[2] M. Dragicevic,[2] J. Erö,[2] A. Escalante Del Valle,[2] M. Flechl,[2] R. Frühwirth,[2,b] M. Jeitler,[2,b] N. Krammer,[2] I. Krätschmer,[2] D. Liko,[2] T. Madlener,[2] I. Mikulec,[2] N. Rad,[2] J. Schieck,[2,b] R. Schöfbeck,[2] M. Spanring,[2] D. Spitzbart,[2] W. Waltenberger,[2] J. Wittmann,[2] C.-E. Wulz,[2,b] M. Zarucki,[2] V. Drugakov,[3] V. Mossolov,[3] J. Suarez Gonzalez,[3] M. R. Darwish,[4] E. A. De Wolf,[4] D. Di Croce,[4] X. Janssen,[4] J. Lauwers,[4] A. Lelek,[4] M. Pieters,[4] H. Van Haevermaet,[4] P. Van Mechelen,[4] N. Van Remortel,[4] F. Blekman,[5] E. S. Bols,[5] S. S. Chhibra,[5] J. D'Hondt,[5] J. De Clercq,[5] G. Flouris,[5] D. Lontkovskyi,[5] S. Lowette,[5] I. Marchesini,[5] S. Moortgat,[5] L. Moreels,[5] Q. Python,[5] K. Skovpen,[5] S. Tavernier,[5] W. Van Doninck,[5] P. Van Mulders,[5] I. Van Parijs,[5] D. Beghin,[6] B. Bilin,[6] H. Brun,[6] B. Clerbaux,[6] G. De Lentdecker,[6] H. Delannoy,[6] B. Dorney,[6] L. Favart,[6] A. Grebenyuk,[6] A. K. Kalsi,[6] J. Luetic,[6] A. Popov,[6] N. Postiau,[6] E. Starling,[6] L. Thomas,[6] C. Vander Velde,[6] P. Vanlaer,[6] D. Vannerom,[6] Q. Wang,[6] T. Cornelis,[7] D. Dobur,[7] A. Fagot,[7] M. Gul,[7] I. Khvastunov,[7,c] C. Roskas,[7] D. Trocino,[7] M. Tytgat,[7] W. Verbeke,[7] B. Vermassen,[7] M. Vit,[7] N. Zaganidis,[7] O. Bondu,[8] G. Bruno,[8] C. Caputo,[8] P. David,[8] C. Delaere,[8] M. Delcourt,[8] A. Giammanco,[8] G. Krintiras,[8] V. Lemaitre,[8] A. Magitteri,[8] K. Piotrzkowski,[8] J. Prisciandaro,[8] A. Saggio,[8] M. Vidal Marono,[8] P. Vischia,[8] J. Zobec,[8] F. L. Alves,[9] G. A. Alves,[9] G. Correia Silva,[9] C. Hensel,[9] A. Moraes,[9] P. Rebello Teles,[9] E. Belchior Batista Das Chagas,[10] W. Carvalho,[10] J. Chinellato,[10,d] E. Coelho,[10] E. M. Da Costa,[10] G. G. Da Silveira,[10,e] D. De Jesus Damiao,[10] S. Fonseca De Souza,[10] L. M. Huertas Guativa,[10] H. Malbouisson,[10] D. Matos Figueiredo,[10] M. Medina Jaime,[10,f] M. Melo De Almeida,[10] C. Mora Herrera,[10] L. Mundim,[10] H. Nogima,[10] L. J. Sanchez Rosas,[10] A. Santoro,[10] A. Sznajder,[10] M. Thiel,[10] E. J. Tonelli Manganote,[10,d] F. Torres Da Silva De Araujo,[10] A. Vilela Pereira,[10] S. Ahuja,[11a] C. A. Bernardes,[11a] L. Calligaris,[11a] D. De Souza Lemos,[11a] T. R. Fernandez Perez Tomei,[11a] E. M. Gregores,[11a,11b] P. G. Mercadante,[11a,11b] S. F. Novaes,[11a] Sandra S. Padula,[11a] A. Aleksandrov,[12] R. Hadjiiska,[12] P. Iaydjiev,[12] A. Marinov,[12] M. Misheva,[12] M. Rodozov,[12] M. Shopova,[12] G. Sultanov,[12] A. Dimitrov,[13] L. Litov,[13] B. Pavlov,[13] P. Petkov,[13] W. Fang,[14,g] X. Gao,[14,g] L. Yuan,[14] M. Ahmad,[15] G. M. Chen,[15] H. S. Chen,[15] M. Chen,[15] C. H. Jiang,[15] D. Leggat,[15] H. Liao,[15] Z. Liu,[15] S. M. Shaheen,[15,h] A. Spiezia,[15] J. Tao,[15] E. Yazgan,[15] H. Zhang,[15] S. Zhang,[15,h] J. Zhao,[15] Y. Ban,[16] G. Chen,[16] J. Li,[16] L. Li,[16] Q. Li,[16] Y. Mao,[16] S. J. Qian,[16] D. Wang,[16] Y. Wang,[17] C. Avila,[18] A. Cabrera,[18] L. F. Chaparro Sierra,[18] C. Florez,[18] C. F. González Hernández,[18] M. A. Segura Delgado,[18] J. Mejia Guisao,[19] J. D. Ruiz Alvarez,[19] D. Giljanović,[20] N. Godinovic,[20] D. Lelas,[20] I. Puljak,[20] T. Sculac,[20] Z. Antunovic,[21] M. Kovac,[21] V. Brigljevic,[22] D. Ferencek,[22] K. Kadija,[22] B. Mesic,[22] M. Roguljic,[22] A. Starodumov,[22,i] T. Susa,[22] M. W. Ather,[23] A. Attikis,[23] E. Erodotou,[23] A. Ioannou,[23] M. Kolosova,[23] S. Konstantinou,[23] G. Mavromanolakis,[23] J. Mousa,[23] C. Nicolaou,[23] F. Ptochos,[23] P. A. Razis,[23] H. Rykaczewski,[23] D. Tsiakkouri,[23] M. Finger,[24,j] M. Finger Jr.,[24,j] E. Ayala,[25] E. Carrera Jarrin,[26] Y. Assran,[27,k,l] S. Elgammal,[27,k] S. Bhowmik,[28] A. Carvalho Antunes De Oliveira,[28]